HOKKAIDO UNIVERSITY

Title	Study on Composite Materials with Macroscopic Double Network Structures
Author(s)	奥村, 剛士; Okumura, Tsuyoshi
Degree Grantor	北海道大学
Degree Name	博士(ソフトマター科学)
Dissertation Number	甲第14845号
Issue Date	2022-03-24
DOI	https://doi.org/10.14943/doctoral.k14845
Doc URL	https://hdl.handle.net/2115/89204
Type	doctoral thesis
File Information	Tsuyoshi_Okumura.pdf

Doctoral Dissertation

Study on Composite Materials with

Macroscopic Double Network Structures

（巨視的なダブルネットワーク構造を有する複合材料に関する研究）

By

Tsuyoshi Okumura

Supervisor: Jian Ping Gong

HOKKAIDO
U N I V E R S I T Y

Laboratory of Soft & Wet Matter, Division of Soft Matter,

Graduate School of Life Science, Hokkaido University

Sapporo 001-0021, Japan

March 2022

Contents

CHAPTER 4 55

Investigating the Defect-Insensitive Nature of Double-Networks using Macro-scale Double-Network Materials

CHAPTER 5 90

Improving the Strengthen and Toughness of Macro-scale Double Networks by Exploiting Poisson's Ratio Mismatch

CHAPTER 6 126

Fabrication of Highly Deformable Hydrogel Composites with Macroscopic Reinforcement

CHAPTER 7 157

Summary of the dissertation

References 161

List of Publications 172

Acknowledgments   174

CHAPTER 1

General Introduction

1.1 Overview

In nature, materials such as bone, nacre, and wood usually possess complex hierarchical composite structures consisting of hard and soft phases.[1–3] These hierarchical structures can range from the nano-scale ($<10^{-7}$ m) to the macro-scale ($>10^{-3}$ m). Moreover, natural composites are known to be lightweight yet have both strength and toughness that can dramatically exceed the sum of the component materials.[4]

Inspired by these hard/soft composites in nature, double-network (DN) hydrogels were developed in our laboratory.[5] DN hydrogels are tough hydrogels with a nano- and micro-scale interpenetrating structure of a hard and brittle 1st network (hard phase) and a soft and ductile 2nd network (soft phase). Even though the polymer content of DN hydrogels is so low that it contains 90 wt% water, its toughness is 10-100x higher than that of the single network hydrogels that make up the DN hydrogel, exhibiting comparable toughness to industrial elastomers. The reason for the high toughness of DN hydrogels is that the brittle polymer chains of the 1st network (sacrificial bonds) preferentially fracture over a wide area before the ductile 2nd network undergoes significant deformation, resulting in the dissipation of a large amount of energy.[6,7] This strategy of toughening by introducing sacrificial bonds (the "DN principle") was revolutionary, and the DN principle has been applied not only to hydrogels but also to industrial materials such as elastomers and is widely applicable to various polymer materials regardless of their chemical constituents.[8–10] In addition, recent research has reported that the DN principle can be applied even when the length-scale of the network structure is extended from the micro-scale to the macro-scale, as long as the condition of

entanglement of two contrasting hard/soft networks is satisfied. Hong and coworkers developed the first "macroscale" double network (Macro-DN) material, consisting of VHB tape adhered to a fabric mesh[11]. The development of Macro-DN materials is beneficial because it allows us to observe the fracture behavior. When this Macro-DN material is stretched, the fabric mesh, acting as the 1st network hard phase fractures, dissipating energy, while the viscoelastic tape, acting as the 2nd network soft phase, prevents premature fracture of the sample. The stress on the sample is transmitted to the fabric through interfacial adhesion with the tape, and fracture of the sample occurs until small islands of fabric are formed, where the interface is not sufficiently strong enough to cause additional fracture. Furthermore, Macro-DN materials have been successfully used to improve toughness due to the DN principle by the incorporation of fabric meshes,[11] metal cores,[12,13] magnetic structures,[14] 3D printed structure,[15] and low melting point alloys.[16]

Recent research has tried to elucidate the DN principle of the nano- and micro-scale DN materials. In the experimental system, researchers attempted to observe the internal structure and phenomena of DN hydrogels by using small-angle neutron scattering (SANS) and small-angle x-ray scattering (SAXS), but it has been difficult to directly understand the DN principle.[17,18] On the other hand, in theoretical systems, simulations have been carried out by using a coarse-grained MD spring-bead model at the microscale and a spring model at the macroscale, and consistent results have been obtained.[19] However, the mechanism by which the DN principle enables the high toughness of DN materials is not completely understood. In this dissertation, we have developed a method to design hard phases based on macroscopic skeleton structures by utilizing 3D printing technology. The simplicity, precision, and reproducibility of these skeletons make them the perfect system to use towards elucidating the toughening mechanism and expression

conditions of the DN principle. Moreover, we have demonstrated explicit control over the strengthening and toughening of Macro-DN materials and fabricated novel highly deformable macroscopic reinforced hydrogel composites by incorporating macroscopic skeleton structures.

1.2 Outline of this dissertation

In **Chapter 2**, we will introduce the general concepts required to understand the basis of this dissertation. We will begin with a summary of the types of hard/soft composites that already exist from nature to industry, and how these materials are related to DN materials. DN materials are divided into two categories: (1) molecular-scale DN materials and (2) macro-scale DN materials. We review the recent progress of each type of DN material, focusing on the characteristic functions of each and the methods to elucidate the DN principle.

In **Chapter 3**, we report a general strategy to develop Macro-DN materials with a macroscopic hard skeleton structure and a discussion on the expression conditions of the DN principle on the macroscale. We use a photocurable 3D printed resin for the hard phase and a commercially available silicone rubber for the soft phase as model materials. 3D printing technology enables the skeleton structure to be easily designed and controlled on the millimeter scale. By controlling the thickness of the pillars that act as sacrificial bonds in the hard skeleton, we show that the primary condition required to express the DN principle is controlled by the strength ratio of the hard and soft phases. We also show that increasing the number of sections in the skeleton increases the number of events where the skeleton fractures as sacrificial bonds, thereby improving the toughness. This work not only provides a promising avenue for the design and development of Macro-DN materials, but also introduces a very effective system for understanding other

unexplored phenomena in DN materials. The system introduced here will be further employed in the following chapters.

We succeeded in reproducing the DN principle through incorporating sacrificial bonds on the macroscale, but the results introduced a new mystery, related to the relative increase in performance compared to the neat components. Nano-scale DN materials can show increases in toughness up to 10-100x, but in the macroscale materials we see an increase of only about 2x. To investigate this mystery, which cannot be explained by the DN principle alone, we consider the inhomogeneity that always exists within both networks of a DN hydrogel. In **Chapter 4**, we investigate how the defects arising from the inhomogeneity of both networks in the DN structure affect the mechanical properties of the DN materials by introducing defects into the hard and soft phases. The results show that DN structures that inherently contain defects in both networks are capable of exhibiting mechanical properties similar to defect-free DN structures. These results shed light on the why DN hydrogels are so strong and tough, especially compared to their neat components: cracks are blunted because defects in the hard phase are supported by locally high concentrations of soft phase, and soft phase defects avoid deformation due to high hard phase density. In the future, this work may become a guideline for versatile composite designs that can ignore material defects to allow composites to exhibit their true mechanical potential.

The aforementioned Macro-DN materials achieved high toughness by preferential, multi-step fracture of the hard skeleton. However, the key to the DN principle is the large amount of energy dissipated due to the widespread fracture of sacrificial bonds, and it is difficult to introduce sacrificial bonds in as large of quantities on the macro-scale as exist on the micro-scale. Furthermore, the strength of Macro-DN materials depends on the

strength of the hard phase, and high strength Macro-DN materials have not yet been achieved. Therefore, in **Chapter 5**, we develop a strengthening and toughening mechanism for Macro-DN materials by designing 1st networks with functional structures that show specific Poisson's ratios, such as an auxetic (negative Poisson's ratio) and honeycomb (positive Poisson's ratio). By introducing hard skeletons with functional structures into the soft phase, the skeleton not only fractures as sacrificial bonds, but also works synergistically with the soft phase due to the difference in Poisson's ratio. This Poisson's ratio mismatch effect between the component materials causes the functional structure of the skeleton to induce large deformation of the soft phase, and the soft phase resists the deformation, resulting in a synergistic improvement in the mechanical properties of the Macro-DN materials. The Poisson's ratio mismatch effect is found to increase with the difference in Poisson's ratio between the component materials, demonstrating that either auxetic or honeycomb structures can be used to improve Macro-DN materials.

While using elastomer systems to develop Macro-DN materials is simple and effective, DN materials based on hydrogel systems are also important because neat hydrogels are extremely brittle. However, developing Macro-DN hydrogel composites is difficult because the soft hydrogel phase can change in volume to match its environment, while the skeleton hard phase maintains a fixed size. In **Chapter 6**, we report a simple and versatile strategy to develop highly deformable hydrogel composites reinforced with an auxetic macroscopic skeleton, which is one of the functional structures described in **Chapter 5**. The auxetic structure exhibits a negative Poisson's ratio and thus extends in the direction perpendicular to the stretching direction. Likewise, when hydrogels swell, they increase in volume. Therefore, auxetic hydrogel composites can eliminate the

volume change mismatch between component materials by flexibly deforming the skeleton in response to the swelling and deswelling of the soft phase caused by water supply or dehydration. When hydrogels deform, they effectively maintain a constant volume. This auxetic hydrogel composite exhibits excellent mechanical properties due to the aforementioned DN principle and the resulting Poisson's ratio mismatch. Beyond the mechanical properties, these composites demonstrate unique functional abilities such as J-shaped mechanical response and skeleton-derived anisotropic swelling and deswelling.

In **Chapter 7**, the results of this thesis are summarized. We end with concluding remarks where we consider future potential avenues of research in the field of Macro-DN materials.

CHAPTER 2

Background

2.1 Hard/soft composites

The hard/soft composites described in this dissertation consist of a soft matrix and hard reinforcing phase. Nature produces many such composites with analogous structures. For example, nacre in mollusk shells is a complex biological composite, where hard mineral plates are stacked in layers, bound together with soft organic macromolecular components such as proteins[4]. Articular cartilage in animals are also a fiber reinforced composite made of collagen fibers (hard phase) in proteoglycan as a soft matrix.[20,21] These composites exhibit excellent properties unattainable by the individual components. Inspired by such composites in nature, many researchers have attempted to develop novel hard/soft composites that mimic them. For example, using the layered structure of the nacre mentioned above as motivation, Amini *et al.* combined and centrifuged glass flakes with poly(methyl methacrylate) (PMMA) to make a composite that shows good strength and toughness.[22] Inspired by porcupinefish epidermis, Yamauchi developed superhydrophobic flexible materials using micrometer-scale tetrapod-shaped ZnO and poly(dimethylsiloxane). This composite has the contradictory mechanical properties of rigid tetrapod-shaped spines and flexible skin.[23] Such biomimetic composites are expected to have a wide range of applications as an alternative to current industrial materials. Therefore, the search for the origins of the special functions of hard/soft composites in nature and the development of new materials that mimic these structures is a very common approach to creating materials that require efficient designs, from aerospace structures to biomaterials.

2.2 Double-network materials

In this dissertation, we focus on "double-networks" (DN), one type of synthetic structure inspired by the hard/soft composites seen in nature. The DN structure was first implemented in tough DN hydrogels, with the goal being to match the mechanical properties of articular cartilage.[24] In significant contrast to traditional hydrogels that are brittle and weak, DN hydrogels possess high toughness and strength due to the DN structure. As the first widely introduced tough hydrogel, it has attracted worldwide attention with derivative research being conducted both in Japan and abroad. The DN structure consists of two interpenetrating networks, where the "1st network" is hard and brittle (hard phase), while the "2nd network" is soft and ductile (soft phase). Despite the fact that DN hydrogels can contain up to 90 wt% water, the fracture energy of DN hydrogels can reach up to 4,000 J/m^2.[25,26] This value is 10-100x higher than that of common single network hydrogels and is comparable to industrial elastomers. Recent research suggests that the unusually high toughness of DN hydrogel may be due to "sacrificial bonds".[6] When force is applied to the DN hydrogel, the hard phase fractures prior to global fracture of the composite structure. The hard phase structure therefore contributes sacrificial bonds, which break efficiently to dissipate energy and avoid stress concentrations. Sacrificial bonds break over a wide area before any cracks are capable of growing. This fracture process results in the dramatic increase in toughness seen in DN hydrogels. This toughening mechanism, commonly referred to as the "DN principle", is similar to the mechanism proposed for high toughness of bone, and it has recently been elucidated that the DN principle is a common principle in tough materials, including biomaterials.[27] Many researchers have developed new types of tough materials by incorporating sacrificial bonds and implementing the DN principle. From here, we review the recent progress of DN materials, which are divided into two categories: (1) molecular-scale DN materials, and (2) macro-scale DN materials. We will pay special attention to

the characteristic functions of the DN materials and methods to elucidate the DN principle at each scale.

2.2.1 *"Molecular-scale" double-network materials*

The "molecular-scale" DN materials described here possess a hard reinforcing phase that exists on the size-scale from several nanometers up to several tens of micrometers. We introduce some typical examples of recently developed molecular-scale DN materials.

• Materials expressing the DN principle at molecular-scale

The first DN hydrogels developed have a contrasting dual interpenetrating network structure: a soft neutral lightly crosslinked covalent network within an extended, low density, highly crosslinked covalent polyelectrolyte network.[24] The electrolyte network, becomes rigid due to electrostatic repulsion and osmotic pressure caused by ionic dissociation and contributes the sacrificial bonds. Covalent bonds cannot easily be reformed once they break. As a result, this network acts as irreversible sacrificial bonds, and the mechanical properties cannot recover, resulting in permanent hysteresis. Subsequent research has demonstrated that by swelling a soft neutral network so that it becomes as rigid as the electrolyte network, it is also able to contribute sacrificial bonds.[28] Demonstrating that the DN principle can be reproduced using this neutral network as sacrificial bonds was revolutionary because it suggested that tough DN hydrogels can be synthesized from any combination of hydrophilic polymers. This means it is possible to use the DN principle with various functional polymers. Some researchers succeeded in introducing physical bonds into the hydrogel as reversible sacrificial bonds.[29–31] For example, In an alginate-polyacrylamide hydrogel, where the alginate hydrogel is cross-linked by ionic bonds as the 1st network within a polyacrylamide 2nd network, the toughness is greatly improved due to the reversible fracture of ionic bonds in alginate

hydrogel. Moreover, polyampholyte (PA) hydrogels consist of a single network made by copolymerizing high concentrations of ionic monomers with an equal balance of positive and negative charges. PA hydrogels also have improved toughness. In addition, unlike in DN hydrogels where covalent bonds act as the sacrificial bonds, alginate-polyacrylamide hydrogels and PA hydrogels show high durability and self-healing ability in cycle tests because the fractured sacrificial bonds can be reformed with time. It has also been reported that inorganic materials can act as sacrificial bonds instead of polymer networks. Fukao *et al.* successfully reproduced the DN principle by mineralizing hydroxyapatite (HAp) particles in hydrogels.[32] The contribution of dissipated energy due to HAp fracture is over 5x higher than that from the polymer during tensile deformation. They showed that the amorphous parts of the HAp minerals fracture during deformation. This suggests that sacrificial bonds are not limited to polymer networks, but also various materials can be introduced as sacrificial bonds. Furthermore, the DN principle can be applied not only to hydrogels, where water is the solvent, but also to inorganic/organic DN hydrogels with ionic liquids as solvent and solvent-free DN elastomers.[9,10,33–35] The summation of this work shows that the DN principle is a universal principle for toughening soft materials, regardless of chemistry.

• **Elucidation of the DN principle and DN structure at molecular-scale**

It is known that the balance of the entanglements between the hard and soft phase is important in DN hydrogels, and that the DN principle is not expressed by simply forming an interpenetrating structure of any two polymer networks. To better understand how the structure influences the fracture behavior of DN hydrogels, researchers have investigated the fabrication conditions and materials of both phases. Saika *et al.* found that by changing the fabrication conditions of both networks, tough DN hydrogels or fragile DN

hydrogels can be made.[36] By adjusting the crosslinking concentration of the 1st network and the monomer concentration of the 2nd network, the fracture stress of each individual network can be controlled. These experimental results show that the monomer concentration of the 2nd network must be higher than a certain concentration in order to express the DN principle, and that the monomer concentration of the 2nd network must be increased when the crosslinking concentration of the 1st network is increased. It was found that the key factor to change the fracture behavior DN hydrogels from fragile to tough is the relative fracture stress ratio of each independent network. In addition, hydrogel networks are usually very inhomogeneous on the micro-scale and it is therefore difficult to control and understand the mechanical properties due to DN principle. Matsuda *et al.* proved that the swelling ratio of the 1st network affects the mechanical properties of DN hydrogels by using a Tetra-PEG 1st network, which has a homogeneous network structure, in a DN hydrogel.[37] In this work they learned that the yield phenomena of DN hydrogels depends on the tension of the 1st network.

The fracture behavior of the molecular-scale DN structure in DN hydrogels is difficult to observe. Fukao *et al.* succeeded in observing the average fracture behavior of the 1st network in DN hydrogels by using in situ small-angle X-ray scattering.[18] The fracture behavior of the brittle 1st network strongly depends on the relative strength of the two networks. In particular, the relative strength of the two networks changes the degree of stress concentration in the submicrometer-scale voids (defects) that are preexisting in the 1st network, and the larger the difference in relative strength, the larger the degree of stress concentration in the voids, resulting in the yielding phenomenon characteristic of DN hydrogels. Moreover, simulations also have been performed to understand the fracture behavior of the DN structure. Higuchi *et al.* used coarse-grained molecular

dynamics with a spring-bead model for polymer chains to clarify the effect of DN structure on the mechanical properties and fracture behavior of DN hydrogels at the molecular-scale.[19] In the low-strain region, the stress rises due to the strained 1st network and the fracture of the 1st network was observed. Due to the relative high density of the 2nd network, the 1st and 2nd networks are sufficiently entangled, and the DN hydrogel shows high toughness due to the flexible 2nd network in the high-strain region without fracture. The cumulative results of this research have gradually led us to understand the previously unexplained phenomena of the DN effect and provided guidelines for controlling the mechanical properties originating from DN structures on the molecular-scale.

2.2.2 *"Macro-scale" double-network materials*

The "macro-scale" composites described here have hard reinforcing phases that range from about several hundred micrometers to several tens of millimeters. We introduce some typical examples of recent developments in macro-scale DN materials.

• **Materials expressing the DN principle at the macro-scale**

Inspired by the DN principle, Feng *et al.* developed the first composite with a "macro-scale" DN structure, consisting of a mesh-like fabric (hard phase) and VHB tape (soft phase).[11] The useful aspect of this Macro-DN materials development is that the fracture behavior of the hard phase can be directly observed. When a force is applied to this composite, the fabric fractures as sacrificial bonds and dissipates energy, but the VHB tape prevents the sample from fracturing, thus achieving high toughness. Cooper *et al.* developed a Macro-DN material with gallium metal (hard phase) inserted as the core into an elastic shell of poly(styrene-ethylene butylene-styrene) (SEBS) (soft phase).[13] During deformation, the metal fractures in multiple steps, maintaining stress at the fracture

strength of the metal. Even when the metal fractures, the soft elastomer absorbs the strain and allows for longer deformation without breaking the composite. The repeated fracture of the high modulus metal of this Macro-DN material increases the energy dissipation during deformation, resulting in an increase in the toughness of the Macro-DN material. This gallium metal core that acts as the hard phase not only contributes sacrificial bonds, but also imparts conductivity to the Macro-DN material. Furthermore, even if the metal core fractures, it can be repaired repeatedly as long as the soft phase does not fracture.

On the other hand, there are cases where something other than the hard phase acts as sacrificial bonds. King *et al.* develop fiber reinforced soft composites (FRSCs) by combining tough polyampholyte hydrogels with woven glass fiber fabric.[38] Huang *et al.* discovered that the toughness of the FRSC increases in conjunction with the toughness of the hydrogel.[39] This suggests that this toughening mechanism is due to the fracture of the large amount of ionic bonds as sacrificial bonds not only between the fibers and hydrogel but also within the hydrogel itself. Furthermore, by using elastomers instead of hydrogels, extremely tough FRSCs can also be developed.[40,41] From the discussed results, the DN principle has shown to be applicable universally, regardless of the size scale of the networks. In addition, since there is no restriction on the types of materials that can be used as the hard phase, further new functions can be added to Macro-DN materials through the hard phase.

• **Elucidation of the DN principle and DN structure at macro-scale**

Some research on the elucidation of DN principle have also been conducted in Macro-DN materials. Since the structure of the hard phase is macroscopic, the fracture behavior can be directly observed, which has the potential to clearly explain the effect of the DN structure on the mechanical properties. Takahashi *et al.* has also developed hydrogel/low-

melting-point alloy (LMA) composites that exhibit the DN principle on the macro-scale.[42] In this study, when the fracture strength of the hard LMA skeleton is less than that of the hydrogel matrix, multistep internal fracture within the LMA was observed, suggesting that LMA acts as the 1st network based on the DN principle. Inspired by the DN principle, Tauber *et al.* employed computer simulations to investigate how disorder controls the brittle-to-ductile transition from the micro-scale to the macro-scale.[43] A random spring network model featuring two different spring types, representative of the two networks in the DN structure, enables them to study the combined effect of initial disorder and network-induced stress heterogeneity. They revealed that a force balance between components gives a good description of the brittle-to-ductile transition. These results provide guidelines for the design and optimization of Macro-DN materials.

To clarify the relationship between the DN principle and DN structure for the development of new materials required for our future society is very important. Although research on Macro-DN materials is still in its infancy, the development of Macro-DN materials can be expected to have a domino effect on the development of various DN materials. Therefore, in this dissertation, we develop a method to design a simple macro-scale skeleton that can be used as the hard phase, and directly observe the fracture behavior of Macro-DN materials to elucidate unexplained phenomena in DN materials. We also focus on modifying the design of the skeletal structure of the hard phase and investigate universal strategies and practical methods to fabricate various Macro-DN materials for various applications.

In this dissertation, the components of the DN materials, regardless of source or size scale, are referred to as the hard phase and soft phase. The components of the DN materials on the molecular-scale are labeled 1st network and 2nd network, respectively.

The components of the DN materials on the macro-scale are labeled as the skeleton and matrix, respectively.

CHAPTER 3

Elucidation of the Conditions Governing the Double-Network Principle in Macroscale Double-Network Materials

3.1 Introduction

For applications ranging from biomaterials[44,45] to soft electronics and robotics,[46–49] soft materials with improved mechanical properties are required to bring these applications to reality. In particular, most hydrogels have inferior mechanical properties compared to conventional soft materials such as rubber, so various unique molecular toughening mechanisms have been developed.[50] These mechanisms include slide-rings with mobile crosslinks,[51,52] healable dynamic bonds,[29,30,53] and double networks.[6,24,54] As covered in **Chapter 2**, double-network (DN) structures achieve high toughness by incorporating an interpenetrating network design with strong contrasting structure and properties, where the "1st network" consists of relatively short and stiff polymer strands, and the "2nd network" consists of relatively long and stretchable polymer strands (**Figure 1a**). Enhanced toughness is due to two effects: 1) when the sample is deformed, the covalent bonds of the "1st network" fracture, dissipating energy, while the 2nd network maintains global integrity, and 2) at the crack tip, the fracture of the 1st network softens the material to avoid stress concentrations, resulting in increased resistance to crack growth.[6] The DN principle has been extremely important towards modern hydrogel design as it enables hydrogels that are tough but also have enhanced stiffness, similar to that of cartilage.

Recently this DN principle has become a universal principle for toughening soft

materials, regardless of material chemistry.[9,10,35] Moreover, It has been found that this DN principle can be expressed even when the length-scale of DN structure is extended from the molecular-scale to the macro-scale. For the 1st network of Macro-DN materials with DN structure at macro-scale, fabric meshes,[11] metal cores,[12,13] magnetic structures,[14] 3D printed structure,[15] and low melting point alloys[16] are used, which undergo multiple fracture events, increasing dissipation. While some previous studies have recognized the importance of sacrificial fracture in individual systems, the generalized design criteria for utilizing this mechanism and its relationship to the DN concept has not been elucidated.

To carefully study the important parameters that control the mechanical response of Macro-DN materials, we utilize a combination of a 3D printed rigid plastic grid as a sacrificial "1st network" skeleton (hard phase), embedded within a stretchable elastomer "2nd network" matrix consisting of a silicone rubber (soft phase) (**Figure 1b**). 3D printing allows for the easy design of hard phase structures with precision in all three dimensions. Elastomers possess properties that make them suitable as soft phase, including simple preparation, high stretchability, and relatively high toughness. This model system provides a basis to systematically probe the parameter space of Macro-DN materials. Depending on the mechanical properties of the individual components, the composite system can exhibit multi-step internal fracture without global failure, resulting in high composite stiffness (from the reinforcing skeleton) and high stretchability (from the matrix). The hysteresis energy of these composites greatly exceeds that of the neat matrix. By tuning the strength of the reinforcing skeleton, we can control the yield force, defined for this system as the force at which sequential internal fracture occurs, creating a type of "mechanical fuse." We find that at a skeleton to matrix strength ratio of 1 the sample undergoes a transition from multi-step ductile to single-step brittle fracture, with optimal

yield strength and toughness being achieved near the transition point. We also studied the force transmission mechanism and discovered that a grid-based skeleton that results in topological interlocking is essential, as it enables force transmission at length-scales much less than can be achieved solely through interfacial adhesion. Without needing strong interfacial adhesion and using the mechanical guidelines introduced here, we were able to create tough composites with a wide range of material types, including renewable materials. Importantly, the Macro-DN method provides a pathway to incorporate important functional materials such as metals and ceramics into soft and ductile, yet tough composite structures. This work presents general design criteria for macroscale double network composites and should play an important role in expanding the mechanical properties of soft materials.

3.2 Experiments

3.2.1 Materials

The plastic materials required to fabricate the rigid skeleton was AR-M2 (model material) purchased from Keyence Co. AR-M2 consists of acrylate monomer, urethane-acrylate oligomer and photoinitiator. During fabrication of the skeleton, AR-S1 (Keyence Co) was used as a support material. AR-S1 consists of acrylate monomer, polypropylene glycol and photoinitiator. Additional skeletons were made with wood (TOKYU HANDS), and Styrofoam (TOKYU HANDS) in **Section 3.3.4**. The silicone rubber solution used for synthesizing the soft and stretchable silicone rubber as the matrix is a commercially available two-part kit, KE-1603-A, and KE-1603-B, (Shin-Etsu Chemical) and was used as received without further purification and according to instructions. Additionally, natural rubber (Qua Yu Kasei) was used as a matrix in **Section 3.3.4**.

3.2.2 Skeleton fabrication

The grid-shaped plastic skeletons were designed by CAD software (Inventor, Autodesk Inc. and Shade 3D, Shade 3D Co., Ltd.) and 3D printed (AGILISTA-3000, Keyence). 3D printing allows for easy design via computer-aided drawing software and provides fine control over geometry as well as good reproducibility. The results reported from **Figure 3** to **Figure 10** and **Figure 12** represent composites comprised of skeletons fabricated through 3D printing. **Figure 1** contains a schematic illustration of the skeleton designed for use in **Section 3.3.1**. Full control over geometry is available, however some parameters were not changed throughout this chapter:

(1) Each end of the skeleton consists of a large rigid frame as a handle. This region provides sufficient stiffness for the grips of the tensile tester, and ensures that the gauge length region undergoes deformation, not the regions gripped by the tensile tester.

(2) The geometry of the skeleton without handles was maintained for all samples with of 10 mm, length of 34 mm, and thickness of 0.5 mm. An open lattice structure was chosen to enable topological interlocking and improve force transmission between the skeleton and matrix.

(3) The thick cross bars were used to delineate individual sections and maintain fracture in one dimension, and had a width of 10 mm, a length of 2 mm, and a thickness of 0.5 mm. Robust cross bars were employed to resist contraction forces during stretching, resulting in controlled stretching in the length direction.

(4) The number of sacrificial bonds per section was kept constant at 3 bonds per section, unless otherwise noted. It is possible to modify the number of bonds per section, and preliminary tests were carried out with a varying number of sacrificial bonds per section. Ultimately, it was determined that the cross-sectional area of sacrificial bonds was the

primary contribution to dissipation, so a fixed number of sites was chosen for systematic analysis. In this **Chapter 3**, the specific geometric parameters which were varied include the number of sections (from 1-13) and the cross-sectional area of the sacrificial bonds (designed thickness of 0.3 mm and width ranging from 0.4 mm to 1.2 mm, with three per section). There was some variation between inputted sample size and true printed dimensions. Table 1 contains the input dimensions and resulting true dimensions. All dimensions listed in the text represent the true cross-sectional area of the skeleton. From **Figure 5** to **Figure 9** utilize samples with varying cross-sectional area. **Figure 3**, **Figure 4**, **Figure 10**, and **Figure 12** utilize samples with a cross-sectional area of 0.58 mm^2.

(5) A spacer was designed around the exterior of the skeleton to fix the skeleton in the middle of the matrix and maintain a total composite thickness of 1.5 mm and was removed prior to sample testing.

After printing, the skeletons were washed in deionized water to remove the support material and dried prior to composite fabrication.
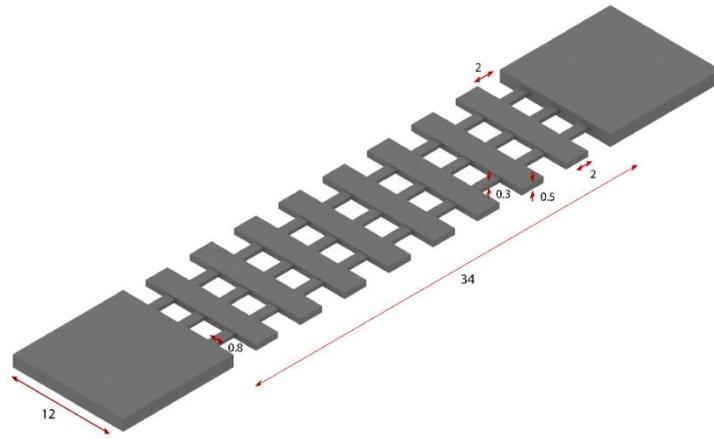
Figure 1. Dimensions of the skeleton used in Section 3.3.1. All dimensions are listed in mm.

Table 1. Input dimensions versus printed dimensions of sacrificial skeleton structures

Input Width (mm)	Input Thickness (mm)	True Width (mm)	True Thickness (mm)	Number of Bonds	True Cross-sectional Area (mm²)
0.4	0.3	0.45 ± 0.02	0.19 ± 0.01	3	0.26
0.6	0.3	0.58 ± 0.03	0.23 ± 0.01	3	0.40
0.8	0.3	0.72 ± 0.04	0.27 ± 0.01	3	0.58
1	0.3	0.99 ± 0.03	0.28 ± 0.01	3	0.83
1.2	0.3	1.20 ± 0.03	0.29 ± 0.01	3	1.04

3.2.3 Synthesis of Macro-DN composites and pristine matrices

To prepare the reaction vessel, plastic skeletons were placed on a glass plate and surrounded by a 1.5 mm thick silicone spacer. For the silicone system, the silicone rubber precursor solution was prepared by mixing the two silicone components at a mixing ratio of 1:1 in a vacuum mixer (ARV-310, Thinky Co.). Immediately, the precursor solution

was poured into the mold and the mold was placed on a level table for 48 hours to cure the silicone. After that, the sample was cut into specific dimensions ($l_0 \times w_0 \times t_0 = 34 \times 12 \times 1.5$ mm^3) using a laser cutter (PLS4.75, Universal Laser Systems). A schematic of the sample used in **Section 3.3.1** with dimensions can be seen in **Figure 2a**. Two cross-sectional images are shown corresponding with the colored planes in **Figure 2a**. **Figure 2b** is a cross-sectional image of the plane highlighted in red, containing sacrificial bonds. **Figure 2c** is a cross-sectional image of the plane highlighted green, containing the cross bar. The sample is embedded on all sides by silicone rubber. The dimensions listed represent the programmed values sent to the 3D printer. This results in a sample with 0.5 mm of rubber between the surface and the top of the cross bars, and 1 mm of rubber separating the side from the edge of the cross bars (**Figure 2b** and **Figure 2c**). For the neat silicone rubber (matrix), the samples were prepared at the same formulation and polymerization conditions as those of the composites for the mechanical tests in the absence of the plastic skeletons.
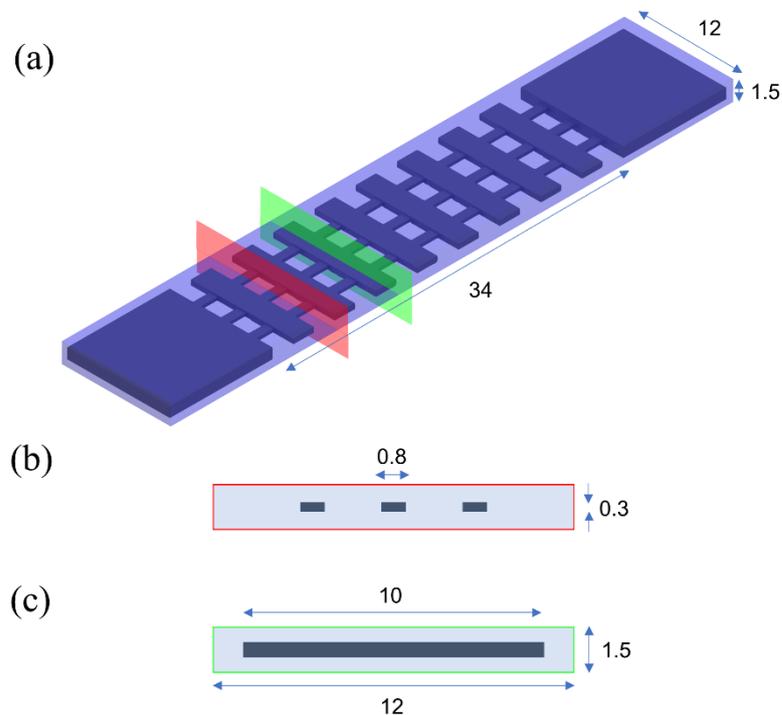
Figure 2. Schematics of the fabricated composite. (a) Schematic of the skeleton embedded in elastomer. (b) Cross-section of the red plane, containing the sacrificial bonds. (c) Cross-section of the green plane, containing the cross bar. The dark blue phase represents the skeleton while the grey phase represents the matrix.

3.2.4 Synthesis of additional composites

In **Section 3.3.4** which includes **Figure 13**, grids made from wood and polystyrene are introduced. In these systems, a bulk sheet of material is the raw material, and a laser cutter is used to prepare the reinforcing skeleton. This method provides slightly less control than 3D printing, because there is no independent control of thickness. Therefore, in these samples, the sacrificial bonds and the cross bars have the same thickness. This may influence the uniformity of the fracture process, as there is less stress at the interface between sacrificial bond and cross bar. However, **Figure 13** shows that laser cutting samples from sheets of raw materials is an applicable method to create macroscale double network composites. Combination with silicone rubber occurred following the same

procedure as listed above. Samples prepared from natural rubber latex were fabricated using an open cell design with just one glass plate, to allow for evaporation of the latex solution. The composite was dried at room temperature for 3 days.

3.2.5 Tensile tests

Uniaxial tensile tests were performed on the composites, pristine silicone rubber (matrix), and the neat plastic skeletons using a tensile-compressive tester (Instron 5965 type universal testing system). All samples were stretched along the length direction of the samples at an extension rate of 50 mm/min. Stretch ratio, l, is defined as l/l_0, where l_0 and l are the length of the sample before and during elongation, respectively. All stretching experiments were recorded visually with a video camera (Panasonic VX985M). Fracture of the skeleton could be seen visually and appears in the data as a local maximum in force. Work to fracture was calculated as the area under the force versus stretch ratio curve,

$$W = l_0 \int_{\lambda=1}^{\lambda=fracture} F d\lambda.$$

3.2.6 Cycle tests

The cyclic loading/unloading tensile test for evaluating the energy dissipation ability of the composites was performed by stretching one sample repeatedly with increasing stretch. The composites and pristine silicone rubber were deformed to strains of $\lambda_x = 0.2$ – 1.6 (with increasing intervals of 0.2) at a velocity of 50 mm/min at room temperature. Then, samples were returned to the initial displacement immediately at the same velocity. The energy dissipation was calculated from the hysteresis area, W_{hys} by:

$$W_{hys} = l_0 \int_{\lambda=0}^{\lambda=\lambda_x} (F_{load} - F_{unload}) d\lambda$$

Where F_{load} and F_{unload} are the stress during loading and unloading, respectively.

3.2.7 Interfacial adhesion tests

The pull-out tests were carried out using a tensile tester in order to measure the adhesive strength of the interface between the skeleton and the matrix. Plastic posts (rod-shape skeletons) were 3D printed and embedded to depths of 5, 7, 10 and 16 mm respectively in silicone rubber. The cross-sectional area of the plastic posts was kept constant (0.5 mm×0.8 mm = 0.4 mm^2) for all the samples. The silicone rubber was fixed to the bottom of a tensile testing machine and the plastic post was fixed to the crosshead, and a pull-out test was conducted at a speed of 50 mm/min. The adhesion strength between the two phases was determined by dividing the maximum value of the force generated between the silicone rubber and the plastic post by the surface area of the plastic post embedded in the silicone rubber. For the fabricated composites, the adhesion strength was calculated by multiplying the adhesive stress with the perimeter of the sacrificial bond, the section interval length, and the number of sacrificial bonds per interval.

3.3 Results & discussion

3.3.1 Macro-scale double-network materials

Rigid 3D printed grid-shaped skeletons are incorporated into a stretchable matrix as a sacrificial phase. These skeletons are designed to fracture, increasing energy dissipation in a manner analogous to the 1st network of DN hydrogels. The use of 3D printing facilitates this process by allowing easy control of skeleton fracture strength, and has been shown to work well to incorporate soft materials.[55–57] The general design can be seen in **Figure 3c**, where the rigid skeleton is shown in dark blue, and the stretchable matrix is shown in light pink. Based on previous research that utilizes soft composite structures,[16,58] we can generally outline the role of each phase. The matrix controls the maximum fracture force, F_x, and stretch at break of the composite, λ_x, while the rigid skeleton controls the

stiffness, k, of the composite. The vertical links within the rigid skeleton are designed to act as macroscale "sacrificial bonds." The force at which these bonds break, and their energy dissipation contribution, can be tuned by modifying the length, L_s, the cross-sectional area, A_{cs}, and the number n_s, of the sacrificial bonds, or by changing the volume fraction, φ, of the matrix related to the rigid phase of the composite. Furthermore, the number of total sections, S, can be tuned, influencing the total potential cyclability, energy dissipation, and ductile response of the composite.

For the exemplary system, the reinforcing skeleton consists of a hard polyurethane-polyacrylate copolymer resin, with a modulus over 1 GPa, and the elastomer matrix is a commercial elastic silicone rubber with a modulus of approximately 0.7 MPa (**Table 2**). The nominal dimensions are fixed, with a length of 34 mm, width of 12 mm, and thickness of 1.5 mm. The reinforcing skeleton contains $S = 9$ sections, each supported by three sacrificial bonds, $n_s = 3$. The thickness and width of the sacrificial bonds were 0.27 mm and 0.72 mm, respectively, resulting in total a cross-sectional area per section of $A_{cs} = 0.58$ mm^2 (complete detailed dimensions are shown in **Figure 1**). This sample has a volume fraction of matrix, φ, of 0.85. The force, F, versus stretch ratio, λ, for the skeleton, matrix, and Macro-DN composite can be seen in **Figure 3d** and **Table 3**. The two neat components have drastically contrasting mechanical properties in their independent form. The stiffness, k, of the skeleton (28.8 N/mm) is much greater than that of the matrix (0.51 N/mm), while the fracture stretch, λ_x, of the matrix (2.71) exceeds that of the skeleton (1.03). When combined, the mechanical properties of the composite are visibly different. At small stretch, the composite is stiff and quickly fractures (**Figure 3d(i)**), eclipsing the curve of the neat skeleton. However, in contrast to the brittle failure of the independent skeleton, the force is transferred into the matrix, in the location of the initial fracture event (**Figure 3d(ii),** denoted by yellow dashed line). The decreased force and increased

stretchability after fracture of the skeleton is similar in many ways to the release of "hidden length" in the protein titin.[57] As stretching continues, the force increases until the force in the matrix exceeds the fracture strength of the skeleton, and the skeleton fractures elsewhere, creating a second local deformation region (**Figure 3d(iii)**). This process repeats (**Figure 3d(iv)**), and subsequent fracture events (**Figure 3d(v)** and **Figure 3d(vi)**) maintain the high force within the sample. Eventually, once all sacrificial bonds that make up the skeleton are fractured, rupture will occur through the matrix phase (**Figure 3d(vii)**).

Table 2. Mechanical properties of the component materials measured by uniaxial tensile testing. These values were measured using dumbbells (gauge region: $l_0 \times w_0 \times t_0 = 12 \times 2 \times 0.5$ mm^3) based on Japanese Industrial Standard. Data are the average of n = 3 measurements.

Component	Young's modulus E (MPa)	Fracture Stress σ (MPa)	Fracture Strain ε	Work of Fracture W (MJ m^{-3})
Skeleton	1017 ± 11.6	53.25 ± 1.88	0.078 ± 0.003	2.75 ± 0.26
Matrix	0.66 ± 0.02	4.27 ± 0.37	7.052 ± 0.541	15.99 ± 2.82
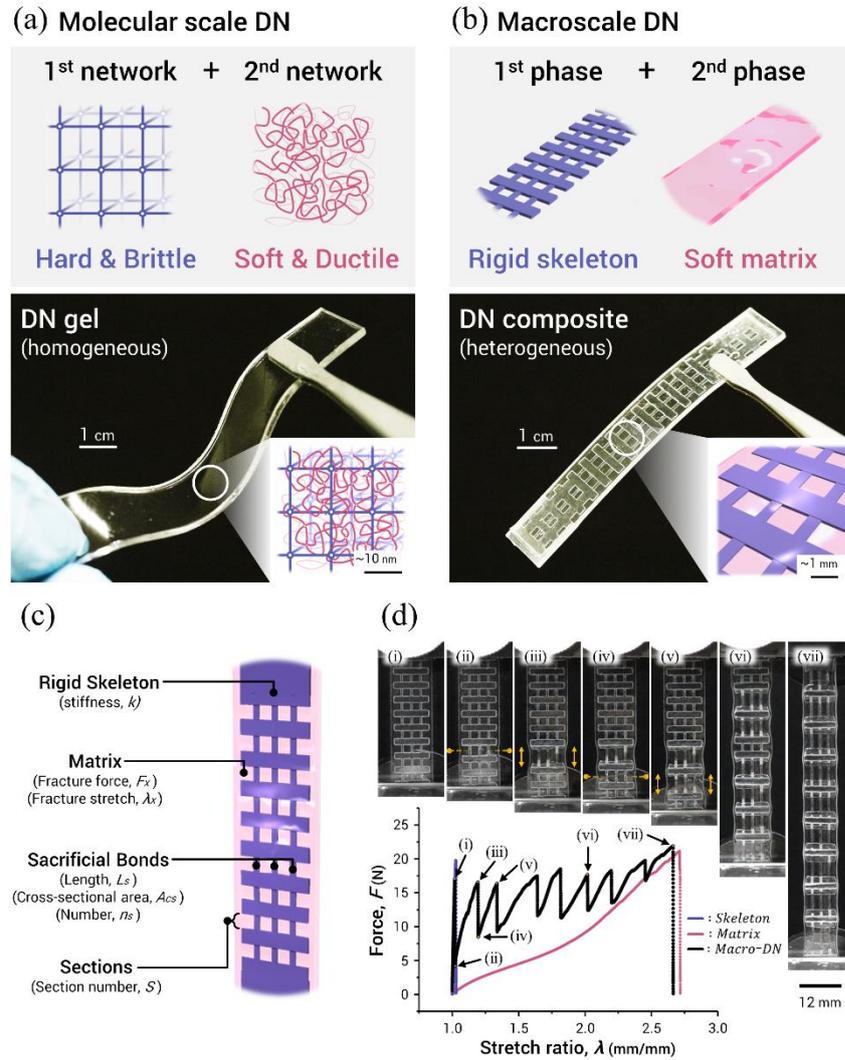
Figure 3. Extending the double network concept from the molecular-scale to the macro-scale. (a) Required network properties for creating double-network materials: hard/brittle properties are required for the 1st network (sacrificial network) and soft/ductile properties are necessary for the 2nd network. (b) Implementation of the double-network concept on the macroscale. The Macro-DN composite has a 1st phase consisting of a 3D printed, rigid grid, and a soft silicone rubber 2nd phase. (c) Schematic of a Macro-DN composite. Features are listed with their specific design parameters. (d) Force-stretch curves of a grid-shaped skeleton (purple), neat silicone rubber (pink), and their resulting Macro-DN composite (black). The insets (i)-(vii) represent snapshots of the composite sample corresponding to the stretch shown in the loading curve. Yellow dashed lines represent internal fracture events and local deformation.

Table 3. Analysis of representative tensile tests for the skeleton, matrix, and fabricated composite. The skeleton utilized had a length of 34 mm consisting of 9 sections, each with a cross-sectional area of 0.58 mm^2. Sacrificial bond length was 2 mm. Volume fraction of rubber was 0.85. The matrix has a thickness of 1.5 mm. Specific geometric parameters can be seen in **Figure 1** and **Figure 2**.

Component	Stiffness, k (N/mm)	Fracture Stretch, λ_x (mm/mm)	Fracture Force, F_x (N)	Work to Fracture, W (mJ)
Skeleton	28.8	1.03	19.8	11
Matrix	0.51	2.71	21.2	560
Composite	32.2	2.66	21.9	850

The mechanical response of the Macro-DN composite can be analyzed by comparison to traditional DN hydrogels. The stiffness of the sample at small stretch is controlled by the stiffness of the skeleton (macro-scale 1st network), resulting in an increase in stiffness of ~60. After fracture of this network, the composite undergoes yielding and enters a ductile region. In this region, ranging in stretch from about 1.2 to 2.5, The average force is 14.8 ± 2.5 N, with the force oscillating between a relative minimum (relaxation after a fracture event) and relative maximum (prior to fracture of the skeleton). In the ductile region, the sample experiences permanent fracture of the 1st network as a function of stretch. Once the entirety of the sample has undergone necking, the sample will fracture through the matrix (macro-scale 2nd network). This fracture event occurs near the same stretch as that of the independently tested matrix component (λ_x ~ 2.7). **Table 3** contains the complete mechanical properties of the skeleton, matrix, and Macro-DN composite.

We can analyze the energy dissipated of each phase by integrating the area under the force versus displacement curves to determine the work to fracture, *W*. During stretching

of the skeleton in **Figure 3d**, 11 mJ of energy is dissipated due to the fracture of 3 sacrificial bonds that make up one section. Fracture of the neat matrix required 560 mJ, and the energy required to fracture the composite structure was 850 mJ. Given that each section of the frame underwent fracture in the composite, a total of 9 sections containing 27 sacrificial bonds fractured, requiring ~100 mJ of energy. However, we can see that the resulting composite required 250 mJ more energy than the simple sum of the sacrificial bond energy plus the stretching of the matrix, demonstrating a synergistic increase in the toughness of the composite structure. The increase in toughness of these composites is not limited to just the addition of sacrificial bonds that dissipate energy when they break; the fracture process itself increases the dissipation of the matrix as well due to localized large deformation of the matrix in the fractured section. This matches the response of DN hydrogels, where the introduction of the 1st brittle network dissipates energy not only by fracturing covalent bonds, but also by supporting large local deformation of the 2nd network in regions where 1st network fracture occurs. A similar process is shown here: only a minority of the energy dissipated can be attributed to fracturing of the sacrificial network, and we therefore conclude that the presence of the sacrificial network also increases the dissipation in the silicone rubber matrix.

Another unique feature of DN hydrogels is that they exhibit significant hysteresis during cycling due to fracture of the sacrificial 1st network.[59] **Figure 4** demonstrates cycle testing with increasing stretch for Macro-DN composites. **Figure 4a** demonstrates cyclic testing of the neat silicone rubber component, while **Figure 4b** charts the energy dissipated during each cycle. Hysteresis energy is calculated by the difference in the loading energy and the unloading energy. At small λ, the material exhibits strongly elastic properties, with loading and unloading curves virtually overlapping. As λ increases, the amount of energy dissipated increases, likely due to friction between polymer chains, or

the onset of chain fracture due to finite extensibility of the network. These results are drastically different than those seen in the cyclic tests of the Macro-DN sample, shown in **Figure 4c**. Initially, the sample is very stiff, and when the force surpasses about 15 N, fracture of the reinforcing skeleton occurs. This fracture process causes the elastomer in the activated section to stretch, while the remaining sections keep their initial geometry. Interestingly, as presented in **Figure 4d**, the energy dissipated in the 2nd cycle (~100 mJ) of the Macro-DN composite exceeded that of the final, largest applied stretch of the neat rubber (~85 mJ). In other words, the composite dissipated as much energy at $\lambda = 1.2$ as the neat elastomer dissipated at nearly $\lambda = 2.6$. Neat silicone rubber only dissipates significant energy at high λ, close to λ_x. Due to localized stretching from the Macro-DN architecture, high *local* stretch is achieved at low *global* stretch. This design results in a material that is capable of dissipating large amounts of energy, even at small stretches, through fracture of a sacrificial network which controls local deformation.
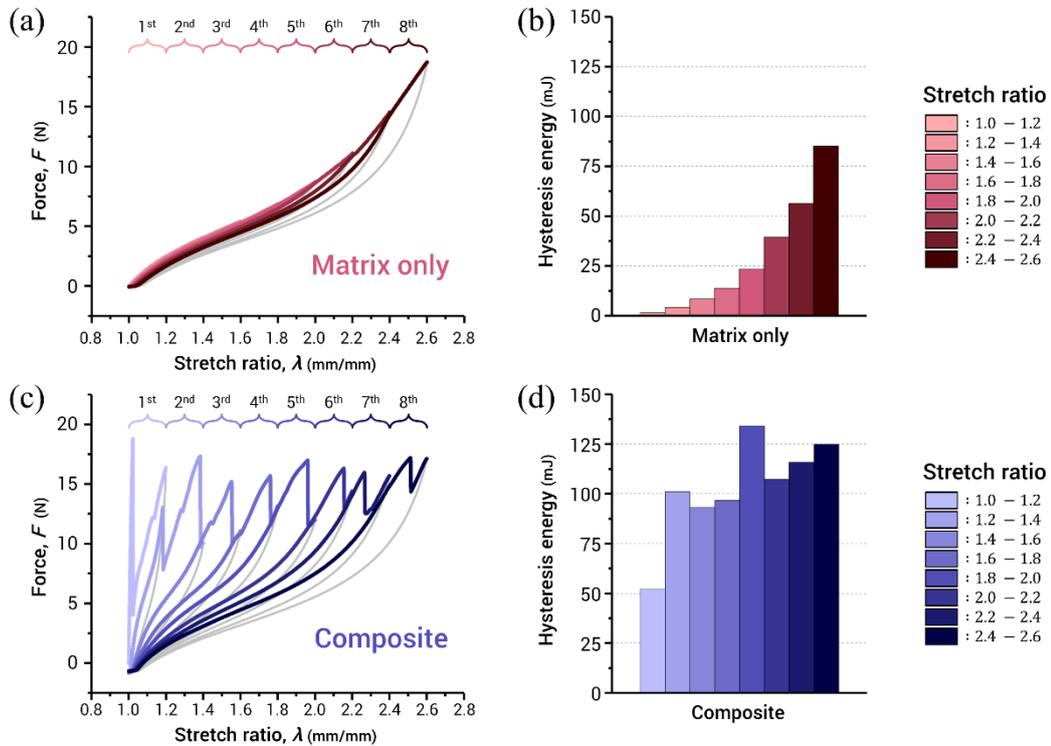
Figure 4. Analyzing energy dissipation via cyclic testing of the matrix and Macro-DN composite. Force versus stretch ratio curves during cyclic testing with repeatedly increasing stretch, and the hysteresis energy during each cycle are shown for the matrix ((a) and (b), respectively) and Macro-DN composite ((c) and (d), respectively). The neat matrix does not dissipate large energy until high stretch. The Macro-DN composite dissipates large amounts of energy, even at small stretch due to preferential fracture of the macroscale sacrificial network.

Interestingly, during the cyclic loading curves in **Figure 4c,** the force never exceeded a value of approximately 18 N. As the force approaches this value with the addition of stretch, the rigid skeleton will fracture, causing a decrease in force. The Macro-DN composite design acts like a "mechanical fuse." For these materials, if the force applied exceeds a given force determined by the skeleton design, fracture and additional displacement will occur, rather than an increase in force. This could be a useful design for shock sensitive applications, whereby tuning the mechanical properties of the composite can allow for programmable maximum force values within a given displacement range.

3.3.2 Expression of the DN principle through optimized component strength

In DN hydrogels, the yield stress is controlled by the properties of the 1st network,[37] and similarly we can control the yield force of Macro-DN composites by tuning the strength of the reinforcing skeleton. To change the fracture force, F_x, of the skeleton, we changed the nominal width of the sacrificial bonds of the skeleton structure from 0.45 mm to 1.2 mm, which resulted in cross-sectional areas, A_{cs}, ranging from 0.26 mm^2 to 1.04 mm^2 per section (**Figure 6a,** skeleton specifications are shown in **Table 1**). As A_{cs} increases, F_x increases proportionally (**Figure 5**). The force versus stretch curves for composites made with these skeletons can be seen in **Figure 6b**, along with an inset of the low stretch region in **Figure 7**. For the sample with the weakest sacrificial bonds, a ductile response with a sawtooth fracture pattern can be seen from a stretch of 1.0 to 1.5, and the nine peaks demonstrate complete fracture of all sacrificial bonds. After the bonds are completely fractured, the stress increases in the remaining intact matrix, until global fracture occurs at a stretch of about 2.75, matching λ_x of the silicone rubber matrix (**Figure 3d**). As the fracture strength of the incorporated skeleton increases, two noticeable changes occur, which are outlined in **Figure 6c**. First, the average F_x during rupture of the sacrificial bonds increases (internal fracture events denoted as circles and the average force as a dotted line). This occurs because the higher strength of the sacrificial network requires more force to fracture. Second, the stretch range over which sacrificial bond fracture occurs increases with increasing strength, until the $A_{cs} = 0.58$ mm^2 sample, where sacrificial bond fracture occurs until matrix rupture (denoted as an X in **Figure 6c**). Stiffer skeletons require higher force to fracture, and therefore greater stretch between fracture events is required. When the width of the skeleton is further increased ($A_{cs} = 0.83$, 1.04 mm^2), only one fracture event occurs, resulting in highly brittle composites with reduced fracture stretch. The optimized skeleton geometry for samples

37

of this size were determined to have a sacrificial network with $A_{cs} = 0.58$ mm^2, resulting in a composite with high stiffness and high toughness, while maintaining ductile characteristics. These results suggested that internal fracture events and fracture strength of the skeleton as the sacrificial bonds are keys for toughening due to the DN principle in Macro-DN materials.
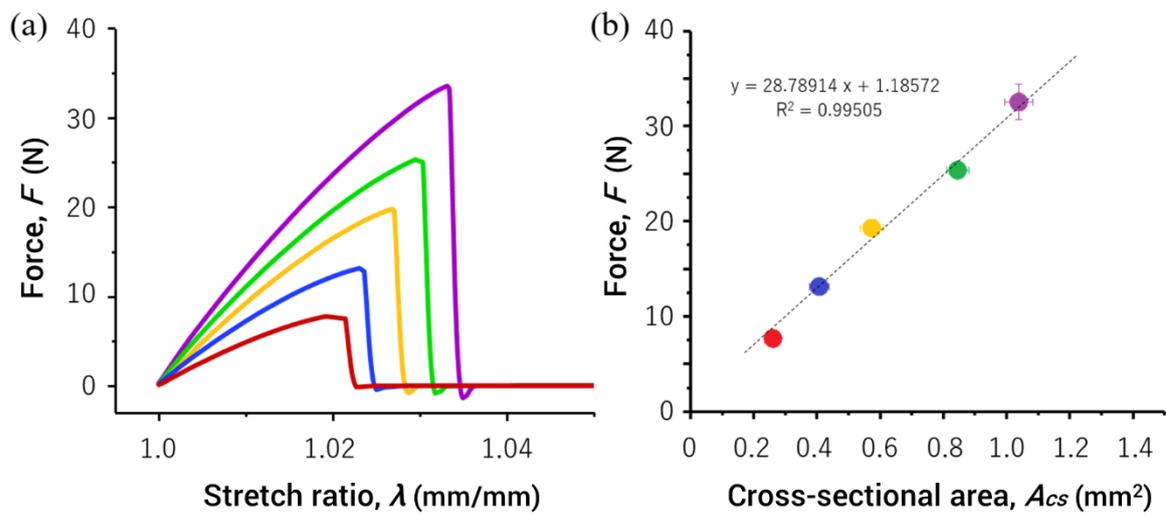

Figure 5. Mechanical analysis of the rigid skeleton. (a) Force versus Stretch ratio curves for skeletons of increasing cross-sectional area. (b). Corresponding fracture force as a function of cross-sectional area.
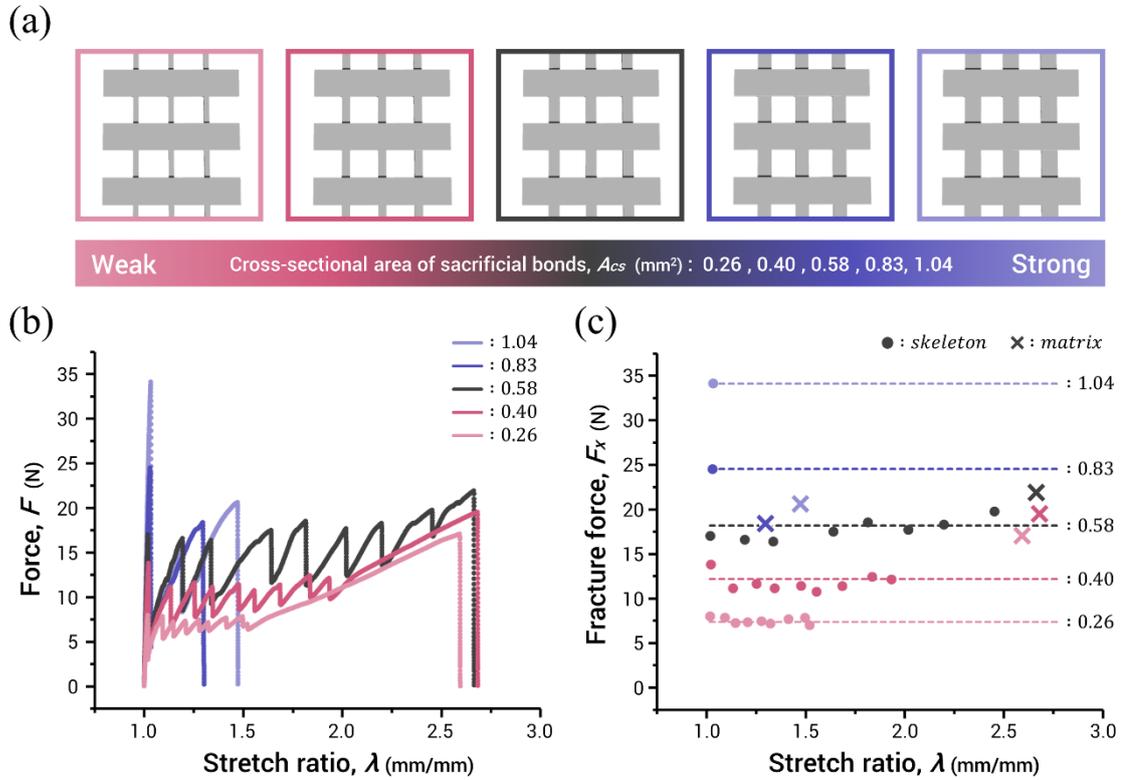
Figure 6. Tuning the mechanical response of Macro-DN composites by modifying the geometry of the sacrificial skeleton. (a) Schematic illustrations of the tested geometries of grid-shaped skeletons used in the Macro-DN composites. (b) Typical force versus stretch curves of the composites with varying geometry of skeletons. The legend values are the cross-sectional area per section of vertical grid. (c) Fracture forces measured during a tensile test, either due to skeleton fracture (circle) or matrix fracture (cross). Fracture of the matrix occurred when the sample failed.

Figure 7. Inset of the low stretch region of Figure 6b. As cross-sectional area of the skeleton increases, the stiffness and yield strength of the composite also increases.

39

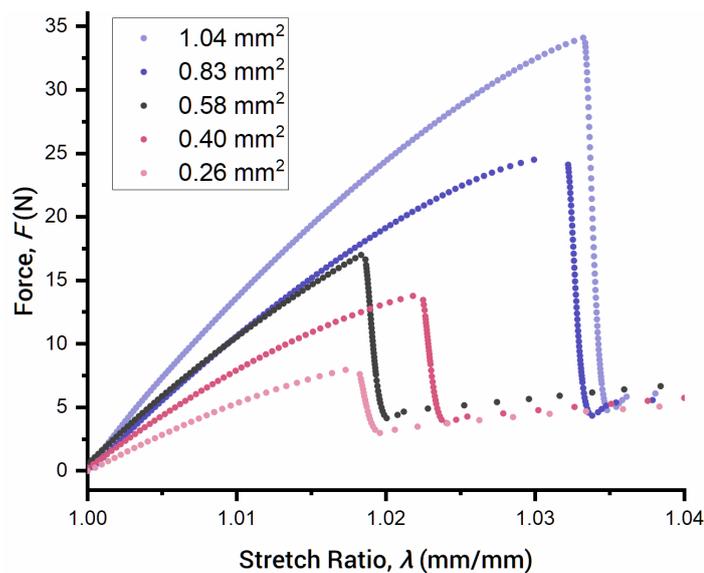A powerful result of multi-step internal fracture is that Macro-DN composites are able to overcome weaknesses in the reinforcing skeleton. **Figure 8** demonstrates a sample where the skeleton sections contain varying A_{cs}, from 0.26 mm^2 to 1.04 mm^2. When stretched, fracture occurs first in the sections with $A_{cs} = 0.26$ mm^2. However, rather than failing at $F_x = 8$ N (denoted by the pink line, the fracture force of the $A_{cs} = 0.26$ mm^2 skeleton), force is transmitted to the matrix, allowing the next stiffer sections to fracture. This process continues until matrix rupture. Since the fracture force of the $A_{cs} = 0.83$ mm^2 and 1.04 mm^2 sections exceeds that of the matrix, they cannot fracture, and l_x occurs at reduced stretch. Multi-step internal fracture results in materials that are flaw-resistant and can overcome defects. Furthermore, by tuning A_{cs}, we have a method to tune the shape of the loading curve, especially useful in biomaterials where "J-shaped" curves are desired.[60]
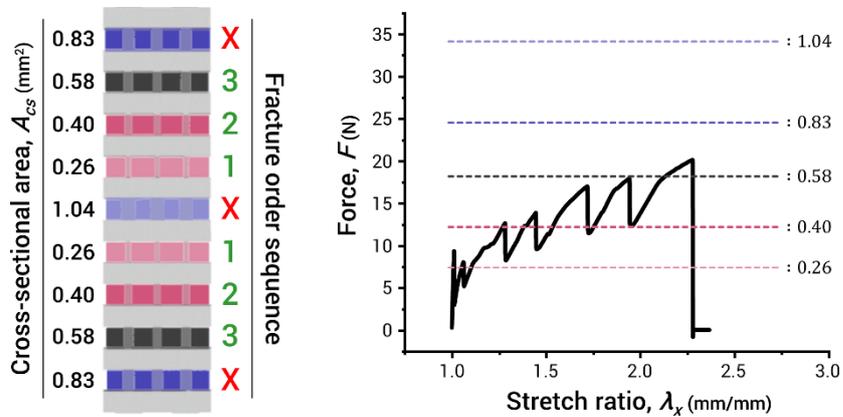
Figure 8. Force versus stretch ratio curve for a Macro-DN composite containing sections with varying cross-sectional area, A_{cs}, as shown on the left. Colored lines on the plot represent the fracture force for sections of corresponding A_{cs}. The weakest sections fracture first, followed by stronger sections, as denoted by the fracture order sequence. Sufficient force is not generated to fracture some sections ($A_{cs} = 0.83$ mm^2, 1.04 mm^2), denoted by a red X.

To understand the ductile-brittle transition, we compared the observed fracture behavior of the composites to the mechanical strength of the reinforcing skeleton. In **Figure 9a**, the strength of skeletons with varying A_{cs} are plotted (symbols), along with

the strength of the silicone rubber matrix (green line). When the fracture force of the matrix exceeds the fracture force of the skeleton, multi-step internal fracture occurs (pink symbols) whereas when the fracture force of the skeleton is greater than the matrix, only single-step fracture occurs (blue symbols). If we examine the samples at the moment prior to fracture (**Figure 9a** insets), we see that the samples that underwent multi-step internal fracture were dramatically deformed and all sacrificial bonds were broken, while the single-step internal fracture samples have only one cracked region, lacking global damage. Based on these qualitative results, we conclude that the expression condition of DN principle in macroscale double networks is multi-step internal fracture, which occurs when the fracture strength of the matrix exceeds that of the reinforcing skeleton.

From the photographs in **Figure 9a**, we see that multi-step internal fracture allows for higher λ_x than single-step internal fracture. These results are quantified in **Figure 9b**. In the multi-step (pink) region, λ_x approaches 2.75, but when the grid to matrix strength ratio goes above 1, λ_x dramatically decreases to below 1.5 (blue region). In **Figure 9c**, we plot the work to fracture, W, of the composite samples, which was calculated by integrating the force versus displacement curve. When weak skeletons are used, there is little change in the overall W. The introduction of a weak skeleton does not dramatically increase the force during stretching but may consequently introduce defects within the matrix to nucleate fracture. W reaches a maximum when the skeleton to matrix strength ratio approached 1. If the skeleton strength to matrix strength is further increased, W dramatically drops, because the matrix is unable to deform to dissipate energy. These results show that the ratio of skeleton strength to matrix strength is the key factor governing the ductile-brittle transition of the DN composites, and that the optimization point for stretchability and energy dissipation lies at a ratio of one.
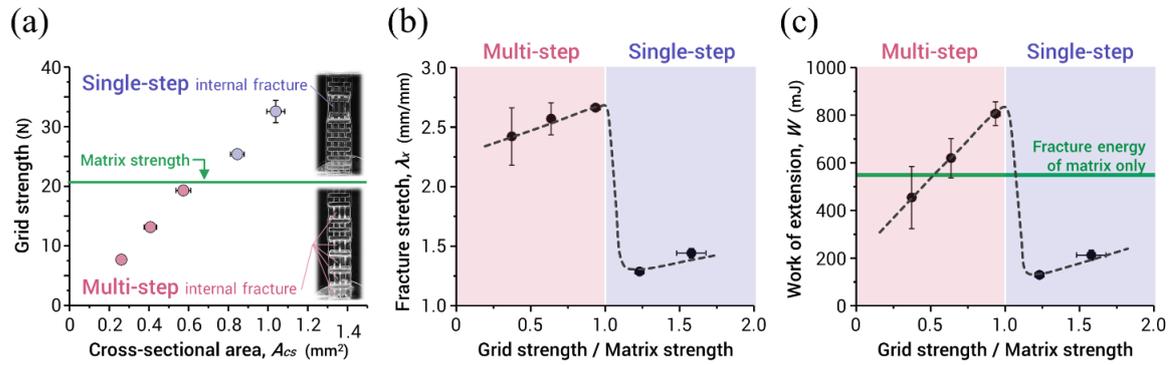
Figure 9. Ductile-brittle phase transition of the Macro-DN composites. (a) Fracture strength versus cross-sectional area for the 3D printed grid skeleton and the silicone rubber matrix. The insets represent images of multi-step and single-step internal fracture. (b) Stretch-at-break versus the grid to matrix strength ratio for the composite samples. A transition occurs when the strength ratios reach 1. (c) Work of extension versus the grid to matrix strength ratio. The highest work of extension occurs at a grid to matrix strength of 1. Tests were performed at least 5 times, and error bars represent standard deviation. Data points without error bars have error less than the symbol size.

3.3.3 Toughening based on the DN principle through topological interlocking

Usually, the interface between the reinforcing phase and the matrix plays an important role in composite materials. This is especially true in macroscale composites or laminated structures, where delamination can quickly result in composite failure. In previous work on Macro-DN composites based on fabric and VHB tape, force transmission occurred primarily due to adhesion between the two phases.[58] As the sample stretched, the fabric fractured and the magnitude of force transmitted from the rubber to the fabric continuously diminished. At some point, the force transmitted was not great enough to fracture the fabric, and this was followed by rupture of the VHB tape matrix. In our experiments, a grid shape was chosen because it allows for the transmission of force between the matrix and skeleton via topological interlocking as well as by interfacial adhesion, resulting in a composite that does not easily delaminate. Understanding the roles of interfacial adhesion and topological interlocking is important toward optimizing the design of macroscale double network structures.

42

To understand the role of interfacial adhesion, we designed an experiment to measure the adhesive strength between the silicone rubber and the skeleton (**Figure 10a**). A rigid rod of 3D printed plastic was embedded in silicone rubber with lengths of 5, 7, 10, and 16 mm, with a constant A_{cs} of 0.4 mm^2. The silicone rubber was clamped with the bottom grip of the tensile tester, and the rod was displaced at 50 mm/min. The force versus displacement curve can be seen in **Figure 10b**. The force increased, until slipping occurred and then the force dropped nearly to 0 N as the rod was pulled out of the rubber. From the peak force, we normalized by the surface area of the rod to determine the maximum adhesion strength. The average adhesive shear stress, σ_a, of the four lengths tested was 0.24 MPa (**Figure 10c**). This stress is exerted by the matrix on the skeleton, and therefore specimens with longer sacrificial bond lengths are expected to reach higher force in the skeleton during stretching. The force applied to the skeleton, F_s, can be calculated as:

$$F_s = L_s P_s n_s \sigma_a$$

where L_s is the sacrificial bond length, P_s is sacrificial bond perimeter, and n_s is total number of sacrificial bonds. For a fixed P_s (1.98 mm) and n_s (3), and using σ_a as calculated above, F_s is estimated as a function of sacrificial bond length in **Figure 10d**. The strength of the skeleton was experimentally measured as 16 N. From the plot in **Figure 10d**, the adhesion force exceeds this value at a critical length, $L_{s,c} \sim 11.5$ mm. If the sacrificial bond length is greater than this value, multiple fracture events can occur within one sacrificial skeleton section due to adhesive force transfer. To test this claim, a sample was prepared with only one section ($S = 1$), containing sacrificial bonds with $L_s = 34$ mm (**Figure 10e**). In this sample, force can only be transmitted by interfacial adhesion. Upon close examination of the tensile tests for this specimen, we see that the initial

fracture of the sacrificial network occurs at low stretch, immediately after the test begins. After this the force drops, but begins to increase again, and at above $\lambda = 1.5$, additional fracture events occurred within the already fractured section, due to adhesive force transmission. However, after three fracture events no additional internal fracture occurred and the sample failed globally. This starkly contrasts with the fracture process of the specimen tested in **Figure 10d**, where a sample of identical length contained $S = 9$ sections and underwent nine fracture events. Despite possessing very short sacrificial bonds ($L_s = 2$ mm), multi-step fracture could occur because force was transmitted by the interlocking design. Because the adhesion between the matrix and skeleton is relatively weak, the impact of changing the number of bonds per section, n_s, is negligible. In **Figure 11**, we demonstrate that when $n_s = 5$ without changing A_{cs} the resulting $L_{s,c}$ decreases slightly to 9.7 mm. For the highest performance sample where L_s is very short, force transfer still occurs due to topological interlocking. These results suggest that the increase of multi-step internal fracture due to topological interlocking is the factor for the toughening condition of DN principle and clearly demonstrate the importance of a design that enables topological interlocking, since fracture can occur even when adhesion force between phases is low.
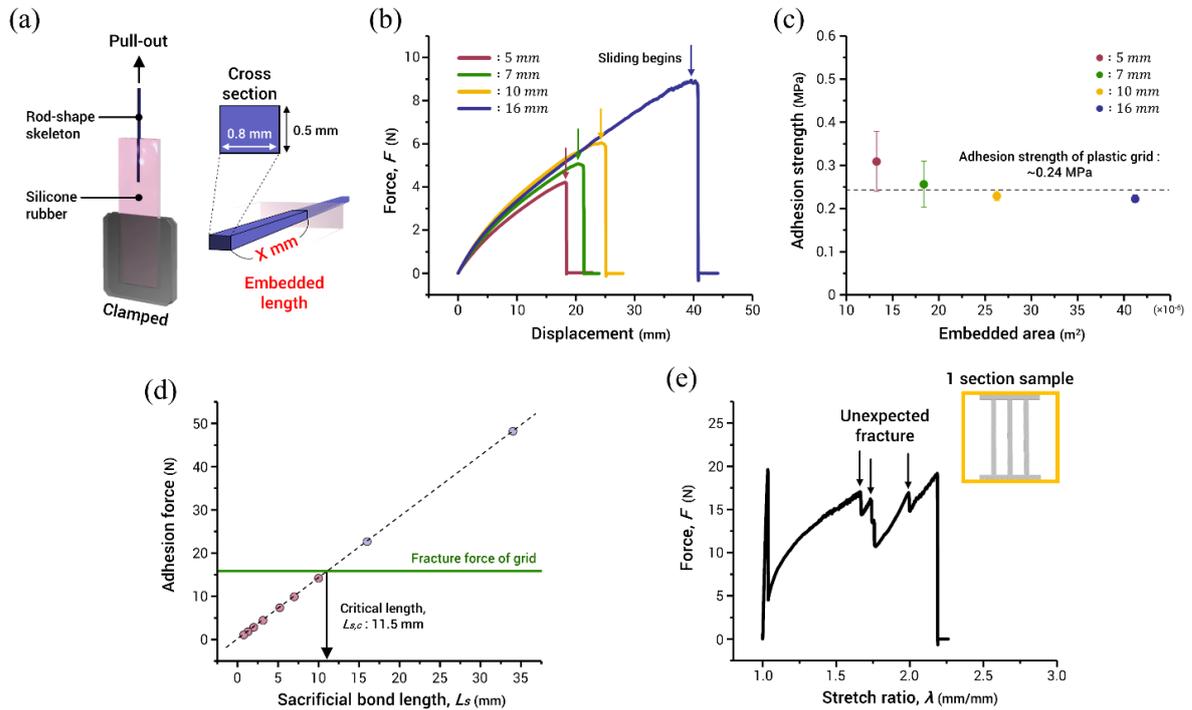
Figure 10. Investigation of adhesion strength between the 3D printed skeleton and silicone rubber.
(a) Schematic of the test setup used to determine the adhesion strength between the silicone rubber and the 3D printed plastic. A rigid rod of length, *x*, was embedded in silicone rubber, and both the silicone rubber and the rod were gripped by opposing ends of a tensile tester. Displacement occurred at a rate of 50 mm/min. (b) Force versus displacement curves for rods of varying embedded length. Once the rod began to slide the force dropped to nearly 0 N and the test was ended. (c) Measured adhesion strength as a function of embedded surface area. (d) Calculated adhesion force, as a function of sacrificial bond length for grid sections containing a sacrificial bond cross section of 0.58 mm^2. The critical length of 11.5 mm represents the transition between fracture due to interfacial adhesion and topological interlocking. (e) Force versus stretch ratio curve for a sample containing only one section. Multiple fracture events are seen, due to the sufficiently strong adhesion force between the skeleton and the matrix.
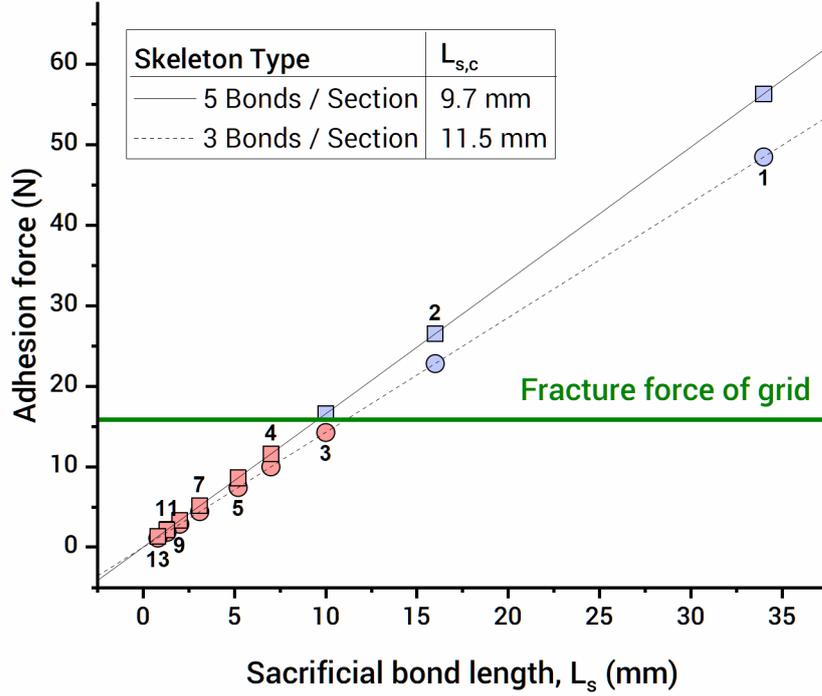
Figure 11. Adhesion force versus sacrificial bond length, L_s, for samples with 5 sacrificial bonds per section, compared to 3 sacrificial bonds per section. This causes the transition from topological to adhesive force transfer to occur at shorter bond lengths. The numeric labels represent the number of sections per 34 mm-long sample.

Next, we wanted to optimize energy dissipation by increasing the total number of fracture events. Samples with varying section number, S, from 0 (neat matrix) to 13 were fabricated. Since nominal length is fixed, when S increases, L_s must correspondingly decrease (**Table 4**). The force versus stretch ratio curves for representative specimens are shown in **Figure 12a**. As the L_s decreases and S increases, the frequency of the sawtooth pattern during yielding also increases, but λ_x does not significantly change. With decreasing L_s, the local stretch per given displacement increases, causing the force to rise quickly and more fracture events occur within the same total displacement. This causes the average force during the yielding region to increase, consequently resulting in increased energy dissipation.

For a simple elastomer, the force-displacement curve takes on a generally triangular shape, and the work to fracture can be approximated as $W_0 = 0.5 * F_x * \delta_x$. We envision that

the force versus stretch curve for a Macro-DN composite containing an infinite number of sections would be a square shape (**Figure 12a**, bottom). To achieve this shape, stiff reinforcement is needed to quickly achieve a loading force near the fracture strength of the matrix. Fracture should occur quickly and repeatedly, so that the average force during the yielding region remains close to the maximum yield strength. Finally, fracture should occur at the same stretch-at-break as the neat matrix. This fracture process would then approach a value of $W_{max} = F_{yield}*\delta_x$, where F_{yield} is the average peak force in the yielding region. In **Section 3.3.2**, we characterized the important factors in maximizing yield force, and in an optimized state $F_{yield} = F_x$ for a given matrix. Based on this model for a linear elastic matrix, we predict a 100% increase in work of extension is likely an upper bound for this type of composite system.
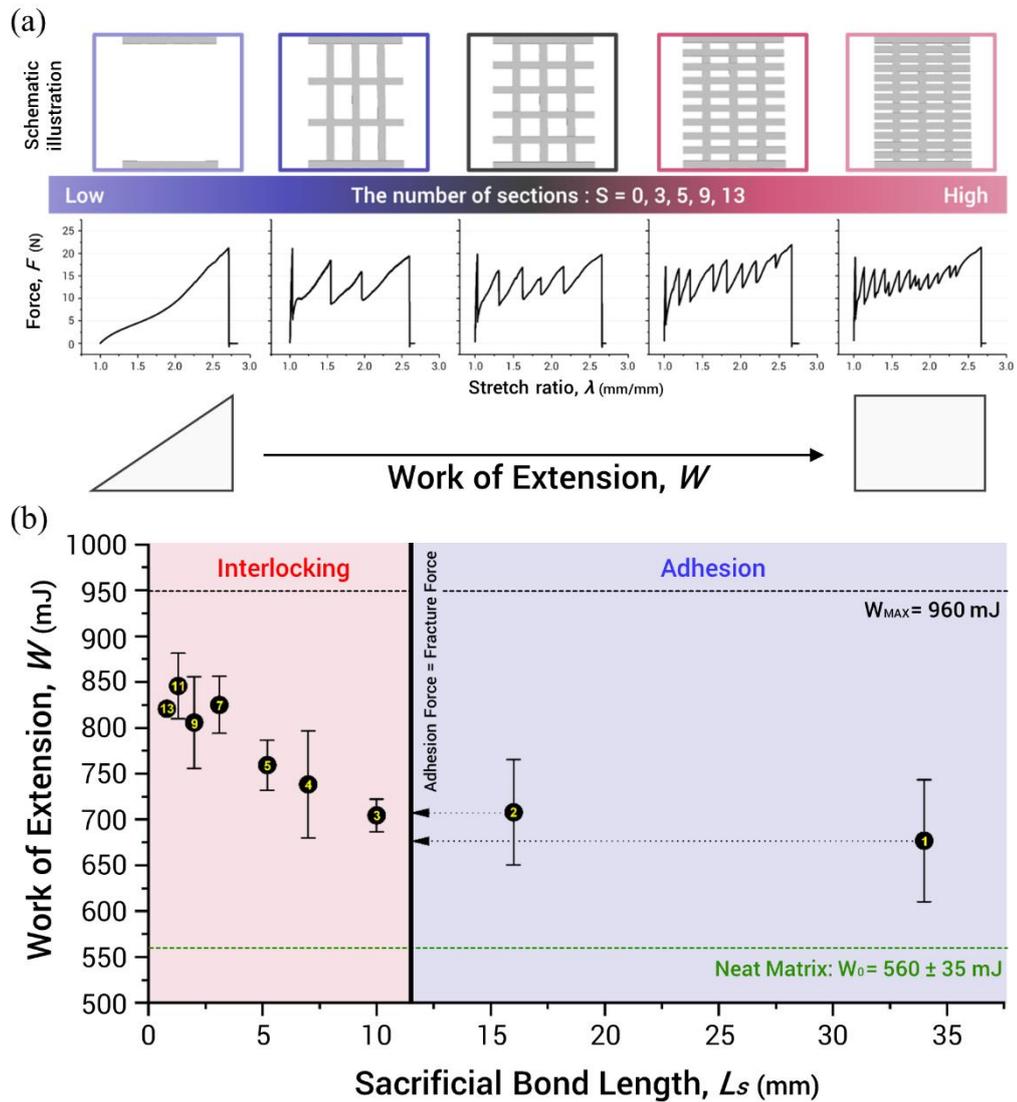
Figure 12. Effect of skeleton density on the toughness of Macro-DN composites. (a) The number of sections, S, was increased from 0 to 13. Schematics of these designs are shown with representative force versus stretch ratio curves. As the density of sacrificial bonds increases, the shape of the curve changes from a triangle to a rectangle, with nominally the same stretch ratio, representing an approximate doubling of the work of extension. (b) The work of extension as a function sacrificial bond length. The black line represents the transition in the dominant force transmission mechanism: at short sacrificial bond lengths topological interlocking plays is essential, and at long sacrificial bond lengths interfacial adhesion is important. The numbers in the symbols are the number of sections, S. The green dashed lined represents the work of extension of the neat matrix. The black dashed line represents the maximum work of extension,

Table 4. Details of the properties of composites made with varying number of sections containing sacrificial bonds.

Number of Sacrificial Sections for a constant sample length, S	Number of Fracture Events	Bond Length, L_s (mm)	Matrix Volume Fraction, φ	Work of Extension, W (mJ)	Increase in Work of Extension*, $(W-W_0)/W_0$	Toughening Efficiency*, $(W-W_0)/(W_{max}-W_0)$
1	3	34.0	0.96	680 ± 67	21%	29%
2	3	16.0	0.95	710 ± 58	26%	37%
3	3	10.0	0.93	700 ± 18	26%	36%
4	4	7.0	0.92	740 ± 59	32%	44%
5	5	5.2	0.90	760 ± 27	36%	50%
7	7	3.1	0.88	830 ± 31	47%	66%
9	9	2.0	0.85	810 ± 50	44%	61%
11	11	1.3	0.82	850 ± 36	51%	71%
13	13	0.8	0.79	820 ± 6	47%	65%

*: $W_0 = 560$ mJ is the work to fracture of neat matrix, $W_{max} = F_{yield}*\delta_x = 960$ mJ.

In **Figure 12b**, the work to fracture, W, versus the sacrificial bond length, L_s, is plotted, with the number of sections, S, inscribed within each symbol. The green dashed line represents W of the neat matrix, $W_0 = 560$ mJ. The vertical black line at 11.5 mm represents the critical sacrificial bond length $L_{s,c}$ at which the adhesion force equals the fracture force of the skeleton. When L_s is greater than or near $L_{s,c}$, fracture occurs independently of section number; hence, samples with 1-3 sections exhibit similar W. When L_s is less than $L_{s,c}$, each section exhibits only one fracture event, due to topological interlocking, and as L_s decreases and S increases, more energy is dissipated. We ultimately measured a maximum work of extension of $W = 850$ mJ, in a sample containing $S = 11$ with $L_s = 1.3$ mm. This result represents a 51% increase in W compared to the W_0, due to the implementation of macroscale sacrificial bonds with topological interlocking. In samples where force transmission occurs primarily by interfacial adhesion (1-3 section samples), the average increase in W is only 24%. These results demonstrate the importance of topological interlocking in creating robust Macro-DN composites due to the DN principle.

We estimate that the maximum theoretical work of extension for this system can be calculated from $F_{yield} = 16$ N and $\delta_x = 60$ mm ($\delta_x = initial\ length * \lambda_x$), resulting in $W_{max} = 960$ mJ (black dashed line in **Figure 12b**). To calculate the toughening efficiency, we compared the true increase in work of extension ($W - W_0$) to the maximum potential increase in work of extension ($W_{max} - W_0$). The results are tabulated in **Table 4.** When $S = 11$, the highest toughening efficiency, 71%, was measured. Interestingly, even with optimized grid strength, when $S = 1$ a toughening efficiency of just 29% was observed. There are a few reasons why a toughening efficiency of 100% was not achieved. The calculation of W_{max} assumes that there is no decrease in force between the fracture of subsequent sections; effectively the calculation assumes an infinite number of fracture

events, which causes F_{yield} to be maintained for the duration of the yielding region. Furthermore, it assumes that the force will not increase after all the sacrificial sections are activated. Finally, as S increases the volume fraction of matrix, φ, decreases (see **Table 4**).

Previous work agrees with our finding that to make robust composites, topological interlocking is essential. Experiments performed on molecular-scale double networks, have shown that strong intermolecular interactions are not required to create double network structures; topological interlocking is sufficient to dramatically enhance mechanical properties via the interpenetrated double network structure. Furthermore, hydrogels and elastomers can achieve strong bonding through topology at either the molecular-scale[61–63] or macro-scale.[64] Ultimately, we see in Macro-DN systems that the incorporation of topological interlocking at large length scales also results in a dramatic increase in material toughness. Importantly, force transmission by topological interlocking makes developing Macro-DN composites using various soft and hard materials possible.

3.3.4 Universal application of Macro-DN composites

Specific materials chemistry is not required to create Macro-DN composites; as long as the guiding mechanical parameters are followed, specifically that the fracture strength of the matrix exceeds the strength of the reinforcement and the design incorporates topological interlocking, components consisting of any type of material can be used. **Figure 13** contains examples that demonstrate the universality of this concept. **Figure 13a** (wood) and **Figure 13b** (foamed polystyrene; Styrofoam) demonstrate two other materials used as reinforcing phases within a silicone rubber matrix. In both cases the toughness increases along with the introduction of yielding, without influencing λ_x. For the Styrofoam sample, the irregular foamed structure likely causes additional fracture

51

events to occur at smaller length-scales, due to increased topological interlocking, which prevents the immediate stress relaxation and significant saw-tooth pattern seen with other material combinations. In **Figure 13c**, natural rubber is used as a matrix. After the yield point, when the force begins to rebuild, the slope has positive concavity, compared to the linear slope seen in silicone rubber samples. At high stretch, natural rubber exhibits significant strain hardening. During each internal fracture event, the rubber locally stretches to high strain, and therefore during each fracture event strain hardening is apparent. This opens up the possibility that this design could be used to create high performance materials by locally taking advantage of viscoelastic behaviors of designer polymers. Natural rubber is one of the toughest soft materials known, and generally represents an upper bound of toughness through intrinsic toughening. This method demonstrates that even the toughness of natural rubber can be improved by using a macroscale double network design. The use of metals as a sacrificial phase has been previously demonstrated,[13,16,65] and the use of ceramics in the sacrificial phase has strong potential due to their high stiffness and brittleness. We expect that Macro-DN composites containing metals and ceramics to play an important role in future functional materials designs. For materials that demand high energy dissipation, the macroscale double network method may universally enable higher performance with relatively minor changes in bulk materials.
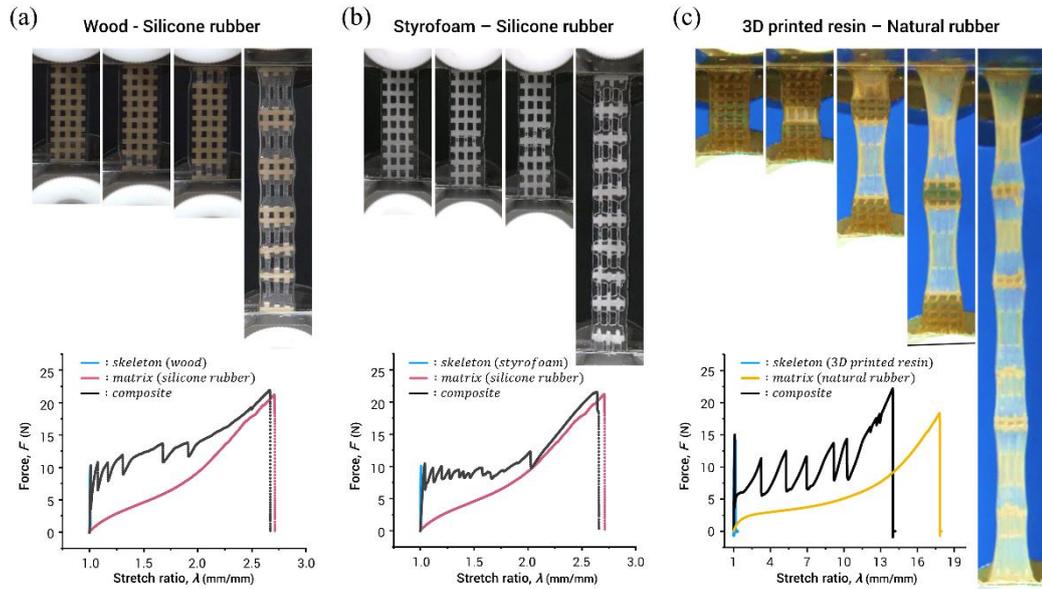
Figure 13. Demonstrating the universality of the macroscale double network effect by creating composites with a wide range of materials. (a) A composite comprised of wood and silicone rubber. (b) A composite comprised of Styrofoam and silicone rubber. This design lacks the obvious sawtooth fracture pattern of other designs, likely due to stronger topological interlocking due to the foamed structure. (c) A composite comprised of a 3D printed skeleton and natural rubber.

3.4 Conclusions

Enhanced toughness can be achieved in soft composite structures by following design principles extrapolated from our knowledge of DN hydrogels and elastomers. Specifically, these composites are designed by integrating a rigid skeleton with high strength but a relatively low fracture force into a stretchable matrix. When stretched, force from the matrix causes the skeleton to fracture multiple times prior to global sample fracture. This matches the fracture mechanism inferred from DN hydrogels, where a stretchable 2nd network causes the brittle 1st network to fracture, resulting in yielding prior to global fracture. We have shown that the strength ratio between the skeleton and matrix governs multi-step, ductile versus single-step, brittle deformation. As the strength of the skeleton approaches that of the matrix, the yield force reaches a maximum, and the yielding region extends in length, close to the ultimate fracture stretch of the composite, resulting in an

optimized design. When these conditions are optimized, the DN principle is expressed in Macro-DN materials. By studying the force transmission mechanisms, we determined that topological interlocking is essential for toughening due to DN principle. Utilizing topological interlocking, a significant increase in sacrificial bond density is achieved, reaching ~70% of the theoretical maximum toughness, compared to ~30% for the adhesion-only compositions. This mechanism also matches DN hydrogels, where topological interpenetration is more important than inter-network interactions. Because topological interlocking of the two phases provides sufficient force transmission, we demonstrate that the macroscale double network design is universal, and can be applied to wide range of materials, even if interfacial adhesion strength is poor. From this, our Macro-DN composite has shown to be an effective model for understanding phenomena in DN materials over a wide range of scales. In the future we hope this simple model provides not only a promising avenue for the design and development of Macro-DN materials, but also introduces a very effective system for understanding other unexplored phenomena in DN materials at all length-scales.

CHAPTER 4

Investigating the Defect-Insensitive Nature of Double-Networks using Macro-scale Double-Network Materials

4.1 Introduction

The mechanical properties of DN hydrogels are superior to their individual components (**Figure 1a**). When tested independently, the 1st network is stiff but brittle, while the 2nd network is soft and ductile, with neither network capable of dissipating significant energy.[24] The DN principle occurs through the preferential rupture of the covalent bonds of the sacrificial 1st network over a wide area during stretching.[6,7,35] Because fracture of the 2nd network does not occur until substantial widespread damage has occurred within the 1st network, a significant amount of energy can be dissipated. Beyond increasing toughness, the fracture stress and stretch of the DN hydrogel is also significantly higher than that of the 2nd network that makes up the vast majority of the composite and ultimately initiates sample failure. This result poses an interesting question: how can such significant stress and stretch evolve if it cannot be obtained with either network independently?

As introduced in **Chapter 2**, some current research has attempted to uncover the origin of the superior properties of DN hydrogels. At the current stage, these phenomena are believed to be caused by the unique internal structure of DN hydrogels. These results therefore cannot completely explain the origin of the unique DN phenomena, and macroscale models provide a simple method to explore this problem.

Materials with a single network structure are sensitive to internal defects and fracture quickly. This fact can be easily demonstrated by comparing the mechanical results of a hydrogel or elastomer in its pristine form, versus the same material when a defect, such as a notch, is added.[66] The addition of a defect significantly decreases both stress and

stretch.[67,68] We hypothesize that the two interpenetrating networks within a DN material can suppress the impact of each other's intrinsic defects, allowing their potential mechanical properties to come to light. To simply demonstrate this point, we utilized the Macro-DN materials framework introduced in **Chapter 3**. Macro-DN composites are materials that consist of two components that match the essence of the 1st and 2nd networks of DN hydrogels, essentially extending the molecular-scale networks of DN hydrogels to the macroscale. In **Chapter 3**, we were able to elucidate the conditions in which the DN principle is expressed on the macroscale, indicating that this Macro-DN material can be a useful simple model for understanding unexplained phenomena in DN materials in general. However, these Macro-DN materials have one notable difference in mechanical response when compared to molecular DN hydrogels: the yield force of the Macro-DN material was equal to the fracture force of the 1st network and the fracture force and fracture stretch of Macro-DN material was equal to that of the 2nd network (**Figure 1b**). Understanding what enables the mechanical properties of DN hydrogels to surpass the individual components is of utmost importance to unraveling the mysteries of the DN concept.

In this Chapter, we demonstrate that DN materials are capable of ignoring defects, enabling them to match the mechanical properties of their "perfect" defect-free counterparts. The mechanical properties of defect-free and defect-containing double-networks are compared by creating simple Macro-DN materials consisting of a silicone rubber matrix and a 3D-printed hard thermoset skeleton. The mechanical properties of the Macro-DN material are first modeled using a simple analytical model. To verify this model, mechanical properties are measured experimentally. Defects in the skeleton are implemented by changing the location of sacrificial bonds within the skeleton to create an inhomogeneous structure, without changing the total number of sacrificial bonds.

Defects are introduced into the matrix through a pre-notch that localizes stress. The presence of inhomogeneity results in two important conclusions: 1) when the local skeleton density is low, high matrix density prevents this region from initiating brittle failure, and 2) when local skeleton density is high, defects in the matrix are screened due to limited local stretch. We believe that the results of this easy-to-understand model demonstrate how DN structure can ignore defects that exist on the length-scale of the sacrificial network and will be important towards the implementation of future DN materials at all size-scales.

(a) Molecular DN hydrogel
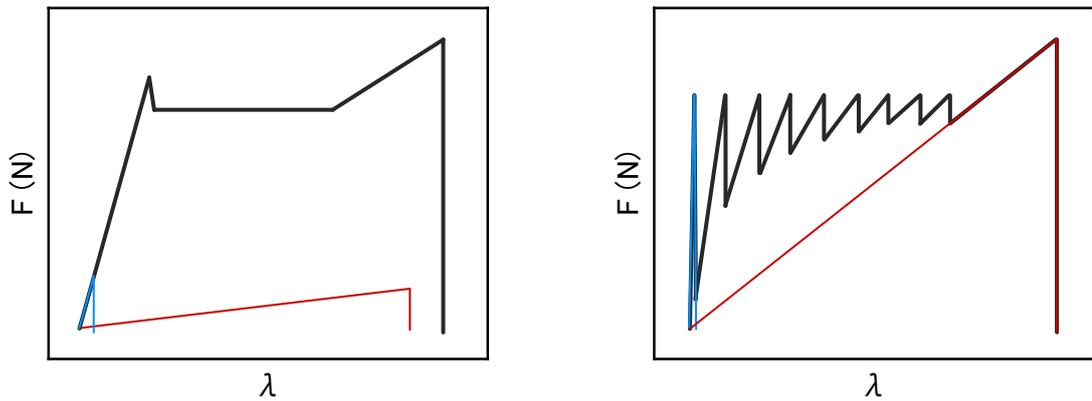
(b) Macroscopic DN composite

Figure 1. Exemplary images demonstrating the characteristic mechanical properties of DN materials. Force-stretch curves of the 1st network and skeleton (blue), the 2nd network and matrix (red), and their DN composites in (a) Molecular DN hydrogels and (b) Macro-DN materials.

4.2 Analytical model for macro-scale double-networks

Consider a macro-scale double-network (Macro-DN) formed by N sections connected in series. Each section contains two springs connected in parallel: One represents the skeleton as the 1st network, and the other represents the matrix as the 2nd network (**Figure 2a**). Here, the superscript indicates the section index ($1 \leq i \leq N$) and the subscript

represents the network type ($X = 1^{st}$ or 2nd). The displacement, δ, of each spring within a section must be equal:

$$\delta^{(i)} = \delta_1^{(i)} = \delta_2^{(i)} \tag{1}$$

The stiffness, k, in the ith section is equal to the sum of the stiffness of 1st network and 2nd network:

$$\kappa^{(i)} = \kappa_1^{(i)}\varphi_1^{(i)} + \kappa_2^{(i)}\varphi_2^{(i)} \tag{2}$$

where φ is the fracture factor, a binary term used to denote the existence of the network. If the displacement of a section exceeds the fracture displacement given to each spring, $\delta_{X,max}$, φ changes from 1 to 0:

$$\varphi_X^{(i)} = \begin{cases} 1 & \left(\delta^{(i)} \leq \delta_{X,max}^{(i)}\right) \\ 0 & \left(\delta^{(i)} > \delta_{X,max}^{(i)}\right) \end{cases} \tag{3}$$

The force, F, in the ith section is calculated by the product of (1) and (2):

$$F^{(i)} = \kappa^{(i)}\delta^{(i)} \tag{4}$$

Because the sections are loaded in series, the total force in each section must be equal:

$$F = F^{(1)} = F^{(2)} = \cdots = F^{(N)} \tag{5}$$

and the total displacement is equal to the sum of each section's displacement:

$$\delta = \sum_{i=1}^{N} \delta^{(i)} \tag{6}$$

Substituting (4) into (6), we can rewrite as:

$$\delta = F \sum_{i=1}^{N} \frac{1}{\kappa^{(i)}} \tag{7}$$

Rearranging (7), we can solve for F as a function of δ:

$$F = \frac{\delta}{\sum_{i=1}^{N}\frac{1}{\kappa^{(i)}}} \tag{8}$$

To accurately predict the force, the stiffness and fracture displacement of each component must be measured. We will ignore nonlinear effects and viscoelasticity, assuming the materials are perfectly elastic. Based on these experimental values and assumptions, the force versus displacement curve for each spring in each section can be calculated, as seen in **Figure 2b**. After obtaining these values, we can use Equation 8 to predict the expected fracture force of a Macro-DN composite.
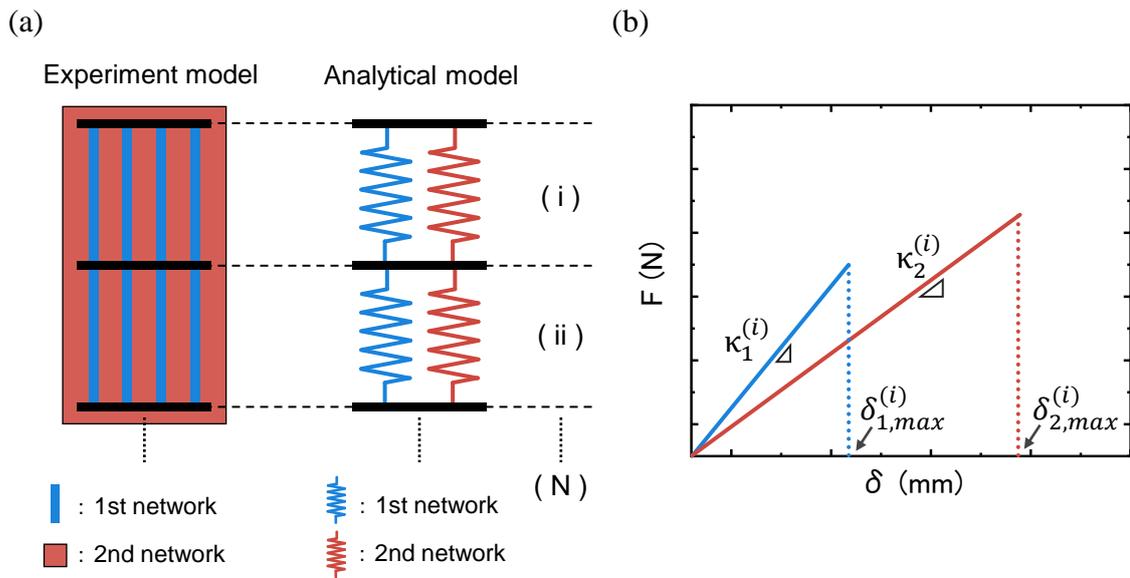
Figure 2. An analytical model to calculate force of a Macro-DN composite. (a) The Macro-DN model consists of a plastic skeleton acting as the 1st network (blue) and an elastomer matrix as the 2nd network (red). Each of these components can be modelled as an individual spring with independent properties. (b) Force-displacement curves of each spring in the ith section with κ and $\delta_{X,max}$ determined from experimental values.

4.3 Experiments

4.3.1 Materials

The skeleton and the matrix were made from plastic 3D printed material (AR-M2, Keyence Co) and silicone rubber (a commercially available two-part kit, KE-1603-A, and KE-1603-B, Shin-Etsu Chemical), respectively. See **Section 3.2.1** for details.

4.3.2 Skeleton fabrication

The grid-shaped plastic skeletons were designed by CAD software (Inventor, Autodesk Inc. and Shade 3D, Shade 3D Co., Ltd.) and 3D printed (AGILISTA-3000, Keyence). **Figure 3** contains a schematic illustration of the grid-shaped skeleton designed for use in **Section 4.4.1 and 4.4.3**. Full control over geometry is available, however parameters 1-3 and 5 from **Section 3.2.2** were not changed throughout this Chapter. Parameter 4 has been modified however, as shown below:

(4) All columns in the skeleton have a width of 0.6 mm, length of 0.769 mm, and thickness of 0.3 mm. The specific geometric parameters which were varied include the number of sacrificial bonds per section (from 2-6). The total number of sections was kept constant at 13.

For the homogeneous 1st network samples, the number of sacrificial bonds per section was kept constant at 4 bonds per section (**Figure 4a**). It is possible to modify the number of bonds per section, to create an inhomogeneous 1st network (**Figure 4b**).

After printing, the skeletons were washed in deionized water to remove the support material and dried prior to composite fabrication.
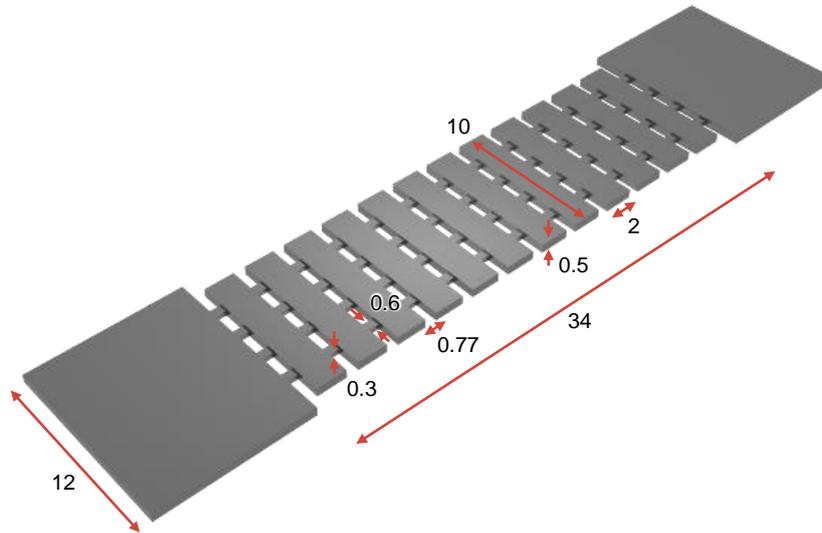
Figure 3. Dimensions of the 1ˢᵗ network used in Section 4.4.1 and 4.4.3. All dimensions are listed in mm.
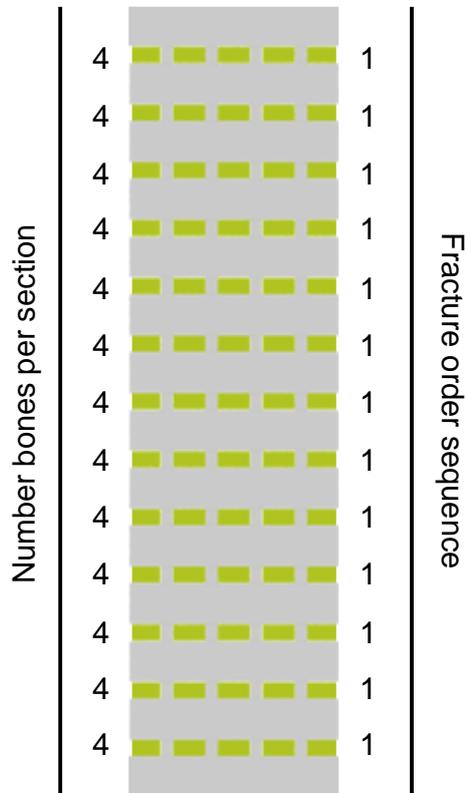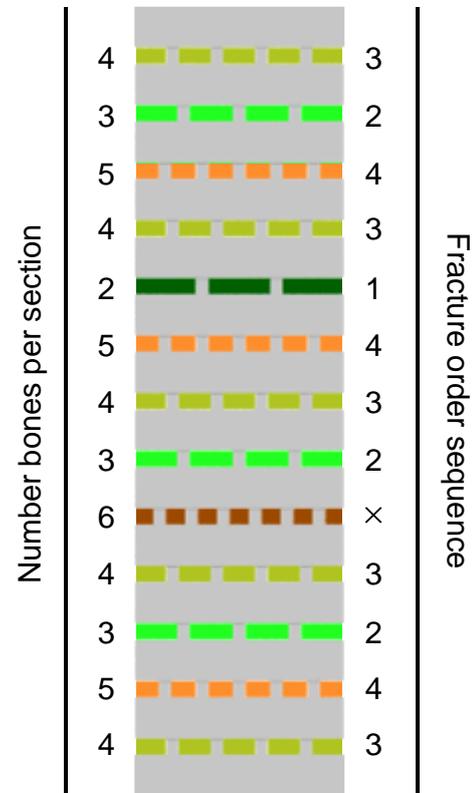
Figure 4. The geometric design of the 1st network. (a) Schematic of the homogeneous 1st network. (b) Schematic of the inhomogeneous 1st network.

4.3.3 Synthesis of Macro-DN composites and pristine matrices

See **Section 3.2.3** for details on how to fabricate the Macro-DN composite and pristine matrix. A schematic of the sample used in **Section 4.4.1** with dimensions can be seen in **Figure 5a**. Two cross-sectional images are shown corresponding with the colored planes in **Figure 5a**. **Figure 5b** is a cross-sectional image of the plane highlighted in red, containing sacrificial bonds. **Figure 5c** is a cross-sectional image of the plane highlighted green, containing the cross bar. The sample is embedded on all sides by silicone rubber. The dimensions listed represent the programmed values sent to the 3D printer. This results in a sample with 0.5 mm of rubber between the surface and the top of the cross bars, and

1 mm of rubber separating the side from the edge of the cross bars (**Figure 5b** and **Figure 5c**).

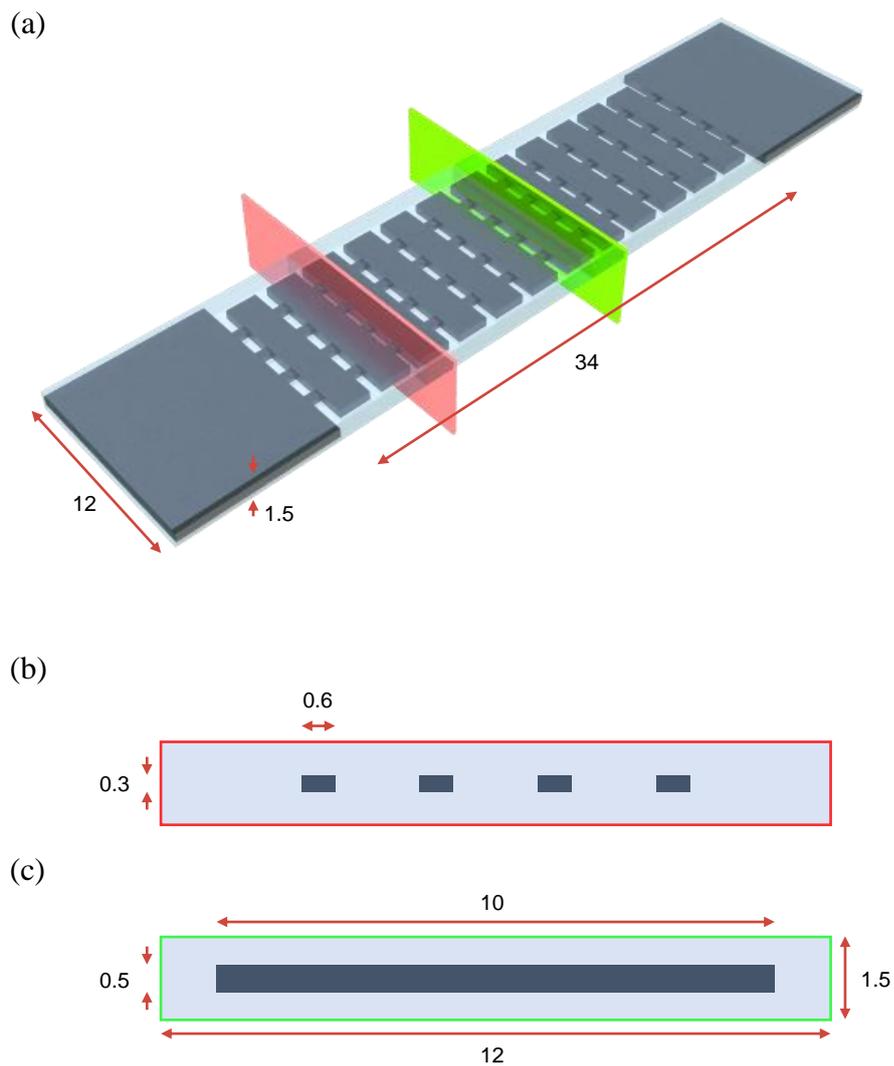**Figure 5. Schematics of the fabricated M-DN(1o,2o) composite. All dimensions are listed in mm.** (a) Schematic of the skeleton (1st network) embedded in elastomer (2nd network). (b) Cross-section of the red plane, containing the sacrificial bonds. (c) Cross-section of the green plane, containing the cross bar. The dark blue phase represents the 1st network while the light blue represents the 2nd network.

4.3.4 Tensile tests

See **Section 3.2.5** for details. Viscoelastic response of the 1st network was measured by uniaxial tensile test at different velocities. The skeleton was printed into the shape of a dog-bone (a width of 2 mm, a length of 12 mm, and a thickness of 1 mm). Each sample was stretched at 1 mm/min, 10 mm/min, and 100 mm/min.

4.3.5 Pre-notch tests

Utilizing a pre-notch as a method to incorporate defects in the 2nd network make these models match the geometry of a single-notch fracture toughness experiment. From the following equation,[67] we can measure the fracture toughness (Γ) of the composite, depending on pre-notch location:

$$\Gamma = \frac{6U(\lambda_c)c}{\sqrt{\lambda_c}}$$

Where U is the deformation energy of a pristine sample, c is the pre-notch length, and l_c is the stretch at which the pre-notch starts to grow. By determining the energy required to deform the pristine sample up to the stretch where the crack was determined to begin growing (l_c), we can calculate the fracture toughness.

4.4 Results

4.4.1 Homogeneous 1st network with pristine 2nd network ("perfect" double-network)

Double-networks on the molecular-scale possess a rigid sacrificial 1st network embedded within a stretchable 2nd network. We can easily match the essence of this design on the macro-scale by utilizing a stiff and brittle thermoset with a low modulus elastomer. In **Chapter 3**, we investigated the design parameters that control the DN principle by modifying the structural design of the skeleton as the 1st network by using 3D printing.[69] The skeleton was designed in a grid-lattice shape made up of numerous sections,

delineating by horizontal crossbars (see **Section 3.2.2** and **Section 4.2.2** for the geometric design of the skeleton). These stiff crossbars never fracture and prevent the rigid interconnects (sacrificial bonds) from fracturing in multiple sections simultaneously. This rigid crossbar design is very useful for investigating how each component interacts within a section, and the role of load transfer between sections during deformation, and will therefore be employed here.

The samples were fabricated through the same process as introduced previously. In brief, a skeleton containing 13 sections of equal length was 3D printed, surrounded by a spacer. Each section contained sacrificial bonds that could be varied in number. Commercially available silicone rubber precursor solution was mixed and degassed, then poured into the mold containing the 3D printed skeleton. Excess silicone rubber prepolymer was removed from the top of the spacer, and the composite was allowed to cure at room temperature for 48 hours. After this time, the composite was removed from the mold by using a laser cutter to cut to the desired shape. The composites were then tested directly by uniaxial tensile testing at a stretching velocity of 50 mm/min. The fabricated samples are coded as M-DN(1a,2b), where *a* and *b* denote whether the component is pristine (o) or contains a defect (x).

As a control case, we first show a Macro-DN composite containing a homogenous skeleton, meaning each section contains the same number of sacrificial bonds (four), totaling 52 sacrificial bonds. This sample can be considered a "perfect" double-network: on the length-scale of the sacrificial bonds (mm scale) no defects exist in either network. This sample is coded as M-DN(1o,2o). This sample was tested by uniaxial tensile testing (**Figure 6a**), and images were taken during the deformation process (**Figure 6b**). The undeformed sample cam be seen in **Figure 6bi**. The sacrificial bonds within a deforming section all broke simultaneously, and stepwise, section-by-section fracture occurred. This

section is denoted by a yellow arrow in the images of **Figure 6b**. After initial rupture of the skeleton, the load transferred to the 2nd network within that section (**Figure 6bii**). After the local 2nd network stretched and stiffened another section ruptured (**Figure 6biii**). This cycle continued until all of the sacrificial bonds were extinguished (**Figure 6biv-vi**). Finally, the 2nd network stretched and hardened (**Figure 6bvii**) and the Macro-DN composite fractured.

The fracture process of the Macro-DN composite without defects can be easily described by the simple analytical model introduced in **Section 4.2**. The results of the model are shown in **Figure 6c**. Note that the model assumes that the components are completely linearly elastic, while the real matrix exhibits mild strain softening followed by strain hardening behavior. By comparison with the experimental results in **Figure 6a**, we see that the model can strongly predict a few important points. First, the average force during yielding is well predicted, within 20%. Interestingly, the experimental results show a slight decrease in the force of internal rupture after the first event, whereas the model expects a slight but gradual increase in force. This is likely due to the slightly viscoelastic response of the 1st network (**Figure 7**), since the initial fracture event is strain controlled at high velocity, and subsequent fracture events are force controlled (resulting in a much lower effective stretching velocity). The distance between peaks is accurately predicted, along with the length of the yielding region. We also see that the minimum force between fracture events increases gradually, and again the force is predicted to be higher by the model. This is likely due to the model not taking into account the strain softening exhibited by the elastomer. Notably, we are unable to explicitly determine the *order* in which the sections will fracture for the M-DN(1o,2o) sample, because each section contains bonds that are fabricated to identical specifications, and therefore should also have identical stiffnesses. The fracture order is governed by microscopic defects in the

fabrication process or local stress concentrations, effectively causing the multi-step internal fracture process to occur at random (**Figure 6bii-vi**).

(a) Experiment results
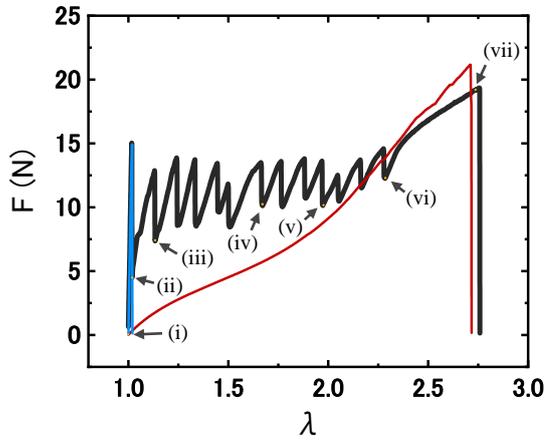
(c) Theoretical results

(b) Fracture behavior

12 mm
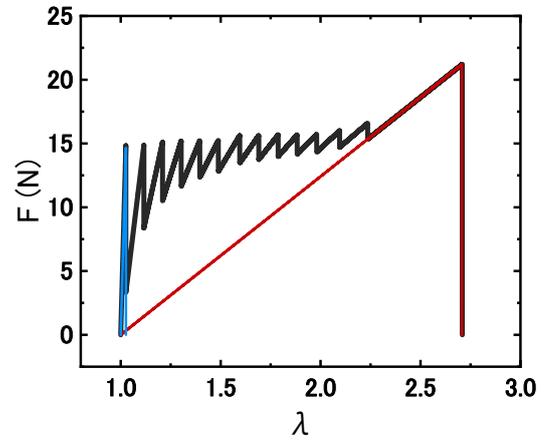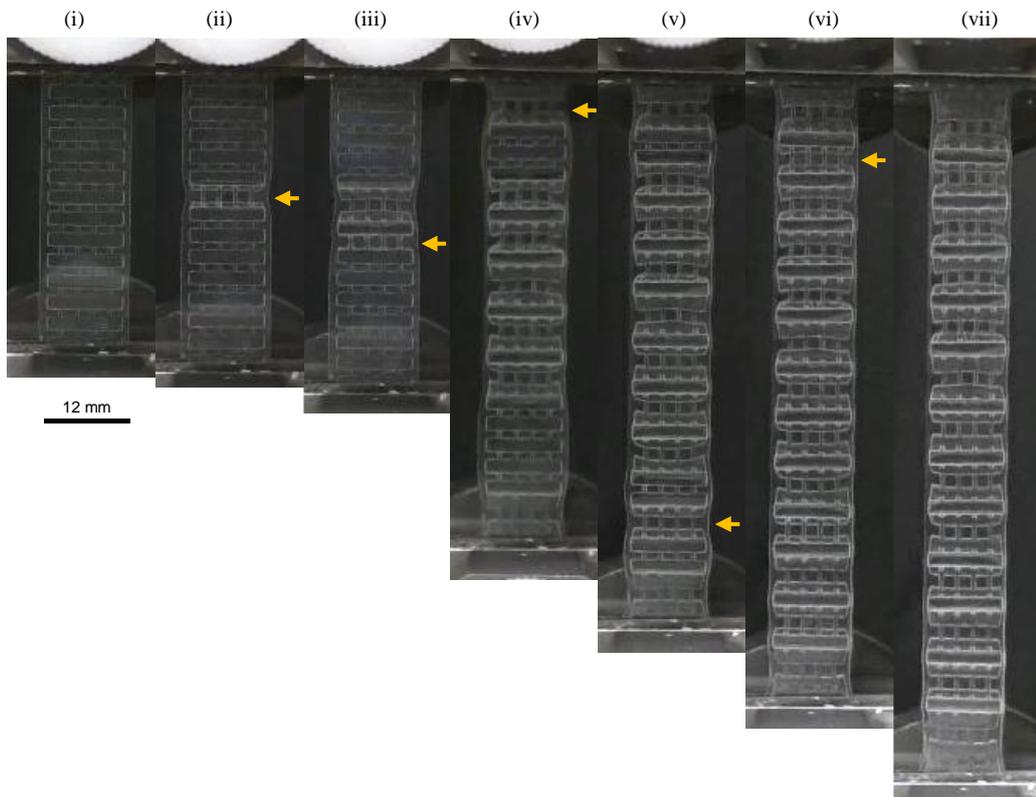
Figure 6. Uniaxial tensile behavior and internal fracture of the "perfect" Macro-DN composite (M-DN(1o,2o)). (a) Experimental curves of the 1st network without defect (blue), the 2nd network without defect (red), and their composite (black). (b) Fracture behavior of the Macro-DN composite. Images correspond to the labels in (a). (c) Predicted fracture curves based on the analytical model.
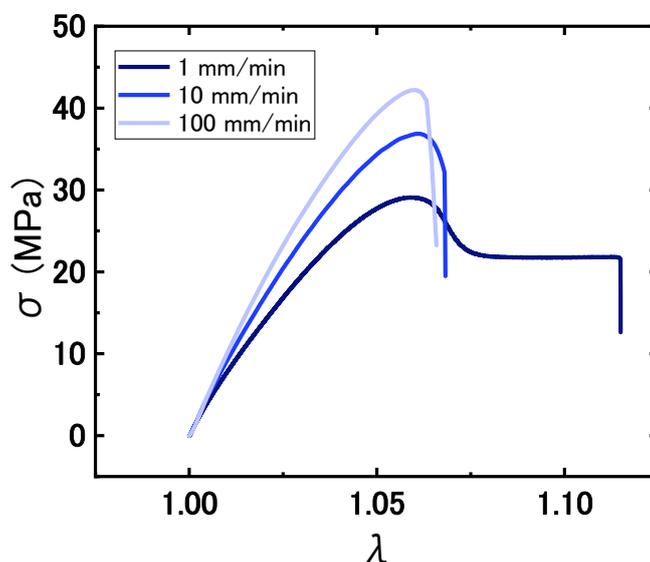
Figure 7. The stress-stretch curves of the 1st network (3D printed skeleton) at different velocities. Stress versus stretch ratio curves of the 1st network at 1 mm/min (light blue), 10 mm/min (blue), and 100 mm/min (dark blue).

4.4.2 Inhomogeneous 1st network with pristine 2nd network (1st network defect)

Next, we investigated the effect of inhomogeneity in the 1st network on the mechanical properties of the Macro-DN composite. To generate a model of an inhomogeneous 1st network, we kept constant the basic geometry of the 1st network, the number of sections, and the total number of sacrificial bonds (see **Section 4.3.2** for details on introducing defects into the 1st network) but changed the number of sacrificial bonds within a given section (**Table 1**). These samples are coded as M-DN(1x,2o). The polymer network structure of hydrogels is known to be highly inhomogeneous, causing brittleness.[70,71] One reason for this is that the reaction rate between monomer and crosslinker can vary, and not all reactive groups in multifunctional monomers are equally reactive. Some specific methods, including Tetra-PEG hydrogels,[72] slide ring hydrogels,[51,52,73] and highly entangled hydrogels[74] have been developed to overcome these issues, but most hydrogels are still synthesized by traditional means. In our model system, since all sacrificial bonds

are of equivalent stiffness, a section with less bonds will fracture at a lower force. Therefore, if only two or three sacrificial bonds exist within a section, that section will fracture with less force than the fracture force of the homogenous 1st network introduced in **Section 4.4.1**. Since we know the force required to break one sacrificial bond, we can predict that sections containing five sacrificial bonds or less will have a fracture force less than the force of the pristine matrix, meaning they should be capable of fracturing sacrificially. The fracture force for a section containing six sacrificial bonds is larger than that of the 2nd network (neat silicone rubber) and therefore will not fracture (**Table 2**). When testing the inhomogeneous 1st network independently, fracture always occurs first in the region containing the least sacrificial bonds (in this case, the two-bond section, **Figure 4b**). This is reasonable, because the skeleton can be modelled as multiple elastic springs in series (see **Section 4.2**), and therefore each section experiences equivalent force. Since the section with the lowest number of bonds has the lowest fracture strength, it will fracture first. Based on this reasoning, we can now predict the section fracture order for the M-DN(1x,2o) composites.

   Figure 8a shows the tensile results of the M-DN(1x,2o) composite (shown before deformation in **Figure 8bi**). In this case, the section containing two sacrificial bonds (denoted by a blue arrow) always ruptured first (**Figure 8bii**). The fracture process then continued, with the sections containing three sacrificial bonds (**Figure 8biii**), four bonds (**Figure 8biv, v**), and five bonds (**Figure 8bvi**) rupturing sequentially. As predicted the six-bond section did not fracture. After the sections containing five or less sacrificial bonds ruptured, the 2nd network hardened and fracture of the composite occurred (**Figure 8bvii**). The Macro-DN composite exhibits a different fracture force during the internal multi-step fracture process depending on the fracture force of each section. Even when the 1st network fractures at relatively low force, the 2nd network can locally harden,

increasing the force to a level that the sample can fracture elsewhere. The ultimate fracture force of the composite is the same, regardless of whether a homogeneous ("perfect") or inhomogeneous ("defect-containing") 1st network exists. Furthermore, when compared to the perfect Macro-DN composite (**Figure 6a**), the minimum force in the yielding region is smaller (M-DN(1x,2o): 8.81 ± 0.22 N, M-DN(1o,2o): 13.66 ± 0.70 N) because the inhomogeneous 1st network contains weaker sections representative of defects. The average yield force is nearly the same (M-DN(1x,2o): 12.81 ± 1.55 N, M-DN(1o,2o): 13.66 ± 0.70 N), but the maximum force in the yielding region is higher (M-DN(1x,2o): 16.72 ± 0.94 N, M-DN(1o,2o): 13.66 ± 0.70 N). The fracture stretch ratio decreased slightly (M-DN(1x,2o): 2.61 ± 0.11, M-DN(1o,2o): 2.79 ± 0.02), because one section could not rupture, but this decrease was small and was also captured by our model.

The results from the model system (**Figure 8c**) match the experimental results, showing that the sections that fracture occur sequentially with increasing section number, and the rupture force matches the fracture force of the breaking section. As expected, the 2nd network does not possess sufficient strength to break the section containing six sacrificial bonds. This confirms our hypothesis about how fracture occurs in networks containing inhomogeneous 1st networks. When the 2nd network is pristine, inhomogeneity of the 1st network does not significantly influence the mechanical properties of a macroscale double-network.

Table 1. Skeleton structure with and without defects.

Skeleton structure		Number of bonds per section					
		2	**3**	**4**	**5**	**6**	**Total**
homogeneous	Number sections	0	0	13	0	0	13
(perfect)	Total bonds	0	0	52	0	0	52
inhomogeneous	Number sections	1	3	5	3	1	13
(defect)	Total bonds	2	9	20	15	6	52
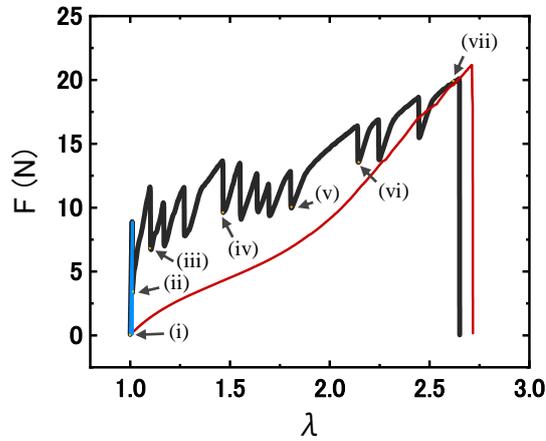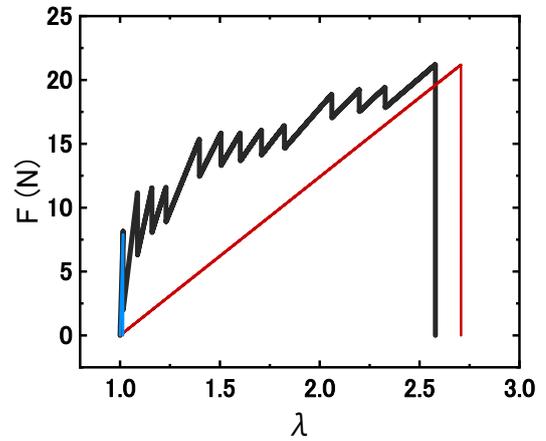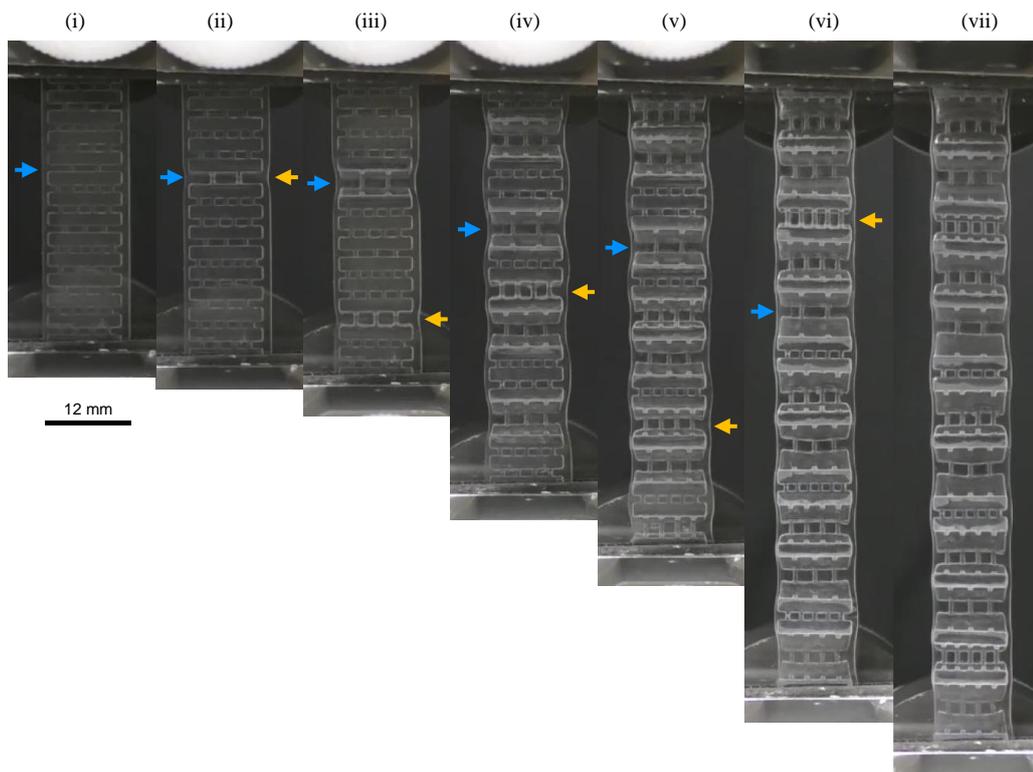
Figure 8. Uniaxial tensile behavior and internal fracture of the Macro-DN composite with 1st network defect (M-DN(1x,2o)). (a) Experimental curves of the inhomogeneous 1st network (blue), the 2nd network without defect (red), and their composite (black). (b) Fracture behavior of the Macro-DN composite. Images correspond to the labels in (a). The blue arrow denotes the location of the largest 1st network defect, and the yellow arrow denotes the section that has ruptured. (c) Predicted fracture curves based on the analytical model.

Table 2. Number of sacrificial bonds per section and fracture force of the 1st network.

Number bonds per section	Section	Input Width, (mm)	Input Thickness, (mm)	Input Cross-sectional Area, (mm²)
2	13	0.6	0.3	0.36
3	13	0.6	0.3	0.54
4	13	0.6	0.3	0.72
5	13	0.6	0.3	0.90
6	13	0.6	0.3	1.08

Number bonds per section	Stiffness, (kN/m)	Fracture Stretch	Fracture Force, (N)	Work of Fracture, (mJ)
2	14.92 ± 0.86	1.012 ± 0.002	8.15 ± 0.01	1.99 ± 0.01
3	19.91 ± 1.93	1.013 ± 0.002	10.59 ± 0.48	2.33 ± 0.44
4	24.75 ± 1.36	1.015 ± 0.002	14.28 ± 0.66	4.81 ± 0.77
5	29.59 ± 2.09	1.016 ± 0.001	17.91 ± 0.57	5.31 ± 0.58
6	33.51 ± 1.84	1.019 ± 0.001	21.66 ± 0.67	7.44 ± 0.50

4.4.3 Homogeneous 1st network with 2nd network pre-notch (2nd network defect)

Next, we incorporated defects into the 2nd network, in combination with a homogenous 1st network. As a simple method to demonstrate a 2nd network defect, we used a laser-cutter to make a notch of 1 mm in length. The pre-notch was always located at the edge of the sample, only cutting the matrix, leaving the 1st network fully intact. When testing the matrix independently, fracture always initiates from the pre-notch, causing fracture to occur at lower stretch, and the force at fracture to decrease. Based on this understanding, we expect that fracture of Macro-DN composites should also initiate from the pre-notch. However, for the pre-notch to initiate fracture, it must undergo deformation, and as we have shown in the previous sections, local deformation only occurs after rupture of the local 1st network. Therefore, 1st network rupture ordering governs fracture, yet for a homogenous 1st network, the fracture order is random.

The M-DN(1o,2x) composites are composed of 13 sections, and since any section can rupture at random there is a 7.7% chance that the section containing the 2nd network defect will rupture at any time. Until the 1st network ruptures in the section containing the 2nd network defect, the defect does not influence the mechanical properties of the composite. However, once the section with the 2nd network defect ruptures, the local 2nd network begins to deform and fractures rapidly. In the case where fracture of the skeleton region containing the defect happens last, we would expect the mechanical properties to be similar to the perfect Macro-DN.

The tensile results of all M-DN(1o,2x) composites can be seen in **Figure 9.** The mechanical response nearly matches that of the M-DN(1o,2o) composite until rupture of the 1st network occurs in the section containing the 2nd network defect, which initiated complete sample fracture. Assuming the probability of each section rupturing is equal (7.7%), and the sample contains a total of 13 sections, we expect fracture will most likely

occur after seven sections have ruptured. If fracture of the last sacrificial bonds in a perfect Macro-DN occurs at a stretch ≈ 2.4, then on average, we would expect fracture of the M-DN(1o,2x) composite to occur at a stretch ~1.7 (50% of the maximum stretch). This result corresponds with the middle two samples (light purple and purple lines) of **Figure 9**, that fracture at stretches of 1.62 and 1.90. However, there is wide variability, and some composites can fracture at very low stretch (magenta line). **Figure 10a** shows the force versus stretch curve of the M-DN(1o,2x) composite that fractured at the highest stretch. **Figure 10b** contains images corresponding with the labels in **Figure 10a**. The red arrow denotes the location of the notch. As stretching occurs, the rupture events that take place in the 1st network are not influenced by the notch, occurring randomly. In **Figure 10biv-vi** we see that rupture occurs near the section containing the notch, but the section containing the notch remains shielded. In **Figure 10bvii**, rupture in the notch region occurs followed by immediate sample fracture. For this sample, 11 rupture events occurred prior to fracture. In our theoretical calculations, we can match these results by inputting small "defects" into the 1st network, so that there are slight differences in stiffnesses in different sections to match the experimental fracture order. The expected fracture curve of the sample in **Figure 10a** is shown in **Figure 10c**. We see good agreement between the theoretical and experimental results.

By comparing the results of the M-DN(1o,2o) sample with the M-DN(1o,2x) sample we see that stretching of the matrix after all sections ruptured accounts for a stretch of about 0.47. Due to the defect present in the M-DN(1o,2x) sample that fractures at high stretch, the fracture stretch decreased by this amount, compared to the M-DN(1o,2o) sample. This also resulted in a slight decrease in the fracture force. However, since the yield force is governed by the stiffness of the 1st network, these composites possess the

same yield force and dissipated 61% of the energy of the perfect Macro-DN composite (764 mJ for M-DN(1o,2o) versus 467 mJ for M-DN(1o,2x)).

From the above, it was found defects in the 2nd network can significantly influence the mechanical properties of the Macro-DN composites. Specifically, the fracture stretch ratio can vary greatly, directly impacting work to fracture. If we were to modify the 1st network to increase the number of sections, the number of fracture events that will occur prior to fracture should increase, as the probability that any individually ruptured section contains a defect decreases. This should cause the average work of fracture to increase.
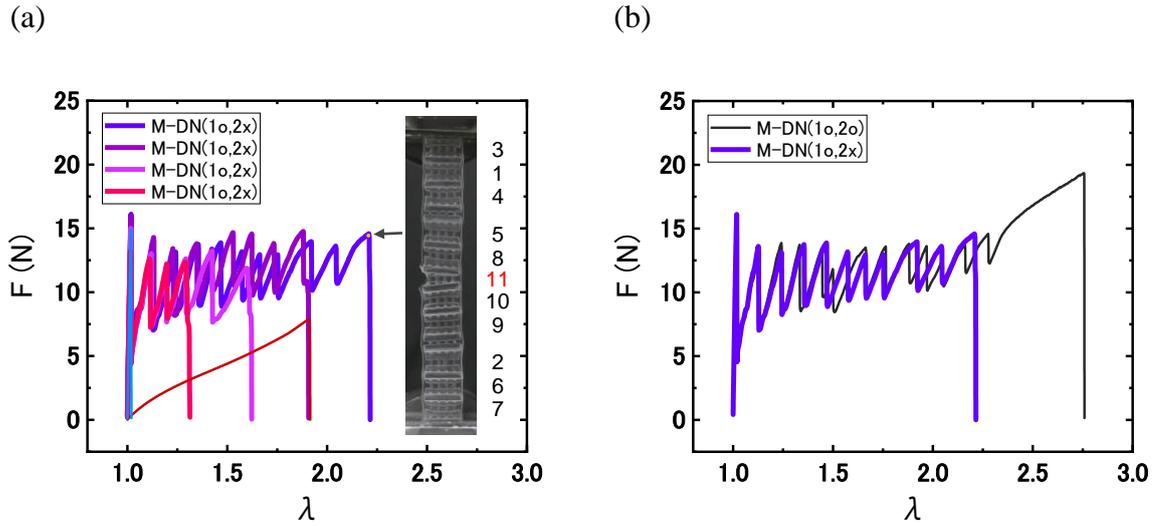
Figure 9. Uniaxial tensile behavior and internal fracture of the Macro-DN composite with 2nd network defect (M-DN(1o,2x)). (a) Experimental force-stretch curves of the 1st network without defect (blue), the 2nd network with defect (red), and their composites (magenta, light purple, purple and blue-purple). The inset photograph is of the Macro-DN composite (blue-purple) showing the random order in which the 1st network ruptured. (b) Force-stretch curves comparing the experimental results of the M-DN(1o,2o) and the M-DN(1o,2x) sample that failed after 11 fracture events.

(a) Experiment results
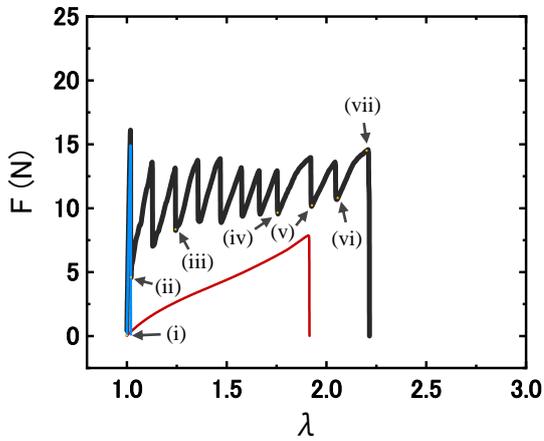
(c) Theoretical results
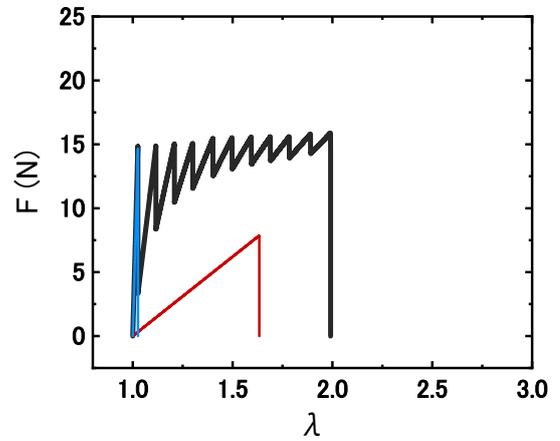
(b) Fracture behavior
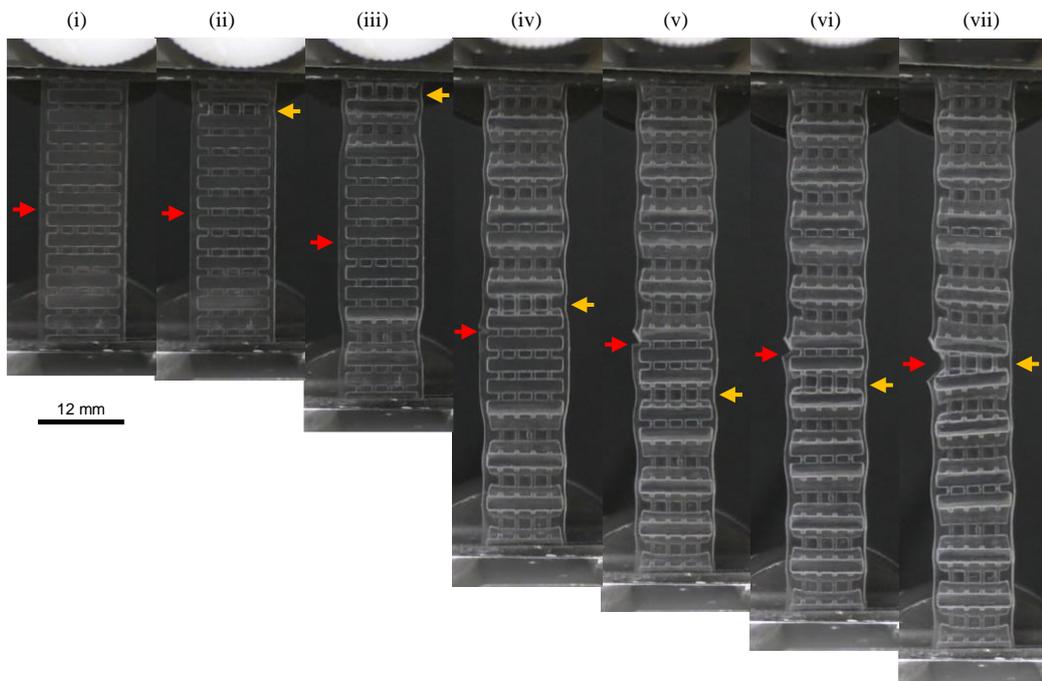
Figure 10. Uniaxial tensile behavior and internal fracture of the Macro-DN composite with 1st network defect (M-DN(1o,2x)). (a) Experimental curves of the homogeneous 1st network (blue), the 2nd network with defect (red), and their composite (black). (b) Fracture behavior of the Macro-DN composite. Images correspond to the labels in (a). The red arrow denotes the location of the 2nd network defect, and the yellow arrow denotes the section that has ruptured. (c) Predicted fracture curves based on the analytical model.

4.4.4 Inhomogeneous 1st network with pre-notched 2nd network ("real" double-network)

Finally, we investigated the effect of introducing defects into both the 1st and 2nd networks of the Macro-DN composites (M-DN(1x,2x)). We consider that this composite type represents the simplest model of real DN hydrogels, which due to their uncontrolled free-radical polymerization process, contain many defects. These samples were prepared by combining, the 1st network and 2nd network designs with defects as introduced in **Section 4.4.2** and **Section 4.4.3**, respectively. The mechanical properties of the composite were varied widely depending on the positional relationship between the defects of the 1st and 2nd network. These samples are classified according to the section (z) in which the 2nd network defect was introduced (M-DN(1x,2x-z)). For example, when the 2nd network defect existed in the section containing two sacrificial bonds, it is referred to as M-DN(1x2x-2).

The fracture behavior of the M-DN(1x,2x) composites during tensile testing could be classified into two cases. The first fracture case occurs when the 2nd network defect is introduced into a section containing a relatively weak part of the 1st network, M-DN(1x,2x-2), M-DN(1x,2x-3), or M-DN(1x,2x-4)) (**Figure 11a**). In this case, the weak part of the 1st network ruptured at low stretch, quickly deforming the region of 2nd network containing the defect, causing fracture at low stretch. In the experimental model, these samples showed almost the same mechanical properties. However, according to the theoretical model, the mechanical properties are expected to improve as the location of the defect in the 2nd network occurs in increasingly stronger locations (M-DN(1x,2x-4) > M-DN(1x,2x-3) > M-DN(1x,2x-2)). In the theoretical model, the composite fractured as soon as the section with the 2nd network defect ruptured (**Figure 11b**). However, the 2nd network matrix that is being used here has some ability to blunt cracks by its own

dissipation mechanisms, and therefore even the 2nd network region containing a crack could often support enough load to break additional weak sections containing two or three sacrificial bonds. However, once the weakest remaining 1st network section contains at least four sacrificial bonds, the sample will fail, as seen in **Section 4.4.3**.

When the 2nd network defect is introduced into a section with a "strong" 1st network (M-DN(1x,2x-5) or M-DN(1x,2x-6)), we observe a different fracture process (**Figure 11c**). In this case, fracture of the Macro-DN composite was significantly delayed. These results are in good agreement with the theoretical results (**Figure 11d**). As seen in the M-DN(1x,2x-5) specimen, the 1st network with 2nd network defect did not fracture unless the composite was highly stretched, so even if there is a defect in the 2nd network, the composite exhibits high stretchability. Furthermore, for the M-DN(1x,2x-6) specimen, sufficient force cannot be generated by the 2nd network to deform the 1st network section containing the 2nd network defect, and in this case, the 2nd network defect is completely ignored. Images of the fracture process can be seen in **Figure 11e**. The blue arrow and red arrow denote the locations of 1st and 2nd network defects, respectively. Initial rupture events (yellow arrows) occur in order of increasing 1st network stiffness, initiating with the 1st network defect and then ignoring the 2nd network defect. During composite fracture, a completely different part of the composite initiates failure, separate from the region containing the defective 2nd network. From the force-stretch ratio curves, the M-DN(1x,2x-5) and M-DN(1x,2x-6) composites exhibit high yield force, fracture force and fracture stretch, even though both component materials are imperfect.

From the observed fracture process of Macro-DN composites containing defects in both networks, we see that when the relatively strong part of the 1st network has a 2nd network defect, the 2nd network defect is protected from deformation by the strong sacrificial bonds of the 1st network, resulting in a fracture process that appears as is no

81

defects exist. Based on this result we consider that the defect containing Macro-DN composites could achieve nearly the maximum potential of the component materials because the Macro-DN composites reinforcing behavior is capable of overcoming the defects. When compared to the perfect Macro-DN (M-DN(1o,2o), the M-DN(1x,2x-5) and M-DN(1x,2x-6) composites exhibit nearly the same work of fracture (**Figure 12**). The work to fracture even exceeds both the M-DN(1o,2x) and M-DN(1x,2o) composites, despite containing more defects. Due to the similarity of geometry, we can also analyze the fracture toughness of these materials, and the results are in strong accordance with the work to fracture (**Section 4.3.5, Figure 13**). These results suggest that even if there are defects in the component materials, Macro-DN composites possess an inherent ability to ignore these defects and exhibit the excellent potential mechanical properties of the neat components.

(a) Experiment results
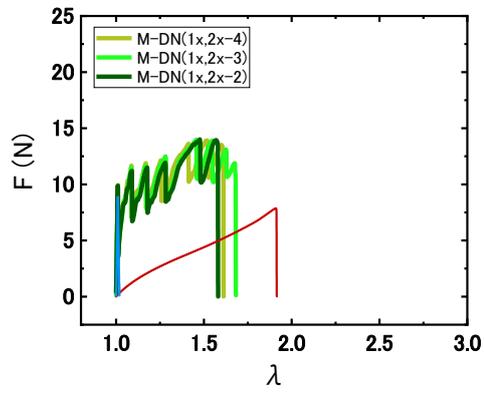
(b) Theoretical results
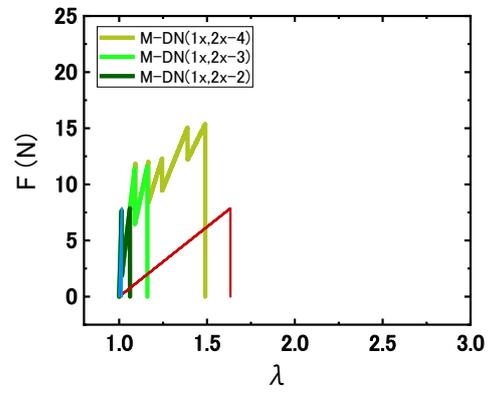
(c) Experiment results
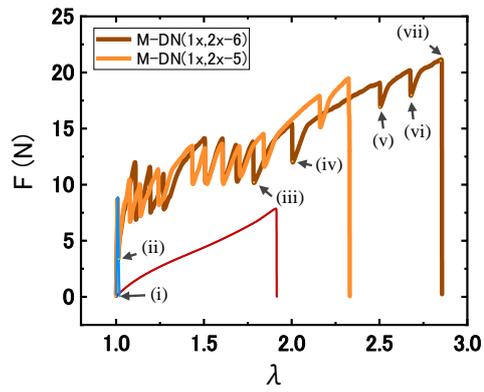
(d) Theoretical results
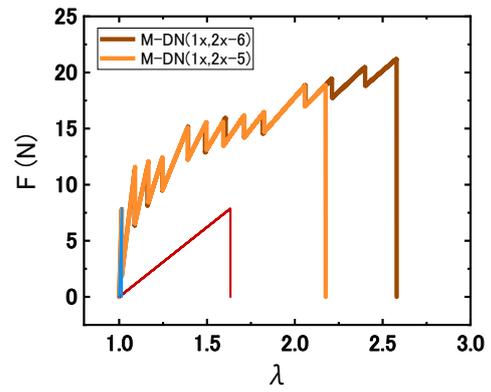
(e) Fracture behavior
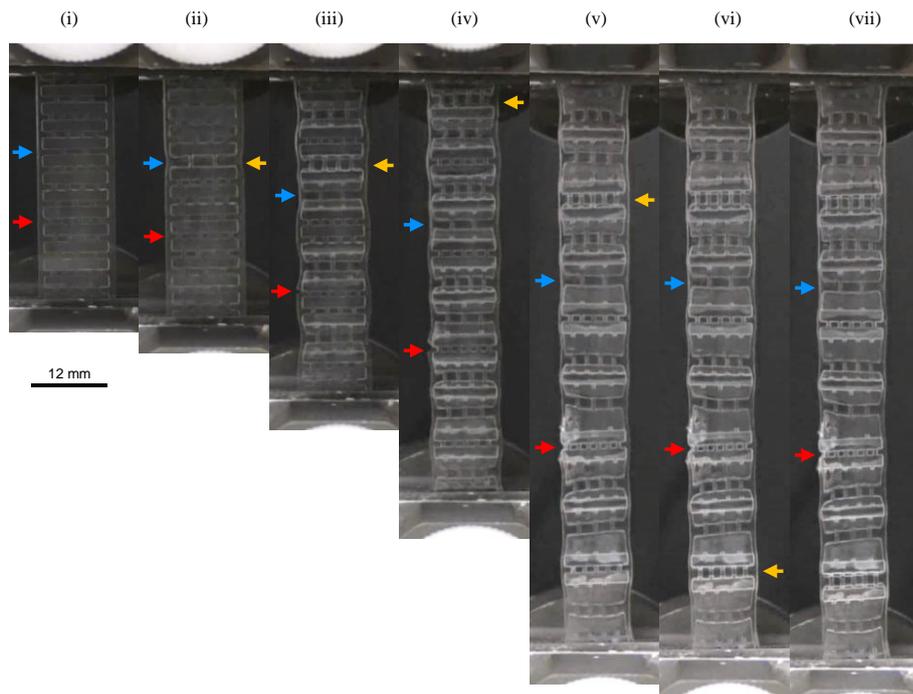
Figure 11. Uniaxial tensile behavior and internal fracture of the "real" Macro-DN composite with defects in both networks (M-DN(1x,2x)). (a) Experimental and (b) theoretical force-stretch curves of the 1st network with defect (blue), the 2nd network with defect (red), and their composites, when the defect is located in sections with 2-4 sacrificial bonds. (c) Experimental and (d) theoretical force-stretch curves of the 1st network with defect (blue), the 2nd network with defect (red), and their composites, when the defect is located in sections with 5 or 6 sacrificial bonds. (e) Fracture behavior of M-DN(1x,2x-6). Images correspond to the labels in (c). The blue arrow denotes the location of the largest 1st network defect, the red arrow denotes the location of the 2nd network defect, and the yellow arrow denotes the section that has ruptured.
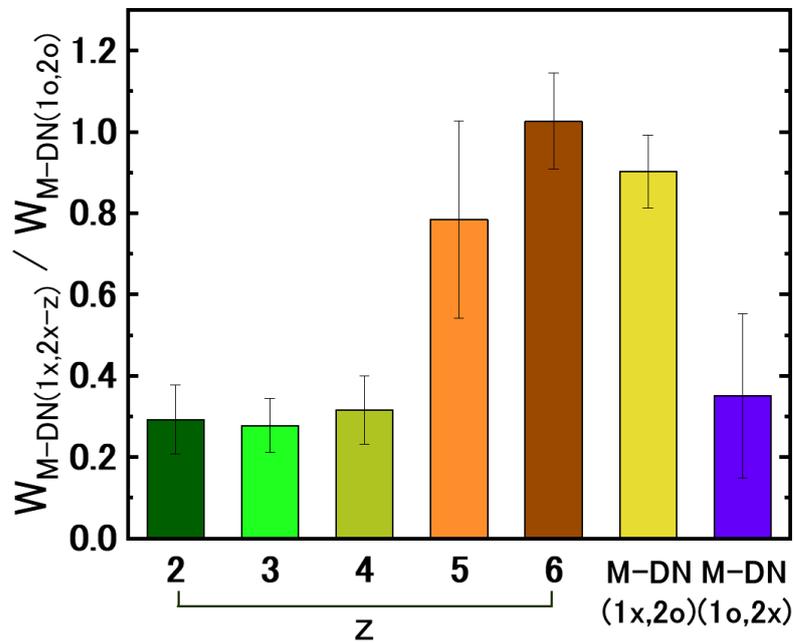
Figure 12. Work of fracture ratio of the "real" Macro-DN composites (M-DN(1x,2x-z) compared to the "perfect" Macro-DN composite (M-DN(1o,2o), based on location of the 2nd network defect, z. The Macro-DN composite with pristine 2nd network (M-DN(1x,2o)) and homogeneous 1st network (M-DN(1o,2x) are included for comparison.
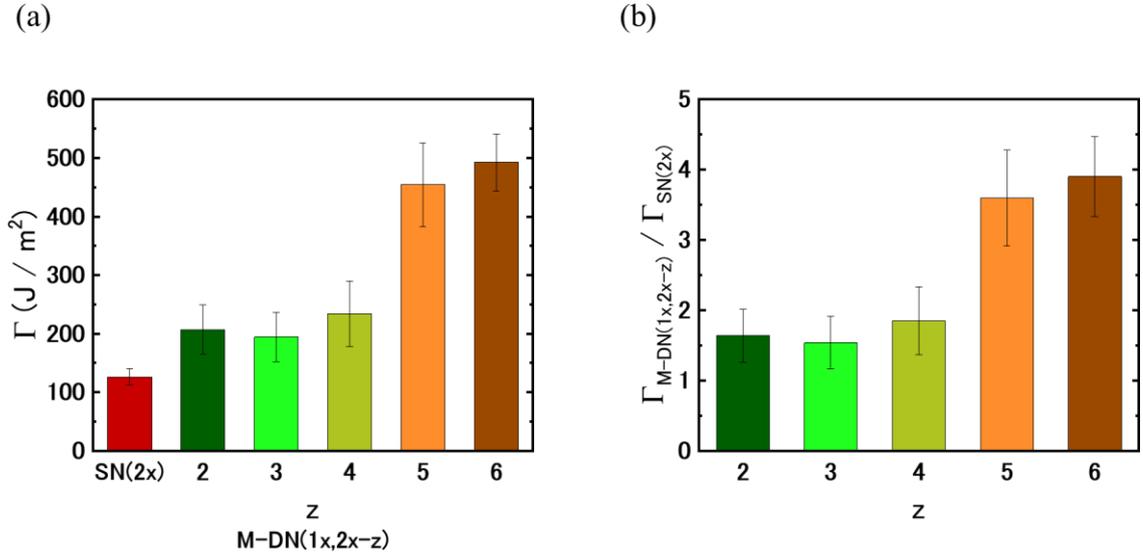
Figure 13. Comparing the mechanical properties of "real" Macro-DN composites to a single network material. (a) Fracture toughness, and (b) fracture toughness ratio as a function of defect location. Fracture toughness of SN(2x) is included independently for comparison in (a).

4.5 Discussion

Here we have introduced "defects" into the 1st and 2nd network of our Macro-DN composites to demonstrate how double-networks can achieve defect-tolerance when composed of inherently defect-prone materials. By introducing inhomogeneity into the macroscale 1st network, we observe a difference between the fracture strength of the neat inhomogeneous 1st network and the yield force of the Macro-DN composite. Rupture of the first section of the macroscale 1st network that has the least number of sacrificial bonds occurs at low force, but because the macroscale 2nd network can stiffen and support load in that region, other stronger areas can fracture. Thus, the yield stress of the Macro-DN composite is much greater than the fracture force of the 1st network. The inhomogeneity of the molecular 1st network causes it to be extremely brittle, resulting in the significant difference in mechanical performance when compared to a molecular double-network. The molecular 2nd network can deform to relatively large stretch but breaks before it can achieve high stress. When a pre-notch is added to the macroscale 2nd network, it likewise

can become very sensitive to deformation. If the 1st network is inhomogeneous, the location of the notch in the Macro-DN composite becomes extremely important. If the 2nd network defect exists in a region of high stiffness of the 1st network, significant deformation of the notch will not occur, and there is no impact on the mechanical response due to its presence.

The Macro-DN composites introduced here possess a synergistic increase in mechanical properties similar to what we see in molecular double-networks: the strength, fracture stretch, and work of fracture all greatly exceed the neat components. To illustrate this fact, we compared these properties for these four architectures introduced here (M-DN(1o,2o), M-DN (1x,2o), M-DN (1o,2x) and M-DN (1x,2x-6)) to the defect-containing "real" 2nd network (SN(2x)) in **Figure 14a-c**. Representative force versus stretch curves for each of these Macro-DN composites compared to the "real" 2nd network can be seen in **Figure 15**. Regarding the fracture force (**Figure 14a**), all samples, regardless of the presence of defects, can exceed the maximum force of the 2nd network. Specifically, when the defect exists in the 2nd network with a homogeneous 1st network (M-DN(1o,2x), we see the smallest improvement, only slightly higher than the independent matrix, because this defect prevents hardening from occurring that is seen at high stretch. Even though initial internal rupture occurs at low force in the M-DN(1x,2o) system, the strength of the 2nd network allows for high force to be achieved. Similarly with M-DN(1x,2x-6) the 1st network defect can be overcome, and the 2nd network defect is ignored, resulting in similar fracture force increases when compared to the "perfect" Macro-DN composite (~2.5x compared to the matrix). The same trends that are seen in fracture force are observed in fracture stretch (**Figure 14b**). Defects in the 2nd network of the M-DN(1o,2x) composite causes a wide dispersity of fracture stretches, as can be seen from the large

error bars. The "real" Macro-DN (M-DN(1x,2x-6) composite can reach a fracture stretch of ~1.4x compared to the matrix even though it also contains 2nd network defects, because these defects are shielded by the strong regions of the inhomogeneous 1st network. In this case the fracture stretch is equivalent to that of the "perfect" Macro-DN. Based on these results, it is clear that to realize greatly improved mechanical properties, controlling the influence of defects, which are always present, is essential. We consider that since DN hydrogels are formed through a two-step process, the synthesis of the 2nd network may occur differently in a DN hydrogel than it would if synthesized independently. The 1st network is synthesized first and forms an inhomogeneous network structure due to the free-radical polymerization method. This means that there is a large distribution of polymer strand lengths between crosslinks, and different regions will be capable of swelling to different degrees: high density 1st network regions will take up relatively less 2nd network monomer, and low density 1st network regions will take up more 2nd network monomer. After 2nd network synthesis, we therefore expect there to be two types of regions based on this swelling effect. During stretching, the low density 1st network regions should rupture first, and the high density of 2nd network chains can support the load locally. As stretching continues, regions of higher density will continue to fracture sequentially. This process can be visualized as the formation of a neck in a tensile sample that grows with increasing stretch. Regions that consist of 2nd network defects, due to low chain density, are most likely to exist in regions with high 1st network density, and therefore will undergo deformation last, screening the 2nd network defects. Therefore, we hypothesize that the synthesis process of DN hydrogels inherently results in the shielding of defects from both networks. The defects in the first network represent the initial sacrificial bonds, but global failure is prevented by high 2nd network density, while 2nd network defects are shielded by the locally high stiffness of 1st network bonds.
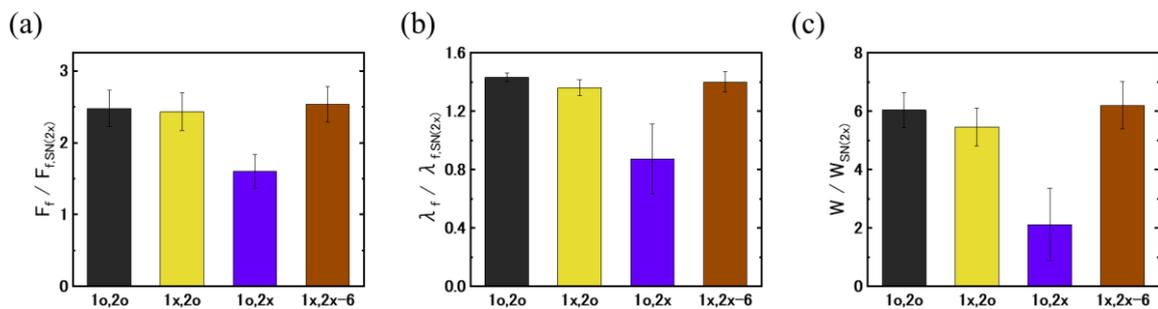
Figure 14. Comparing the mechanical properties of "real" Macro-DN composites to a single network material. (a) Fracture force, (b) fracture stretch, and (c) work to fracture. The macro-DN architecture provides a method to exhibit mechanical properties equivalent to a defect-free network, and significantly increased compared to single network.
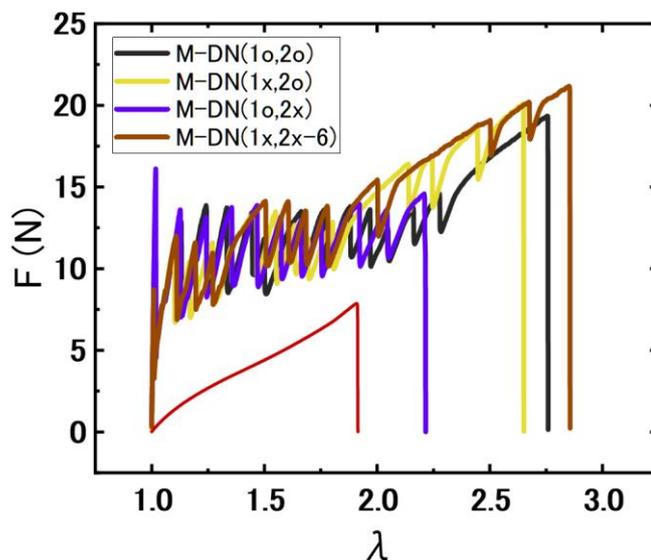
Figure 15. Comparing the mechanical properties of different Macro-DN architectures to the 2nd network containing a defect. The labels of the different Macro-DN systems are included in the legend. The thin red line represents the "real" 2nd network, SN(2x).

4.6 Conclusions

In molecular-scale double networks, both networks will inherently contain a large number of defects introduced by the synthesis mechanism. On the macroscale the sheer number of potential defects is lower, yet it is still possible to demonstrate how they influence the fracture process. With a sufficiently strong 2nd network, 1st network defects can be ignored, resulting in an obvious local necking phenomenon. Likewise, 2nd network defects are

protected by strong regions of 1st network. The combination of these two effects causes the phenomenon known as the "double-network effect," resulting in significant toughening compared to regular single network materials. We show that on the macroscale, we can increase the strength, fracture stretch, and work to fracture by factors of ~2.5x, ~1.4x, and ~6x, respectively. Furthermore, we show that a "real" Macro-DN system that contains defects in both networks is capable of exhibiting properties equivalent to a defect-free "perfect" Macro-DN composite. In all cases, the mechanical response can be understood through a simple analytical model. These findings shed light on the mechanism that has revolutionized the field of hydrogels and other soft materials and should help expand this concept to other materials systems.

CHAPTER 5

Improving the Strength and Toughness of Macro-scale Double Networks by Exploiting Poisson's Ratio Mismatch

This work was published as Okumura, T., Takahashi, R., Hagita, K. *et al.* Improving the strength and toughness of macroscale double networks by exploiting Poisson's ratio mismatch. *Sci Rep* **11**, 13280 (2021). https://doi.org/10.1038/s41598-021-92773-0 under a Creative Commons Attribution 4.0 International License. It has been modified from its original form.

5.1 Introduction

In Chapter 3, we developed Macro-DN materials made of a hard grid-shaped skeleton imbedded in a soft matrix, and these Macro-DN materials show some common features with molecular-scale DN materials. The roles of the hard skeleton and soft matrix match those of the 1st and 2nd network of DN hydrogels, respectively: the skeleton dissipates energy by rupturing sacrificially, while the matrix maintains extensibility. Since mechanical properties of the Macro-DN materials depend much more on material selection and geometric design of the skeleton rather than molecular design, Macro-DN materials can be developed facilely by utilizing 3D printing technology. 3D printing can directly print the skeleton as reinforcing phase with the desired structure and geometry to enable bending, rotation, or sacrificial bonds.[15,56,69,75–77] In the Macro-DN materials introduced in **Chapter 3** and **Chapter 4**, which utilized a hard grid skeleton imbedded in a soft matrix, the matrix of the composite carries almost no stress before breaking the rigid lattice, and the yield force and stiffness of the Macro-DN material are comparable to that of the individual skeleton. The role of the soft matrix was to maintain global integrity of the composite after breaking of the rigid interconnects, and local deformation only occurs in the regions that have fractured. Furthermore, the maximum strength of the composite was limited to the fracture strength of the skeleton in the low stretch region,

and to the matrix at ultimate fracture. The combination of these two points limits the increase in toughness to approximately a factor of two, when compared to a neat, defect-free matrix sample.

In order to achieve higher strength and toughness in Macro-DN materials, it is necessary to introduce a unique macroscopic mechanism in which the deformation of the skeleton and the matrix are strongly coupled even before the rupture of the skeleton. In this case, the skeleton not only dissipates energy through fracture but also acts to apply stress on the matrix to increase the strength of the composite in a synergistic manner. It is known that the preferential design of a reinforcing phase in composites with interpenetrating phase structures enable additional plastic deformation, resulting in increased strength and toughness.[78–80] This effect has been demonstrated on both the macro- as well as the microscale.[81] Recently, it has been shown that 2D re-entrant honeycomb reinforced structures that exhibit auxetic characteristics under compression improve mechanical performance such as impact resistance when modulus mismatch exists between the two phases.[56,76,82,83] Here, our interest is in soft composite materials that can exhibit high strain at break with ductile characteristics under tensile deformation, along with high stress. To realize this effect, we present a strategy to design skeletons that can exhibit transverse deformations under uniaxial tensile strain prior to rupture as sacrificial bonds. We design sacrificial skeleton networks that can increase or decrease their planar area with deformation, which induces size mismatch with the soft matrix that intends to maintain an almost constant volume during deformation. The correlation between the longitudinal and lateral deformations of materials is characterized by Poisson's ratio (μ), defined as the negative ratio of lateral contraction strain (ε_x) to the longitudinal extension strain (ε_y) of a material (or structure). The Poisson's ratio of isovolumetric materials is $\mu = 0.5$. In contrast, planar honeycomb structures have a

Poisson's ratio larger than 0.5, while planar auxetic structures that expand in the lateral direction when being stretched have a negative Poisson's ratio.[84–86] Both honeycomb and auxetic structures provide simple methods to tune the mechanical coupling between the rigid skeleton and soft matrix in Macro-DN composites, which can be characterized by the difference in the Poisson's ratio, $\Delta\mu = \mu_{skeleton} - \mu_{matrix}$.

In this Chapter, we fabricated three categories of two-dimensional skeleton structures: auxetic, offset rectangle, and honeycomb, and investigated the mechanical properties of the macroscale planar composites by uniaxial tensile testing. The mismatch in Poisson's ratio exerts biaxial stress on the soft matrix before the skeleton ruptures, and the mechanical behaviors and the rupture processes of the composites were analyzed. Taking advantage of the planar structure, we also performed real-time birefringence visualization of the stress distribution during uniaxial tension. The stiffness, fracture force, and work of extension were characterized for each composite as a function of the Macro-DN Poisson's ratio mismatch, $\Delta\mu$. We see that when the magnitude of Poisson's ratio mismatch is high, regardless of whether it is negative or positive, the impact of reinforcement significantly increases. Furthermore, we show that these Macro-DN materials exhibit enhanced toughness due to improved matrix deformation by large Poison's ratio mismatch with the skeleton, rather than just through sacrificial bonds. From these results we propose a new strengthening mechanism for Macro-DN materials via Poisson's ratio mismatch.

5.2 Experiments

5.2.1 Materials

The skeleton and the matrix were used for the plastic material (AR-M2, Keyence Co) and the silicone rubber solution (a commercially available two-part kit, KE-1603-A, and KE-1603-B, Shin-Etsu Chemical), respectively. See **Section 3.2.1** for details.

5.2.2 Skeleton Fabrication

The plastic skeletons were designed by CAD software (Inventor, Autodesk Inc. and Shade 3D, Shade 3D Co., Ltd.) and 3D printed (AGILISTA-3000, Keyence). **Figure 1a** shows a schematic illustration of the skeleton with auxetic structure (40°), as an example. The dimensions shown in **Figure 1** is in mm, which were kept constant throughout this paper. Full control over geometry is available, however parameters 1 and 5 from **Section 3.2.2** were not changed throughout this Chapter. Parameter 2-4 have been modified however, as shown below:

(2) The geometry of the skeleton without handles was maintained for all samples with of 24.5 mm, length of 60 mm, and thickness of 2 mm (**Figure 1a**). Open functional structures were chosen to enable topological interlocking and improve force transmission between the skeleton and matrix.

(3) The skeleton interconnects were fabricated with a constant width of 0.5 mm (**Figure 1b**) and a thickness of 2 mm. Three types, auxetic, offset rectangle, and honeycomb, with a total of 5 specific geometries were fabricated. These geometries were controlled by changing the internal angle ($\theta = 40°$ - $140°$) (**Figure 1c**). The internal width of each cell was fixed at 5.5 mm. The length of each longitudinal segment (denoted as L in **Figure 1**) changes depending on the internal angle: 40°, 10 mm; 60°, 8.8 mm; 90°, 7.6 mm; 120°, 5.3 mm; 140°, 2.9 mm. A row with three cells and a row with four cells were designed respectively. Therefore, the skeleton has four rows with three cells and three rows with four cells alternating. Half-finished rows of four cells were added at both ends to unify the length of the skeleton without handle.

(4) A spacer was designed around the exterior of the skeleton to fix the skeleton in the middle of the matrix and maintain a total composite thickness of 4 mm and was removed prior to sample testing.

After printing, the skeletons were washed in deionized water to remove the support material and dried prior to composite fabrication.
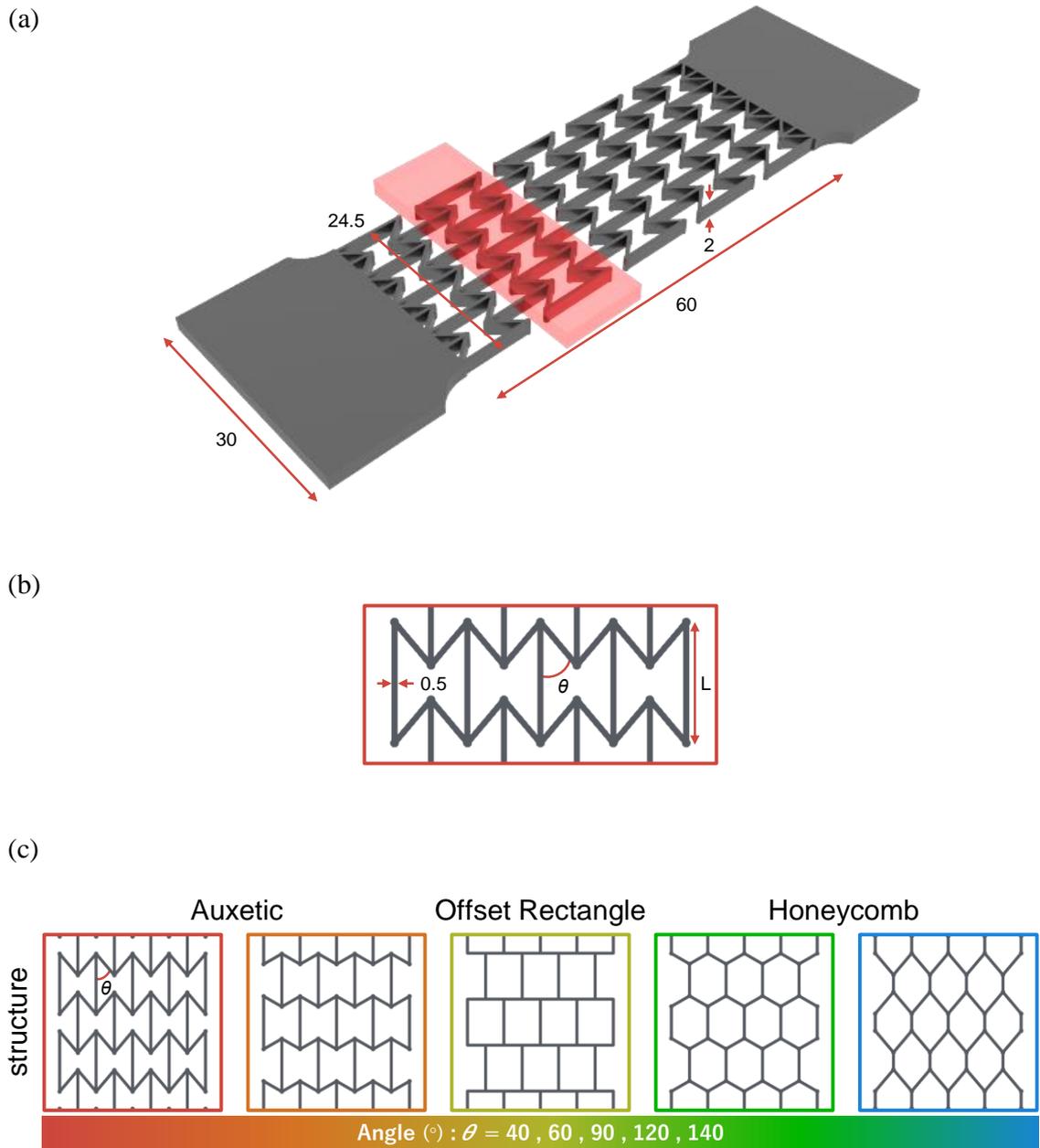
Figure 1. Dimensions of the skeleton with auxetic structure (40°). All dimensions are listed in mm. (a) Schematic of the skeleton. (b) Section of the red plane, the specific geometry by internal angle. (c) Schematic illustrations of the skeleton geometries utilized and their respective internal angles.

5.2.3 Synthesis of Macro-DN composites and pristine matrices

See **Section 3.2.3** for details on how to fabricate the Macro-DN composite and pristine matrix. After that, the sample was cut into specific dimensions ($l_0 \times w_0 \times t_0 = 60 \times 27 \times 4$ mm^3) using a laser cutter (PLS4.75, Universal Laser Systems). For the pristine silicone rubber (matrix), the samples were prepared with the same formulation and polymerization conditions as those of the composites for the mechanical tests in the absence of the plastic skeletons. In **Figure 2a**, a schematic is presented of the skeleton in **Figure 1a** embedded in silicone elastomer. The dimensions shown in **Figure 2** is in mm, which were kept constant throughout this paper. Two cross-sectional images are shown corresponding with the colored planes in **Figure 2a**. **Figure 2b** is a cross-sectional image of the plane highlighted in red, containing the row with three cells. **Figure 2c** is a cross-sectional image of the plane highlighted green, containing the row with four cells. The sample is embedded on all sides by silicone rubber. The dimensions listed represent the programmed values sent to the 3D printer. This results in a sample with 1 mm of rubber between the surface and the top of the skeleton, and more than 1.25 mm of rubber separating the side from the edge of the skeleton (**Figure 2b** and **Figure 2c**).
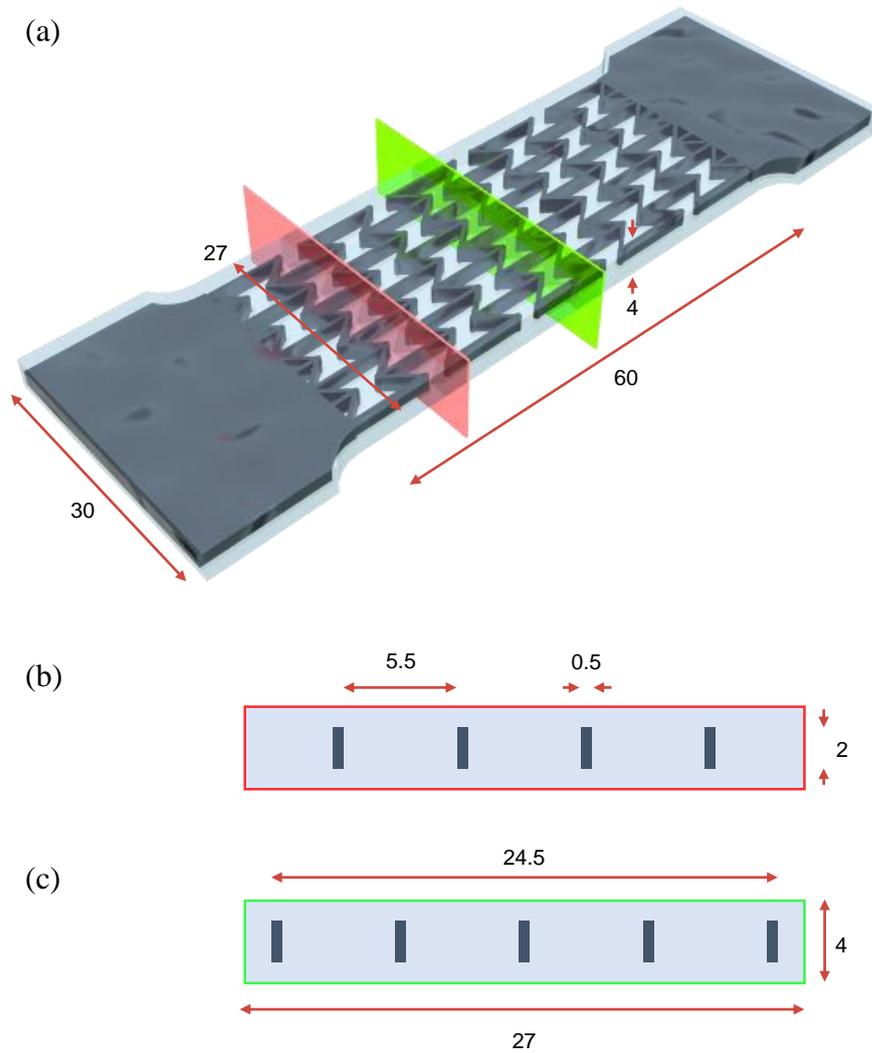
Figure 2. Schematics of the fabricated composite. All dimensions are listed in mm. (a) Schematic of the skeleton embedded in elastomer. (b) Cross-section of the red plane, containing three cells. (c) Cross-section of the green plane, containing four cells. The dark blue phase represents the skeleton while the light blue represents the matrix.

5.2.4 Tensile tests

Uniaxial tensile testing was performed on the composites, pristine silicone rubber (matrix), and the neat skeletons using a tensile-compressive tester (Instron 5965 type universal testing system). All samples were stretched along the length direction at an extension rate of 100 mm/min at room temperature. Stretch ratio, λ, is defined as l/l_0, where l_0 and l are the length of the sample before and during elongation, respectively. All stretching experiments were recorded visually with a video camera (Panasonic VX985M).

5.2.5 Cycle tests

Cyclic loading/unloading tensile tests were performed on the composites, pristine matrix, and neat skeletons using a tensile-compressive tester (Instron 5965 type universal testing system). All samples were stretched to a stretch ratio of $\lambda = 1.083$ at a velocity of 100 mm/min. Then, samples were returned to the initial displacement immediately at the same velocity as stretching. This process was repeated 5 times for the samples.

5.2.6 Circular polarized imaging system

To observe the stress distribution during deformation and fracture of the samples, a homemade circular polarizing imaging system was combined with tensile testing. A white lamp and a video camera were set in front of and behind the sample, respectively. Two pieces of circular polarizer films were fixed, respectively, on the white lamp and video camera. The video camera recorded the shape and isochromatic images of the samples during stretching. This simple method allows us to qualitatively visualize the stress distribution of the samples during deformation.

5.3 Results & discussion

5.3.1 Design of Macro-DN composites with Poisson's ratio mismatch

As model materials, the rigid skeleton is made from a polyurethane/polyacrylate (PU/PA) copolymer resin that is formed by 3D printing, and the soft matrix is a commercial elastic silicone rubber. The mechanical properties of these two materials are significantly contrasting, with the PU/PA resin possessing a modulus more than three orders of magnitude greater than the silicone (**Table 1** in **Chapter 3**). The composites are designed based on three types of geometries: auxetic, offset rectangle, and honeycomb skeletons (**Figure 3**). Specific details can be seen in **Section 5.2.2-5.2.3** and **Figure 1** and **Figure 2**. First, we will analyze the neat skeletons independently, schematically shown in black. Poisson's ratio (μ) is defined as the negative ratio of transverse contraction strain (ε_x) to the longitudinal extension strain (ε_y) of a material as follows:

$$\varepsilon_x = (w - w_0)/w_0, \quad \varepsilon_y = (l - l_0)/l_0, \quad \mu = -\frac{\varepsilon_x}{\varepsilon_y} \tag{1}$$

where l and l_0 represent the current length and initial length along the stretching direction, w and w_0 represent the current width and initial width perpendicular to the stretching direction, respectively (**Figure 3a**). We systematically change the planar Poisson's ratio of the skeleton by changing the interior angle θ of the mesh. Specifically, an auxetic mesh ($\theta < 90°$) has a negative Poisson's ratio, showing expansion in the dimensions normal to the stretching direction, as shown in the representation in **Figure 3a**. An offset rectangle mesh ($\theta = 90°$) has a Poisson's ratio near 0.5, as shown in **Figure 3b**. On the other hand, a honeycomb mesh ($\theta > 90°$) has a Poisson's ratio much larger than 0.5, showing large contraction in the dimensions normal to the stretching direction, as shown in **Figure 3c**. **Figure 3d** shows the measured Poisson's ratio of the matrix (black solid line) and each skeleton with different internal angle (open symbols). These values are calculated by using images of the samples taken at a stretch ratio, $\lambda = \frac{l}{l_0} = 1.02$ during tensile testing. An example of how planar Poisson's ratio was measured is shown in **Figure 4**. The

pristine matrix has a Poisson's ratio of $\mu_{matrix} = 0.48$. In the case of the neat skeletons, the Poisson's ratio, $\mu_{skeleton}$, could be controlled from below -2 to 4 as the internal angle, θ, increases. The relation between $\mu_{skeleton}$ and θ could be represented by a linear regression (dashed line) in **Figure 3d**.

By introducing these functional skeletons with different internal angles into a nearly incompressible soft matrix (shown in gold in **Figure 3a-c**), we can produce two regions where mismatch of Poisson's ratio between skeleton and matrix, $\Delta\mu = \mu_{skeleton} - \mu_{matrix}$, changes from negative to positive (**Figure 3d**, yellow regions). We aim to clarify the effect of this mismatch on the mechanical behavior of the Macro-DN composites. Depending on the functional structure, the skeleton will apply a different biaxial stress (e.g. compression or extension) on the matrix during deformation. **Figure 3a** shows a schematic of an auxetic mesh ($\mu_{skeleton} < 0$) embedded within an elastic, nearly incompressible matrix. Upon stretching by an external force, the 2D auxetic mesh expands in the lateral dimension while the matrix intends to contract in lateral direction. If the mesh is stiffer than the matrix, this negative mismatch in Poisson's ratio ($\Delta\mu < 0$) will cause the matrix to undergo biaxial extension, denoted by the blue arrows. Due to the near-incompressibility of the matrix, it will contract in the thickness direction. For the offset rectangular structure ($\mu_{skeleton} \approx 0.5$), the Poisson's ratio mismatch is very small ($\Delta\mu \approx 0$), and both skeleton and matrix deform similarly with negligible force transfer between the two components (**Figure 3b**). **Figure 3c** shows a schematic of a honeycomb structure ($\mu_{skeleton} > 0.5$) embedded within an elastic matrix. In this case, the positive Poisson's ratio mismatch ($\Delta\mu > 0$) will apply a lateral compression to the matrix at stretching, which causes the matrix to expand in the thickness direction to compensate for this biaxial compression. In both cases, the matrix is undergoing additional deformation that would not occur when the Poisson's ratio of the skeleton and matrix are matched. The Poisson's

ratio of the resulting composites as a function of the internal angle of the skeleton are shown as solid symbols in **Figure 3d**. Poisson's ratio of the composites closely matches the numerical average of the two components, $\frac{\mu_{skeleton} + \mu_{matrix}}{2}$, due to the similarity in stiffness of the two phases (**Figure 5**).

(a) Auxetic (Δμ < 0)

(b) Offset Rectangle (Δμ ≈ 0)

■ : Skeleton
▨ : Soft matrix
◄ : External force   ◄ : Resistance force
◄ : Deformation force of skeleton applied on matrix

(c) Honeycomb (Δμ > 0)
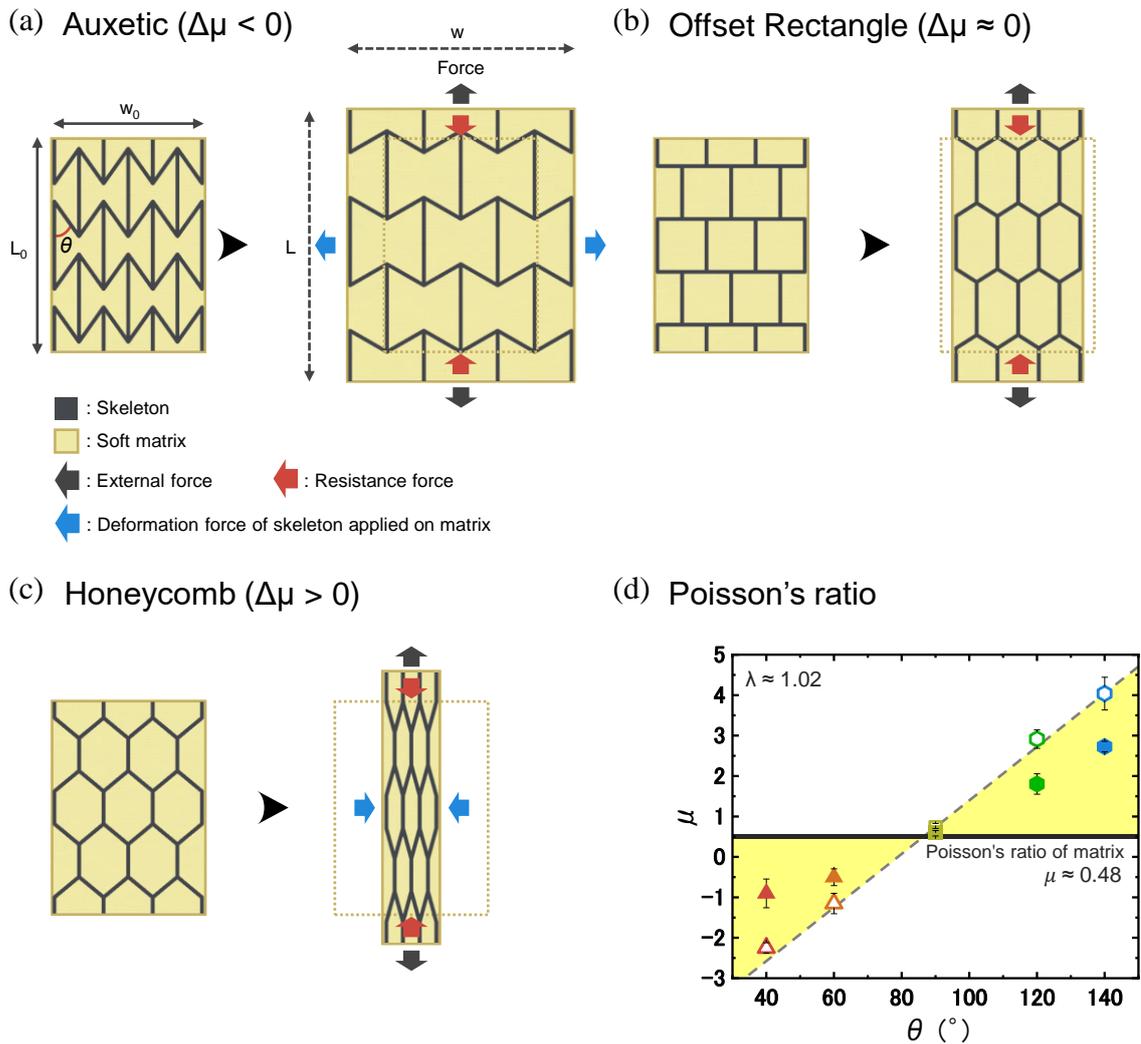
(d) Poisson's ratio

Figure 3. Hypothesis of the mechanism by which Poisson's ratio mismatch between components influences the deformation process of Macro-DN composites. Predicted deformation and force balance of (a) an auxetic composite, (b) an offset rectangular composite, and (c) a honeycomb composite. Here, each skeleton mesh shows how it deforms differently in response to tensile force, due to their varying planar Poisson's ratio, μ. The internal angle and defined lengths for measuring Poisson's ratio are shown in (a). The auxetic skeleton causes the matrix to undergo biaxial extension, while the honeycomb composite causes the matrix to experience compressive forces. (d) Poisson's ratio of matrix (solid black line), skeleton (open symbols), and composite (filled symbols) as a function of skeleton angle, θ. The exact design of these skeletons is shown in **Figure 1**. The highlighted yellow areas represent regions where Poisson's ratio mismatch ($\Delta\mu$) occurs between skeleton and matrix. The measured Poisson's ratio of composites falls between the measure value of the skeleton and matrix. The dashed line is a linear regression for the relation between angle, θ, and Poisson's ratio of skeleton, $\mu_{skeleton}$.

102

(a) Skeleton (Auxetic (40°))

$\lambda = 1.00$

$\lambda = 1.02$

$L_0 = 60.00$ mm
$w_0 = 27.00$ mm

$L = 61.20$ mm
$w = 28.19$ mm

(b) Composite (Auxetic (40°))

$\lambda = 1.00$

$\lambda = 1.02$

$L_0 = 60.00$ mm
$w_0 = 27.00$ mm

$L = 61.20$ mm
$w = 27.33$ mm

(c) Skeleton (Honeycomb (140°))

$\lambda = 1.00$

$\lambda = 1.02$

$L_0 = 60.00$ mm
$w_0 = 27.00$ mm

$L = 61.20$ mm
$w = 25.02$ mm

(d) Composite (Honeycomb (140°))

$\lambda = 1.00$

$\lambda = 1.02$

$L_0 = 60.00$ mm
$w_0 = 27.00$ mm

$L = 61.20$ mm
$w = 25.51$ mm
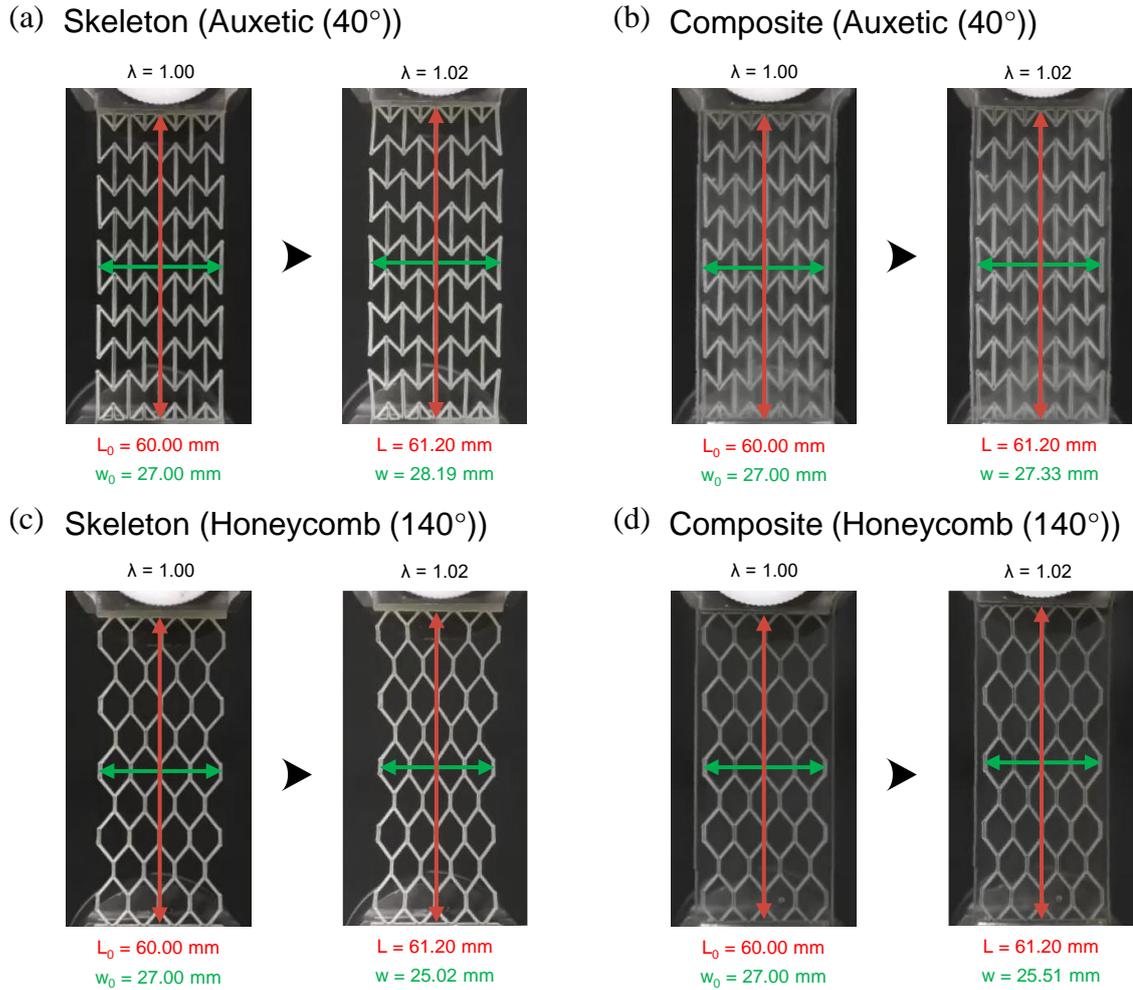
Figure 4. Optical images of the neat skeletons and their composites used for measuring the planar Poisson's ratio. The measurements were performed at a stretch ratio $\lambda = 1.02$ from the relation $\mu = -\dfrac{(w-w_0)/w_0}{(L-L_0)/L_0}$, using the data shown in the figures. w was the central width of the skeletons. (a) An auxetic skeleton. (b) A composite with auxetic skeleton. (c) A honeycomb skeleton. (d) A composite with honeycomb skeleton.
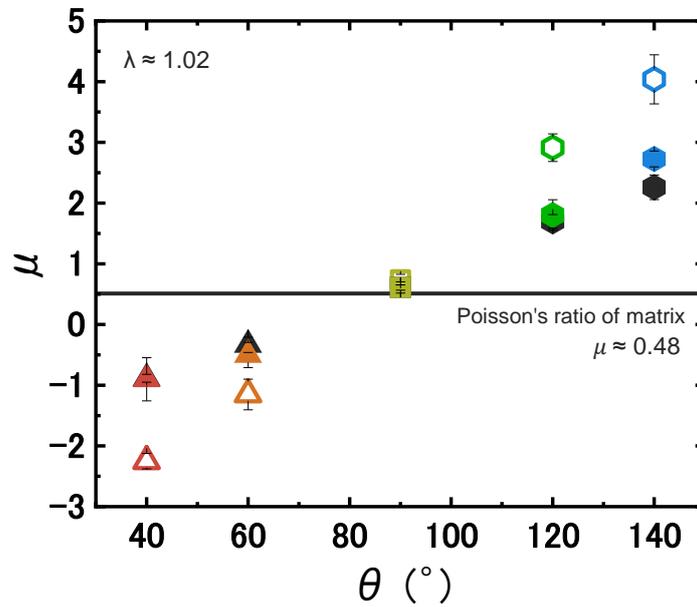
Figure 5. Experimental Poisson's ratios, m, of the neat skeletons (open symbol) and Macro-DN composites (filled symbol) measured at stretch ratio of λ = 1.02. The numerical average of the skeleton and matrix for each angle (average value = $\frac{\mu_{skeleton}+\mu_{matrix}}{2}$) are shown as solid black symbols. The experimental Poisson's ratios of the composites closely match the numerical average of the skeleton and matrix. The symbols represent the average of at least n = 3 trials and error bars represent the standard deviation.

5.3.2 Tensile behavior of composites with varying mismatch in Poisson's ratio

To demonstrate the impact of the functional skeleton designs described in **Section 5.3.1**, we first measure and compare the mechanical properties of the soft matrix, representative functional skeletons, and the resulting composite structures by tensile testing. Representative samples with internal angles of 40° (auxetic, $-\Delta\mu$), 90° (offset rectangle, $\Delta\mu \approx 0$), and 140° (honeycomb, $+\Delta\mu$), are shown in **Figure 6a-c**, respectively. From the resulting force versus stretch ratio curves, we see that the neat silicone rubber is elastic, fracturing at a stretch ratio of approximately 2.3. By comparison, the skeletons are much more brittle, fracturing at a stretch ratio of only ~1.1. In **Chapter 3**, we showed that when the fracture force of the 1st network matched that of the 2nd network, the mechanical properties of DN materials are optimized. However, in this system, the skeleton fracture forces are much lower than the matrix fracture force, and the skeleton stiffnesses are similar to that of the matrix, because the incorporated joints allow the skeleton to bend easily, despite the skeleton consisting of a much higher modulus material.

All composites had far better mechanical properties than the component materials. Surprisingly in the low stretch ratio region, the composites exhibited much higher force and stiffness than the neat skeleton. In **Chapter 3** and **Chapter 4**'s Macro-DN composites, the initial peak force represented the yielding force of the composite, and this value matched the fracture force of the skeleton.[69] In the designs utilized here with compliant skeletons however, the yielding force greatly exceeded the fracture force of the skeleton. The force versus stretch ratio curves along with corresponding pictures will be described in order.
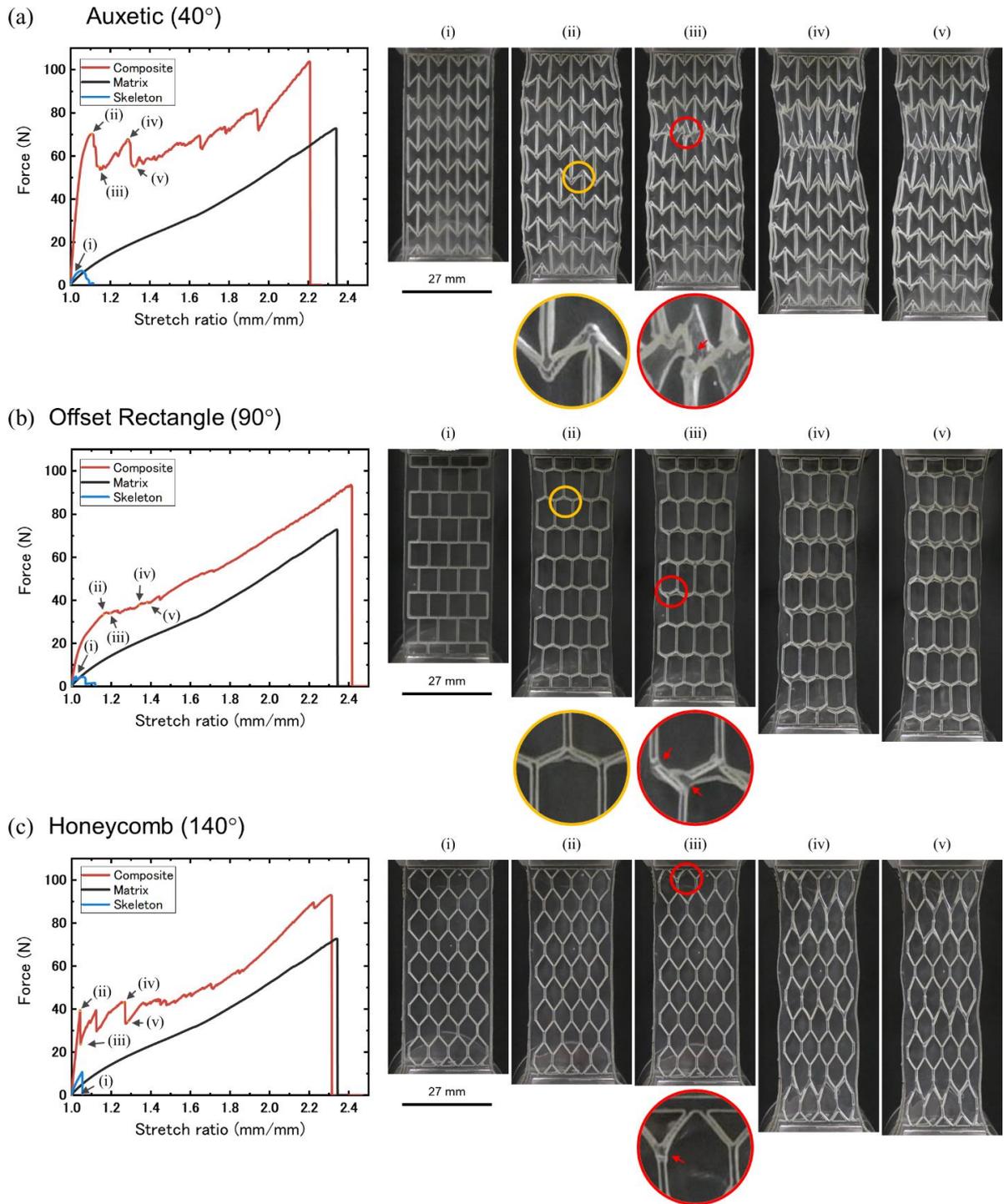
Figure 6. Uniaxial tensile behavior and internal fracture of the Macro-DN composites with skeletons of varying structure. Force-stretch curves of a neat skeleton (blue), pristine silicone rubber (black), and their composite (red). Yellow circles and red circles show where the delamination between the component materials and fracture of the skeleton occurred, respectively. (a) A composite with auxetic skeleton. (i-v) Images correspond to the labels in (a). (b) A composite with offset rectangle skeleton. (i-v) Images correspond to the labels in (b). (c) A composite with honeycomb skeleton. (i-v) Images correspond to the labels in (c).

First, we will examine the results of the auxetic (40°), -$\Delta\mu$ composite in **Figure 6a**. Images of the sample at corresponding stretch ratios can be seen in **Figure 6a(i-v)**. Upon stretching, a yield point is reached at a stretch ratio of 1.1, corresponding with the expansion of the skeleton (**Figure 6a(ii)**). At this time, since the interfacial bonding strength between the component materials is small, local delamination is observed. However, this does not result in sample failure because mechanical interlocking prevents large-scale delamination from occurring between the component materials. The yielding force is 68.5 ± 1.50 N, greatly exceeding the sum of the forces of the neat matrix and skeleton at that stretch ratio, demonstrating a synergistic increase in strength from the composite structure. After reaching the yield point the force of the composite dropped, representing fracture of the skeleton (**Figure 6a(iii)**). Load is then transferred from the skeleton to the matrix. With additional stretch, the sample became increasingly distorted, demonstrating high local deformation. With increasing stretch, the skeleton began to fracture preferentially numerous times, enabling high toughness (**Figure 6a(iv, v)**). These fracture processes show that the skeleton acts as a 1st network and dissipates energy, and the matrix acts as a 2nd network and supports the bulk of the load on the composite, in agreement with our previous work and double network theory. Finally, in the high stretch ratio region, the force of the composite exceeded that of the pristine matrix, even though the skeleton contained many fracture sites. The final fracture force was 98.53 ± 4.37 N, greatly exceeding the sum of the matrix and skeleton.

Next, we examine the offset rectangle (90°), $\Delta\mu \approx 0$ composite. Images of the sample at corresponding stretch ratios can be seen in **Figure 6b**. While the yield force is again much higher than the skeleton fracture force, compared to the auxetic composite the yield force is approximately half (32.18 ± 2.05 N versus 68.52 ± 1.50 N), and occurs at a larger stretch ratio (~1.2). During deformation, we do not see a pronounced change

in lateral geometry, in contrast to the auxetic composite (**Figure 6b(ii)**). Interestingly, in the ductile region, a jig-saw shaped force versus stretch curve was not observed, as has been previously seen in Macro-DN composites and in the auxetic composite (**Chapter 3** and **Chapter 4**). This demonstrates less load is supported solely by the skeleton, and the fracture process results in less transfer of force between the skeleton and matrix. However, as in the case of the auxetic composite, due to the deformation of the skeleton, slight local delamination is observed between the component materials. After internal fracture (**Figure 6b(iii)**) of the sacrificial bonds, global fracture of the sample occurs at ~90 N, greater than the sum of the components but less than the fracture force seen in the auxetic composite.

Finally, **Figure 6c** shows the force versus stretch ratio curve of a honeycomb (140°), $+\Delta\mu$ composite along with images of the sample at corresponding stretch ratios. The yield force is reached quickly at only a stretch ratio of 1.05 and achieves a force (38.4 $\pm$ 1.85 N) that exceeds the offset rectangle composite but is less than the auxetic composite. After the yield point, rupture of the skeleton occurs (**Figure 6c(iii)**), and the force drops. Since the yield force is reached at a low stretch ratio, the honeycomb composite does not show local delamination between the component materials as is seen in the auxetic and the offset rectangle composites. Increasing stretch ratio causes further deformation and sacrificial of the skeleton (**Figure 6c(ii-v)**), before final fracture occurs at a force exceeding the sum of the fracture forces of the skeleton and matrix. The global fracture force follows the general trend, greater than the offset rectangle design, and less than the auxetic composite.

The circular polarized images of the composites and a neat matrix sample during the tensile tests were taken (**Figure 7**). These images visualize the magnitude of the stress distribution during deformation of the composites. As seen from the neat matrix sample

(**Figure 7a**), in the unstretched state the sample has no molecular orientation and therefore appears completely dark. With stretching, we see a continual homogenous increase in the intensity of the coloring, turning from white to orange with the increase of stretch. In the case of the auxetic, $-\Delta\mu$ composite, regions in close proximity to the angled joints that bend with deformation initially become bright before the matrix that lies in the center of a unit cell (**Figure 7b**, $\lambda = 1.02, 1.03$). In the high stretch ratio region, even after rupture occurs within the skeleton, the stress is concentrated near the ruptured joints at a level that is higher than the stress in the pristine matrix at the same stretch (**Figure 7b**, $\lambda = 1.6$, 2.0). For the offset rectangle composite with little Poisson's ratio mismatch, the magnitude of deformation as judged by the coloring matches closely to that of the pristine matrix (**Figure 7c**). Because $\Delta\mu \approx 0$, the skeleton does not impose additional stress on the matrix, and the magnitude of deformation in the matrix with increasing stretch is similar to the neat matrix. Finally, **Figure 7d** contains the images of the honeycomb, $+\Delta\mu$ composite. In the low stretch region, $\lambda = 1.01$, the initial deformation appears in the center of the skeleton unit cell, due to the compression imposed by the skeleton. This result is significantly different from what was seen in the auxetic, $-\Delta\mu$ composite that undergoes local biaxial extension. Even at high stretch this observation continues ($\lambda = 2$), with brighter coloring occurring in the bulk of the unit cell rather than at the joints. Analysis via circular optical polarization confirms the stress exchange mechanism due to Poisson's ratio mismatch during the deformation in Macro-DN composites with functional structures.

An interesting observation from the images in **Figure 3** is that all samples exhibit deformation homogenously throughout the length of the composite at low stretch. This type of deformation process occurs because the stiffness of the functional skeletons introduced here allow for global deformation at low stretch, and the skeleton and matrix

are closely matched in stiffness. By comparison, in **Chapter 3** and **Chapter 4**'s Macro-DN design that was based on a rigid square-lattice design,[69] the skeleton was much stiffer than the matrix, resulting in an individual region undergoing significant deformation prior to the rupture of another region. With a very stiff skeleton, at small global stretch only a small portion of the sample (~10%) can deform. Due to Poisson's ratio mismatch and comparable stiffness, we observe a yield force and stiffness significantly greater than the neat skeleton, in contrast to the previous design where both yield force and stiffness match that of the skeleton.
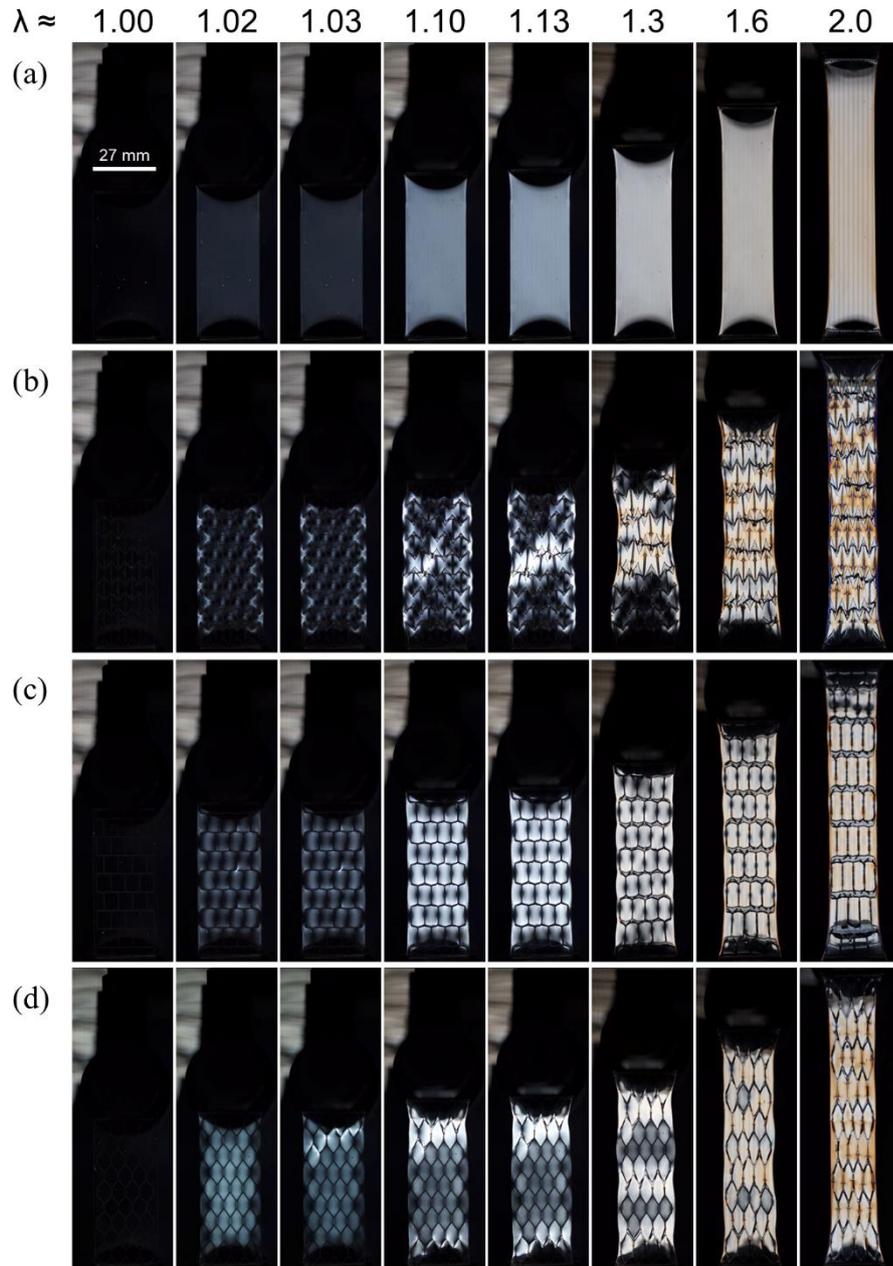
Figure 7. Circular polarized images of the Macro-DN composites under uniaxial tension. (a) Neat matrix. (b) Auxetic skeleton ($\Delta\mu$ = -2.73). (c) Offset rectangle skeleton ($\Delta\mu$ = 0.26). (d) Honeycomb skeleton ($\Delta\mu$ = 3.56). The completely dark images at λ=1 demonstrates the stress-free state of the composites prior to stretching, while the increase in coloring at λ >1 reveals the internal stress distribution of the samples.

5.3.3 Comparison of mechanical properties in the low stretch ratio region

The primary way in which the mechanical response introduced here differs from previous

research is the significant increase in yield force, compared to the neat components at

similar stretch. To investigate the origins of this response, we will focus our study to the lower half of the stretch region, up to $\lambda = 1.65$. We investigated the mechanical properties of the composite based on systematic modification to the geometry of the skeleton. The interior angle, θ, of the skeleton was varied between 40° and 140°, resulting in five types of skeletons exhibiting either auxetic ($-\Delta\mu$), offset rectangle ($\Delta\mu \approx 0$), or honeycomb ($+\Delta\mu$) response (**Figure 1c**). The mechanical properties were investigated by uniaxial tensile tests in the same way as **Section 5.2.4**.

First, we investigated the difference in mechanical properties of the neat components, with the results shown in **Table 1.** All skeletons exhibit similar stiffnesses, regardless of Poisson's ratio. Yield force and stretch ratio are also similar, with the exception of the 140° skeleton, that has a higher yield force, likely due to the high degree of alignment from the high internal angle. In **Table 1** in **Chapter 3**, we can see that both skeleton and matrix exhibited similar stiffnesses despite having neat material moduli that differ by three orders of magnitude (**Table 1**). One significant difference between the two components is that the matrix, as an elastic dissipator, has a much higher work of fracture.

Table 1. Mechanical properties of the neat skeletons and pristine matrix by uniaxial tensile testing.

Component	Structure	Angle, θ (°)	Poisson's ratio, μ	Initial Stiffness, κ (kN/m)	Yield Force, F_y (N)	Yield Stretch ratio, λ_y	Work of Fracture, W (mJ)
Skeleton	Auxetic	40	-2.25 ± 0.13	3.48 ± 0.06	6.41 ± 0.14	1.058 ± 0.003	23.77 ± 2.44
Skeleton	Auxetic	60	-1.15 ± 0.25	3.40 ± 0.25	5.40 ± 0.08	1.047 ± 0.005	14.52 ± 2.62
Skeleton	Offset Rectangle	90	0.74 ± 0.09	4.84 ± 0.24	4.80 ± 0.02	1.021 ± 0.003	23.25 ± 0.35
Skeleton	Honeycomb	120	2.91 ± 0.23	3.50 ± 0.24	5.87 ± 0.55	1.054 ± 0.016	14.47 ± 5.59
Skeleton	Honeycomb	140	4.04 ± 0.40	3.95 ± 0.18	12.47 ± 2.61	1.066 ± 0.012	28.64 ± 5.59
Matrix	-	-	0.48 ± 0.01	1.69 ± 0.02	-	-	2885 ± 312

Table 1. Mechanical properties of the composites and pristine matrix by uniaxial tensile testing and volume fraction of the skeletons in the Macro-DN composite. Data are average of at least n = 3 trials of different samples prepared by the same run.

Component	Structure	Angle, θ (°)	Poisson's ratio difference, $\Delta\mu$	Poisson's ratio, μ	Initial Stiffness, κ (kN/m)	Yield Force, F_y (N)
Composite	Auxetic	40	-2.73 ± 0.13	-0.90 ± 0.35	21.74 ± 0.59	68.52 ± 1.50
Composite	Auxetic	60	-1.63 ± 0.25	-0.50 ± 0.21	13.21 ± 0.47	41.69 ± 1.84
Composite	Offset Rectangle	90	0.26 ± 0.09	0.61 ± 0.09	8.96 ± 0.54	32.18 ± 2.05
Composite	Honeycomb	120	2.43 ± 0.23	1.80 ± 0.25	9.05 ± 0.36	22.41 ± 0.85
Composite	Honeycomb	140	3.56 ± 0.40	2.73 ± 0.13	15.26 ± 0.41	38.47 ± 1.85
Matrix	-	-	-	0.48 ± 0.01	1.69 ± 0.02	-

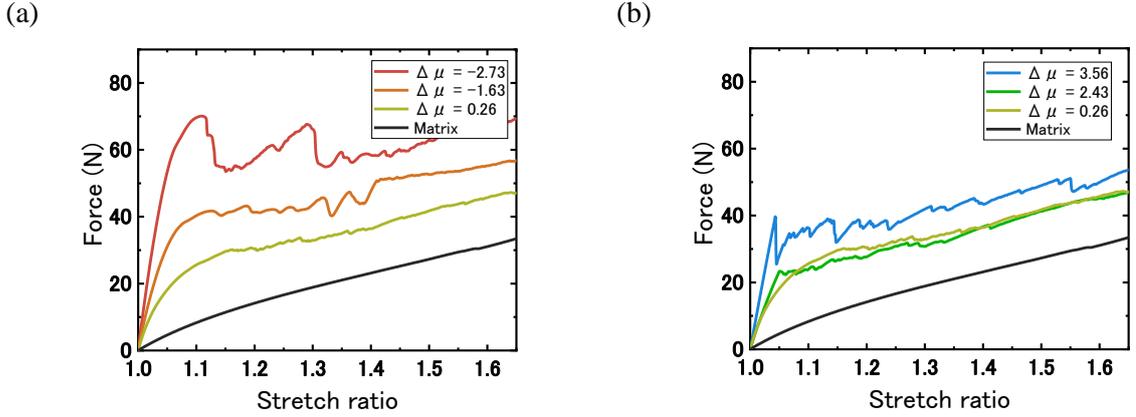| Component	Structure	Angle, θ (°)	Yield Stretch ratio, λ_y	Work of Extension, W (mJ) ($\lambda = 1 \sim 1.65$)	Volume fraction, $\varphi_{skeleton}$
Composite	Auxetic	40	1.112 ± 0.006	2232 ± 63	0.130
Composite	Auxetic	60	1.121 ± 0.005	1730 ± 95	0.093
Composite	Offset Rectangle	90	1.174 ± 0.003	1338 ± 68	0.076
Composite	Honeycomb	120	1.054 ± 0.011	1245 ± 29	0.072
Composite	Honeycomb	140	1.043 ± 0.002	1526 ± 72	0.080
Matrix	-	-	-	733 ± 14	-

Figure 8. Mechanical response of composites in the low stretch region (λ = 1.65). (a) Force versus stretch ratio curves for composites with internal angle equal to or less than 90°. (b) Force versus stretch ratio curves for composites with internal angle equal to or greater than 90°. As internal angle deviates from 90°, initial stiffness, yield force, and work of extension increases.

Next, we examine the force-stretch curves of the composite and the matrix, up to half of the maximum stretch ratio, λ =1.65. **Figure 8a** includes the samples with $\theta \leq$ 90°, and **Figure 8b** includes the samples with $\theta \geq$ 90°. In **Figure 8a**, we see that as the $\Delta\mu$ decreases to more negative values, yield force increases. The stretch ratio at which yielding occurs for the auxetic composites is much greater than what is seen for the neat skeletons (**Table 1**). In **Figure 8b**, we see the mirror effect: as $\Delta\mu$ increases to more positive values, yield force also increases, but less prominently in comparison with the case of negative $\Delta\mu$. For the honeycomb samples, the yield force occurs at a stretch ratio similar to that of the neat skeletons. The offset rectangle skeleton with an internal angle of 90° shows a Poisson's ratio closes to that of the neat matrix and shows an increase in yield force due to sacrificial fracture of the skeleton. In summary, as the internal angle of the skeleton deviates from 90° and the absolute magnitude of $\Delta\mu$ increases, we see a further increase in force as a function of stress, but the Poisson's ratio mismatch effect is much prominent in the case of negative $\Delta\mu$.

To more clearly see the effect that skeleton geometry has on the composites, we plotted the initial stiffness (**Figure 9a**), yield force (**Figure 9b**), and work of extension (**Figure 9c**) of the composites as a function of $\Delta\mu$. Work of extension was calculated as the area under the force versus stretch ratio curve, $W = L_0 \int_{\lambda=1}^{\lambda=1.65} F d\lambda$. While all composites show increased performance compared to the neat materials, we see that modifying the structure of the skeleton to possess $\Delta\mu$ with a large magnitude, either in the positive or negative direction, increases the mechanical performance of Macro-DN structures compared to the $\Delta\mu \approx 0$ design.

To better understand the improvement in mechanical properties of the composites we calculate the enhancement ratio (**Figure 9d-f**). The enhancement ratio for initial stiffness (κ_{enh}), yield force ($F_{y,enh}$), and work of extension (W_{enh}) are calculated as follows:

$$\kappa_{enh} = \frac{\kappa_{composite}}{\kappa_{skeleton} + \kappa_{matrix}} \tag{2a}$$

$$F_{y,enh} = \frac{F_{y,composite}}{F_{y,skeleton} + F_{matrix}(\lambda_{y,composite})} \tag{2b}$$

$$W_{enh} = \frac{W_{composite}}{W_{skeleton} + W_{matrix}} \tag{2c}$$

where the subscripts refer to the property of the specific component. The enhancement ratio describes the increase in a given mechanical response compared to the simple addition of each component: an enhancement ratio greater than 1 shows a synergistic increase in mechanical properties. In **Figure 9d**, the initial stiffness of the most strongly auxetic and honeycomb reinforced composites was enhanced by up to 4.2x and 2.7x, respectively, while the offset rectangle was enhanced by only 1.4x. The larger the magnitude of $\Delta\mu$, the higher the initial stiffness of the composite. To calculate the enhancement of yield force, we estimated the matrix contribution to yield force by using

the force in the matrix at the λ where the composite exhibits yielding, because the matrix does not exhibit a yield point independently. For yield force, the most highly auxetic skeleton reinforced composite showed an enhancement of up to 4.4x, and this value decreases as we approach $\Delta\mu \approx 0$ (**Figure 9e**), which exhibits an enhancement of 1.8x. However, as $\Delta\mu$ increases we see a slight increase in enhancement, with the most elongated honeycomb composite having a yield force enhancement of 2.3x. Because the incorporation of functional skeletons results in fracture forces that are greater than the fracture force of the combined neat components, we have developed a method to overcome a limitation of our previous macroscale design.

To understand why the response was stronger in auxetic than honeycomb composites, we compared the stretch ratio when yielding occurs for the neat skeleton and the composite (**Figure 10**). We see that the yielding stretch ratio is higher in auxetic and offset rectangle composites than in their neat skeletons but is lower in the honeycomb composite than the neat skeleton. From this finding, we believe that in the honeycomb composites, the matrix inhibits the free deformation of the skeleton during extension and resulting in greater stress within the skeleton of the composite than for the neat skeleton, resulting in early rupture of the reinforcing phase. While the enhancement of yield force for the honeycomb composites is not as pronounced, these composites still exhibit high toughness. The work of extension shows the same tendency as the initial stiffness, and the auxetic and honeycomb composite work of extension can be enhanced by up to 2.9x and 2.0x (**Figure 9f**), respectively, when compared to the neat matrix. We can clearly see that as the *magnitude* of $\Delta\mu$ increases in *either* the positive or negative direction, the better the mechanical properties of the composite. Interestingly, this result differs from the previous results of auxetic co-continuous composites prepared by Wang and coworkers, which exhibited a maximum in energy dissipation close to $\mu \approx 0$.[56]

When designing the functional skeletons, we aimed to keep the number of sacrificial bonds and the cross-section of these bonds constant, so that the stiffness and influence of sacrificial rupture could be compared among all skeletons. By maintaining this constant geometry, the volume fraction of the skeletons within the composites ($\varphi_{skeleton}$) were different, as shown in **Table 1**. The skeleton volume fraction of the offset rectangle structure and honeycomb structures were approximately 8%, while the most highly auxetic structure reached 13%. Taking the volume fraction into account, we estimated the efficiency ratio (**Figure 9g-i**) for the initial stiffness (κ_{eff}), yield force ($F_{y,eff}$), and work of extension (W_{eff}). These terms are calculated by:

$$\kappa_{eff} = \frac{\kappa_{enh}}{\varphi_{skeleton}} \tag{3a}$$

$$F_{y,eff} = \frac{F_{y,enh}}{\varphi_{skeleton}} \tag{3b}$$

$$W_{eff} = \frac{W_{enh}}{\varphi_{matrix}} \tag{3c}$$

Where $\varphi_{skeleton}$ and φ_{matrix} represent volume fraction of neat skeleton and pristine matrix, respectively. Energy dissipation takes places through two methods: 1) deformation of the elastic matrix by the skeleton, and 2) rupture of the sacrificial bonds within the skeleton. Since each skeleton regardless of design has the same number of sacrificial bonds, we assume that the work of extension is dependent on the volume fraction of the matrix. In **Figure 9g**, we see the efficiency results match those of enhancement ratio: as $\Delta\mu$ deviates from 0, stiffening efficiency increases. Despite having different volume fractions of skeleton, the auxetic, $-\Delta\mu$ composites and the honeycomb, $+\Delta\mu$ composites exhibit similarly high stiffening efficiencies. Regarding the yield force, **Figure 9h**, we again see the highest efficiency in the most highly auxetic composite, and the lowest value in the offset rectangle composite. The honeycomb composites also outperform the offset

rectangle composite. Finally, **Figure 9i** shows the work of extension versus Poisson's ratio. The auxetic structure shows the highest efficiency, as it can dissipate the most energy, even though it possesses less matrix to deform than the other composites. The honeycomb structure with the largest Poisson's ratio mismatch exceeded the offset rectangle work of extension efficiency but was lower than the auxetic design. In conclusion, we consider that the mismatch of Poisson's ratio between skeleton and matrix plays an important role for increasing the mechanical properties of Macro-DN designs, even when taking the loading fraction into account.
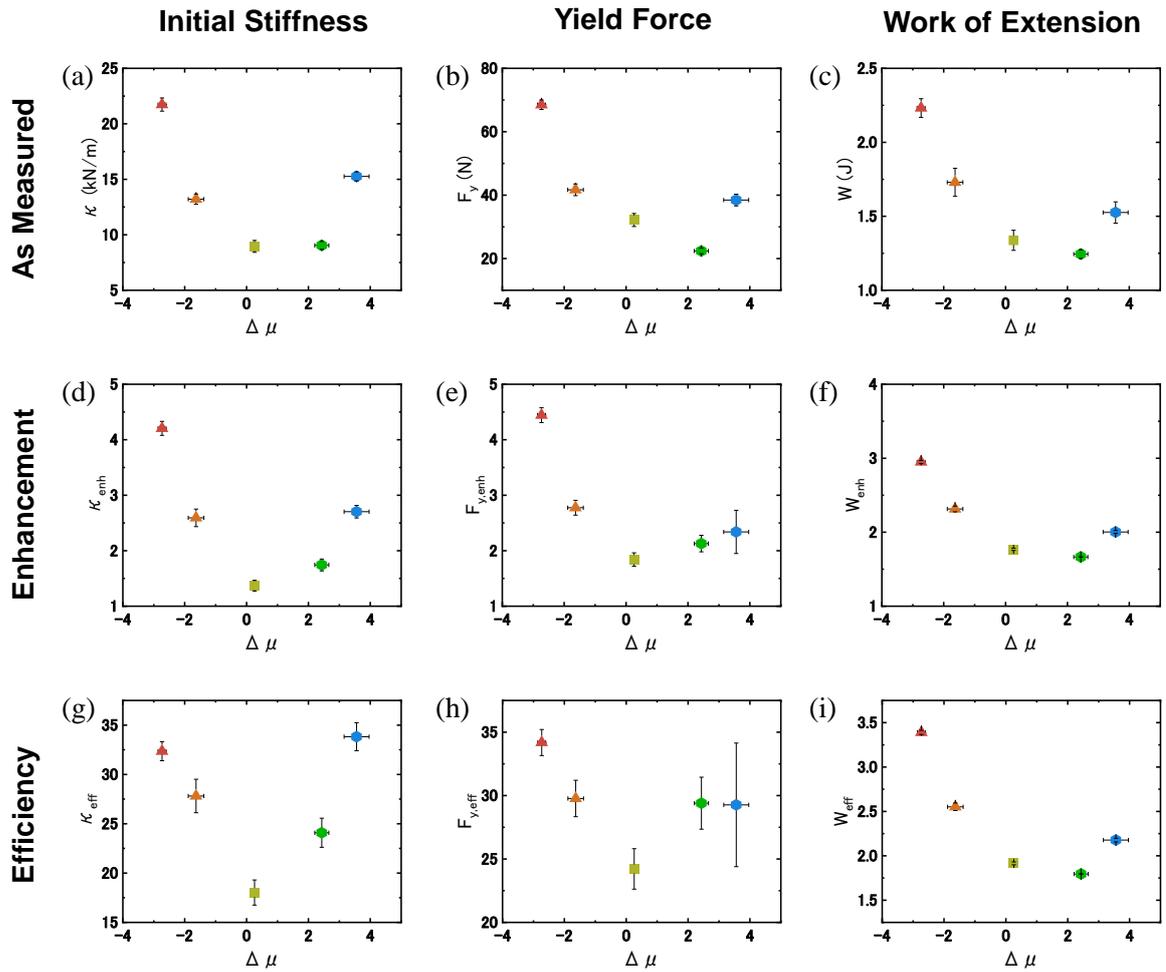
Figure 9. Effect of Macro-DN Poisson's ratio mismatch, _Δμ_, on the measured value, the enhancement ratio, and the efficiency ratio of the composite mechanical properties up to _λ_ = 1.65. Relationship between _Δμ_ and measured (a) stiffness, (b) yield force, and (c) work of extension. Enhancement ratio versus _Δμ_ for (d) stiffness, (e) yield force, and (f) work of extension. Stiffness, yield force and work of extension are normalized by the sum of the component materials. Efficiency ratio versus _Δμ_ for (g) stiffness, (h) yield force, and (i) work of extension. Stiffness and yield force are normalized by the volume fraction of the skeleton, and work of extension is normalized by the volume fraction of the matrix. Error bars for all plots represent the standard deviation from n > 3 samples.

Figure 10. Yield stretch ratio of the neat skeletons (open symbols) and Macro-DN composites (filled symbols) as a function of skeleton Poisson's ratio. Triangles represent auxetic samples, and hexagons represent honeycomb samples. The colors and shapes of the symbols correspo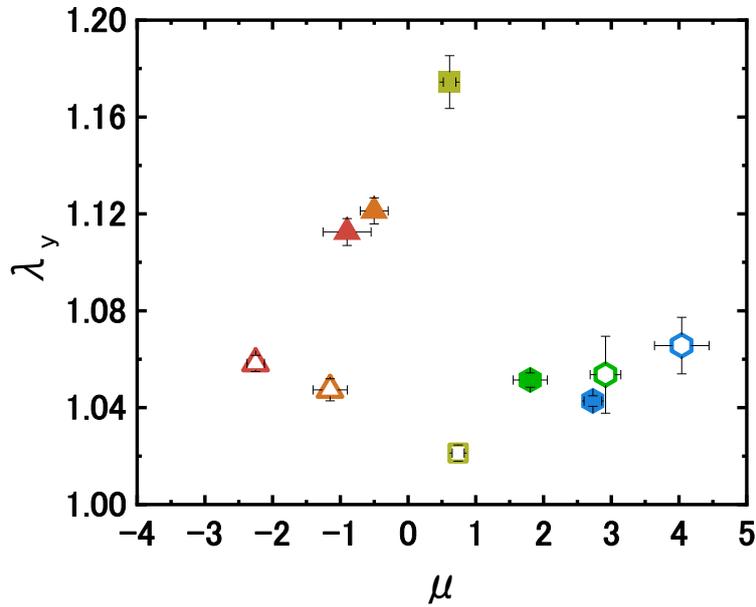nd with the internal angles in **Figure 3**. The symbols represent the average of at least n = 3 trials and error bars represent the standard deviation.

5.3.4 Investigating the impact of skeleton design in the elastic (no fracture) region

Traditionally the DN principle works to increase toughness by the rupture of sacrificial bonds, which occurs beyond the yield point. The incorporation of functional sacrificial networks results in significant improvement in strength (stiffness and maximum force) and toughness (work of extension), even in the stretch regime where the response is primarily elastic, and the network has not yet fractured. We studied the mechanical response in the stretch region prior to fracture to understand the role of functional structures on the deformation process.

In order to show the impact that the Macro-DN design has even without skeleton fracture, cyclic tensile testing was conducted up to a strain of ~8% ($\lambda = 1.083$), where the skeleton does not yet fracture in the composite ($\lambda < \lambda_y$). As an example, we used the

auxetic (40°), $-\Delta\mu$ composite, which exhibited the greatest enhancement in mechanical response, according to **Section 5.3.3**. First, the neat skeleton was tested (**Figure 11a**). Stress concentrations in the joints of the skeleton during the first stretching resulted in partial skeleton rupture at only a stretch ratio of 1.06. During subsequent stretching cycles, the mechanical properties of the skeleton continued to decrease. It should be noted that since the skeleton was plastically deformed by stretching, a slight negative force was observed when the stretch ratio returned to its original position. Next, the experiment was repeated for the pristine matrix (**Figure 11b**). The force generated by this test was very low but did not change upon with cycling, because the silicone elastomer is highly elastic. On the other hand, as seen in **Figure 11c**, in the composite the mechanical properties improved significantly compared to the neat components, exhibiting increased stiffness and maximum force. No fracture occurred in the skeleton within this stretch ratio region. The composite shows a compressive force after the first stretching cycle, and a decrease in maximum force after the first cycle. These results can be attributed to two effects. First, as mentioned before, during stretching the skeleton exhibits some plastic deformation. Upon unloading, the shape of the skeleton has slightly changed, resulting in compression when returning to the original position. Second, we can see from the snapshots of the stretching tests (**Figure 12**) that the matrix is able to debond from the skeleton during stretching, and this only occurs in the first stretching cycle. Despite these effects, even after repeated stretching the mechanical properties of the composite are superior to the component materials.

A comparison of the stiffness, maximum force, and energy dissipation (difference in work of extension during loading and unloading) can be seen in **Figure 11d-f**, respectively, for each component and the composite over five cycles. Since the skeleton begins to break, each subsequent step causes the skeleton to decrease in stiffness and

122

force. The pristine matrix and composite, in contrast, exhibit almost no change within the first five cycles. The energy dissipation exhibits more obvious changes. The energy dissipation was estimated from the hysteresis area, $W_{hys.}$, by:

$$W_{hys.} = L_0 \int_{\lambda=1}^{\lambda=1.083} (F_{load} - F_{unload}) d\lambda \tag{4}$$

where F_{load} and F_{unload} are the force during loading and unloading, respectively.

The skeleton and matrix show the same trends as before; the energy dissipation of the neat skeleton decreases with increasing cycle, while the matrix exhibits consistent but low energy dissipation. For the composite sample from the second cycle, the energy dissipation decreased by half, but the skeleton did not fracture. This decrease in hysteresis occurs due to the debonding of the matrix from the skeleton, resulting in the loss of an energy dissipation source. However, despite some degree of delamination occurring, there was no catastrophic failure of the sample, and continued cycling can occur without further decrease in performance. This result shows the importance of topological interlocking in forming robust composite materials. In this system, the biaxial expansion of the soft matrix by the functional skeleton had a large effect on toughness (energy dissipation), and the topological interlocking effect had a large effect on strength (stiffness and maximum force). Without requiring a strong interface, this method can create composite materials that exhibit excellent mechanical properties. Furthermore, since high interfacial strength is not a requirement, this opens the possibility for making a wide range of Macro-DN composites, with diverse materials combinations.
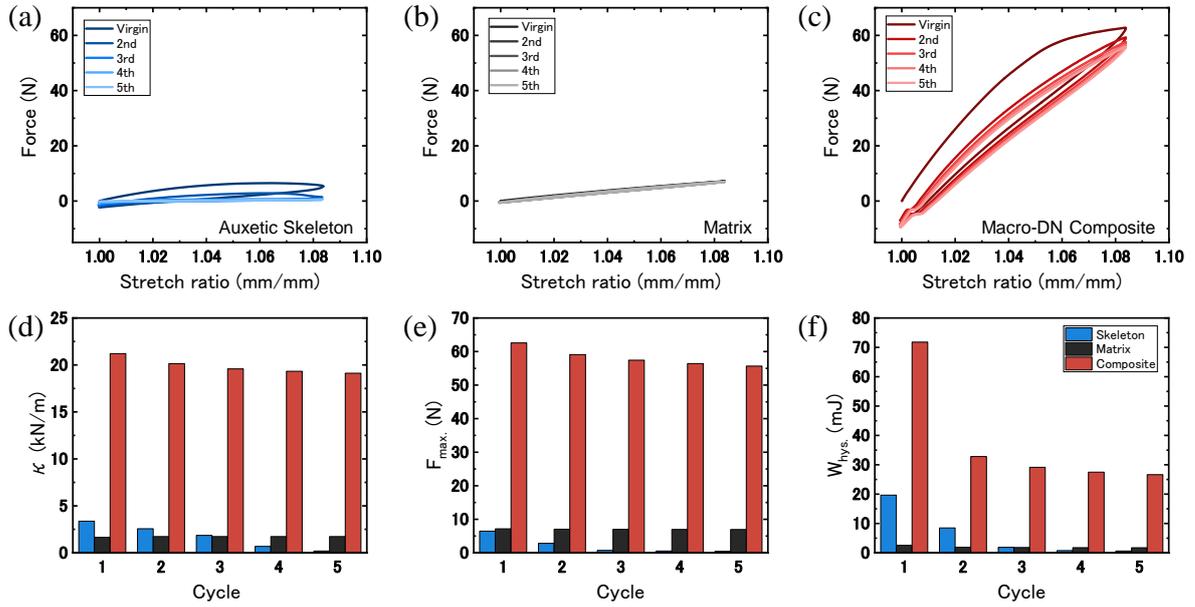
Figure 11. Cyclic tensile behavior of the auxetic, -Δμ Macro-DN composite. Force-stretch curves of (a) a neat auxetic (40°) skeleton, (b) the neat matrix (silicone rubber), and (c) the resulting Macro-DN composite. Comparisons of (d) stiffness, (e) maximum force, and (f) energy dissipation up to $\lambda = 1.083$, for the skeleton (blue), matrix (black), and composite (red) at different cycle numbers.
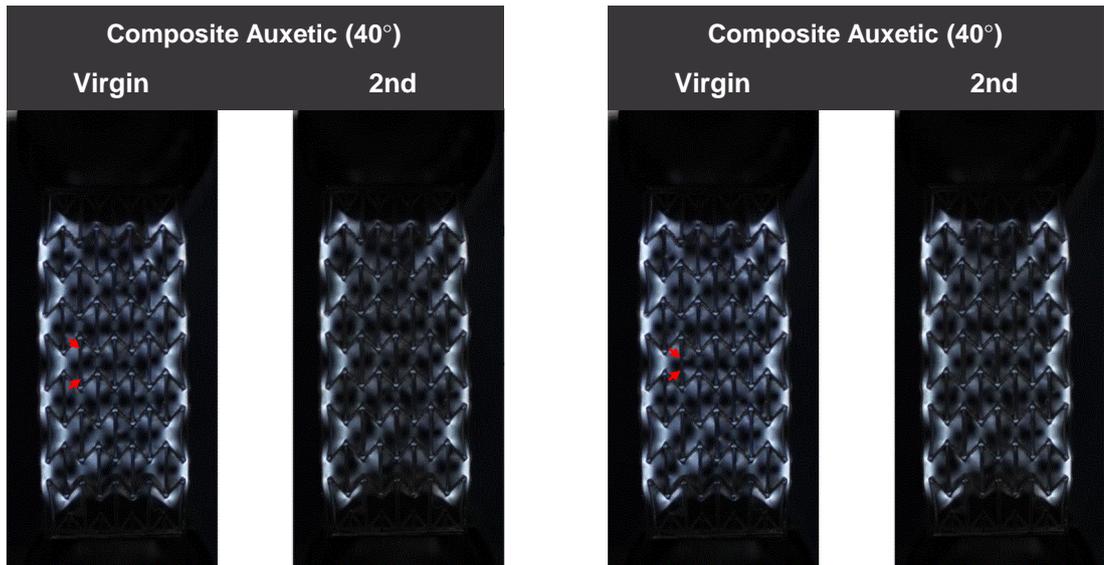
Figure 12. Cyclic tensile polarizing images of the auxetic, -Δμ Macro-DN composite. (a) Virgin and 2nd stretch in $\lambda \approx 1.07$. (b) Virgin and 2nd stretch in $\lambda \approx 1.08$. Red arrows show where the matrix is able to debond from the skeleton.

5.4 Conclusions

In summary, we have demonstrated that incorporating functional skeletons into the Macro-DN composite design improves the resulting mechanical response, especially in the low stretch region. Enhanced stiffness and toughness seen in Macro-DN composites are now known to originate from two sources: 1) the incorporated auxetic or honeycomb structures that exhibit strongly negative or positive Poisson's ratio mismatch ($\Delta\mu$), increasing deformation of the matrix prior to skeleton rupture, and 2) the preferential, repetitive rupture of the skeleton within the composite prior to matrix fracture, based on the DN principle. The method introduced here improves upon previous Macro-DN designs that increased toughness solely through the fracture of a sacrificial network. This new method simultaneously increases the work performed by the matrix, by incorporating biaxial deformation. Even if the interfacial adhesion strength between the skeleton and the matrix is poor, it is possible to improve the mechanical properties of composite structures through topological interlocking. This strengthening mechanism can be widely used for diverse combinations of hard skeletons and may serve as a guideline for the design of high strength soft/hard composites in the future.

CHAPTER 6

Fabrication of Highly Deformable Hydrogel Composites with Macroscopic Reinforcement

6.1 Introduction

Hydrogels have unique properties such as biocompatibility,[87,88] high-water content,[89,90] substance permeability,[91] and low friction,[92] making them highly applicable to various fields, notably artificial organs and drug delivery systems. Since the 2000s, numerous high-strength hydrogels comparable to living tissues have been developed, but there are still many problems in their application as high strength, load-bearing tissues or other industrial materials.[24,51,72,93] In order to develop even better mechanical properties with hydrogels, hydrogel composites that combine hydrogels with dissimilar materials that have properties contradictory to soft swollen matter have attracted attention.[38,39,94] However, a serious problem has limited the use of hydrogels as a matrix in combination with hard reinforcements: stress-induced deformation can occur due to volume change mismatch between the hydrogel and the hard reinforcement. In general, an inherent property of hydrogels is that they can absorb water and change volume significantly (swelling or deswelling) from the as-prepared state depending on the environment.[30,95,96] However, swelling the matrix does not inherently result in a change in the skeleton. As a result, the volume change of the hydrogel induced by swelling causes strong volume change mismatch and interfacial stress between the matrix and skeleton, resulting in surface creasing or bulk deformation, at best, and delamination or rupture, at worst.[97–99] Some hydrogel composites have been reported by using hydrogels in the as-prepared state or employing relatively low-swelling hydrogels as the matrix.[38,39,94] However, these approaches merely limit the impact of the induced stress and are not fundamental solutions to volume change mismatch. Furthermore, these approaches limit the types of

hydrogels that can be used as a matrix. As a result, the components of hydrogel composites have been highly selective. To overcome such limitations, Takahashi *et al.* succeeded in creating a hydrogel composite that does not suffer from volume change mismatch by using a low-melting-point alloy as a skeleton that can transform from the load-bearing solid state to a free-deformable liquid state at relatively low temperature.[16] In this method, any hydrogel that swells or shrinks can be used, but there is a restriction on the type of reinforcing material that can be used as the skeleton. Moreover, the interfacial strength between the component materials is low. It is also difficult to create complicated or 3D structured reinforcements for use in hydrogel composites.

To create novel hydrogel composites that are not restricted by hydrogel swelling or limited to specific types of component materials, we focus on the skeleton structure. The skeleton structure is required to deform to follow the volume change due to swelling or shrinking of the hydrogel. Inspired by the functional structures in **Chapter 5**, we focus on auxetic structures. In this research, we took 2D auxetic structures and incorporated them into a 3D structure for use as the skeleton. This structure can increase or decrease in length in all three dimensions, similar to the hydrogel matrix. In this research, we use a particle-based double-network hydrogel (P-DN hydrogel) as the model matrix. P-DN hydrogels are useful because they combine high toughness with a one-pot synthesis method.[100,101] Moreover, P-DN hydrogels can firmly adhere to various materials.[102] Therefore, we demonstrate the creation of a P-DN hydrogel composite with macroscopic auxetic reinforcement, which eliminates the volume change mismatch between components, despite having strong inter-component adhesion. As a result, when the auxetic hydrogel composite is immersed in aqueous solutions with various osmotic pressures, the skeleton of this auxetic hydrogel composite deformed according to the volume change of the hydrogel, successfully eliminating the volume change mismatch

between the component materials. The auxetic hydrogel composite exhibits high strength and toughness due to the DN principle and Poisson's ratio mismatch, as found in **Chapter 3** and **Chapter 5**, respectively. Moreover, the auxetic hydrogel composite shows J-shaped stress-strain curves and anisotropic swelling and deswelling due to the skeleton. Our method can make use any type of material that can be formed into a macroscopic auxetic structure, resulting in a method to significantly improve the mechanical response of a wide variety of hydrogels.

6.2 Experiments

6.2.1 Materials

The plastic material used to fabricate the rigid skeleton was AR-M2 (model material), purchased from Keyence Co. AR-M2 consists of acrylate monomer, urethane-acrylate oligomer and photoinitiator. During the printing of the skeleton, AR-S1 (Keyence Co) was used as a support material. AR-S1 consists of acrylate monomer, polypropylene glycol and photoinitiator. 2-acrylamide-2-methylpropane sulfonic acid (AMPS) was received courtesy of Toagosei Co., Ltd. and used as received for the rigid/brittle 1st network of the DN gel matrix. Acrylamide (AAm) was purchased from Junsei Chemical Co., Ltd. and used as received for the soft/ductile 2nd network of the DN gel matrix. MBAA (FUJIFILM Wako Pure Chemical Corporation), as a cross-linker for both 1st and 2nd hydrogel networks, was used as received. 2-Oxoglutaric acid (α-keto) (FUJIFILM Wako Pure Chemical Corporation), was used as a UV initiator for the hydrogelation reaction and was used as received.

6.2.2 Preparation of particle-based DN hydrogels

PAMPS particles and a PAAm network were used as the rigid/brittle 1st network and the soft/stretchable 2nd network, respectively. Bulk P-DN hydrogels were synthesized

through a two-step sequential free-radical polymerization. In the first step of the 1st network particle preparation, MBAA (4 mol%) and α-keto (0.1 mol%) were added to 1 M AMPS solution (the molar percentages of MBAA and α-keto are relative to the AMPS monomer). The solution was poured into a sealed glass container. Photoinduced free radical polymerization was carried out under argon atmosphere with a UV lamp for 10 h (UV light intensity was 3.9 mW/cm^2). After that, the as-prepared PAMPS hydrogels were roughly ground with a spoon into particles and dried using a vacuum oven for 24 h. Subsequently, the dried particles were finely ground with a blender (Hi-Power BLENDER MX1200XTM, waring commercial), and sifted, resulting in particles ranging in size from 106 to 300 µm. Then, the 1st network particles were added to the AAm aqueous solution (2 M) containing MBAA (0.1 mol%) and α-keto (0.1 mol%), where the concentration of PAMPS dried particles to AAm solution was 2.5 mg/mL, to obtain the paste-like precursors of the P-DN hydrogels. After that, the hydrogel particle solution was poured into a plastic spacer ($l_0 \times w_0 \times t_0 = 20.00 \times 28.55 \times 28.55$ mm^3) in the reaction cell consisting of a pair of glass plates with a 20 mm silicone spacer. Mold releasing films were attached to the inside of the plastic spacer to prevent chemical bonding between the P-DN hydrogel and the plastic spacer. The AAm monomers were photopolymerized under a UV lamp for 8 h in an argon atmosphere to obtain the bulk P-DN hydrogel (matrix). The neat P-DN hydrogels in deionized water exhibited isotropic swelling.

6.2.3 Designing reinforcing skeletons with various geometries

The plastic skeletons were designed by CAD software (Inventor, Autodesk Inc. and Shade 3D, Shade 3D Co., Ltd.) and 3D printed (AGILISTA-3000, Keyence). Two types of skeleton geometries are illustrated in **Figure 1** based on (a) auxetic and (b) rectangular structures. The dimensions shown in **Figure 1** are in mm, which were kept constant throughout this Chapter. Full control over geometry is available, however some

parameters were not changed throughout this Chapter:

(1) The 3D skeleton consists of a combination of multiple 2D skeletons. The 2D skeleton interconnects were fabricated with a constant width of 0.5 mm and a thickness of 2 mm. Two types, auxetic and rectangle 2D skeleton structures, were designed by changing the internal angle (θ = 50° and 90°) of the joints. The vertical and horizontal external widths of the two 2D skeletons were fixed at 20.00 mm and 28.55 mm, respectively. Each 3D skeleton is made up of two types of 2D skeletons. **Figure 1a(i)** and **Figure 1b(i)** consist of a 3 cell – 2 cell – 3 cell pattern, while **Figure 1a(ii)** and **Figure 1b(ii)** consist of a 2 cell – 3 cell – 2 cell pattern.

(2) 3D skeletons consist of four 2D skeletons with the design of subfigures (i), and two 2D skeletons with the design of subfigures (ii). The top view layout of these 2D skeletons is shown schematically in **Figure 1a(iii)** and **Figure 1b(iii)**. For stable compression from one direction, this skeleton structure is symmetric in the xz plane and the yz plan. An image of the final structures are shown in **Figure 1a(iv)** and **Figure 1b(iv)**.

After printing, the skeletons were washed in deionized water to remove the support material and preserved in deionized water prior to composite fabrication.
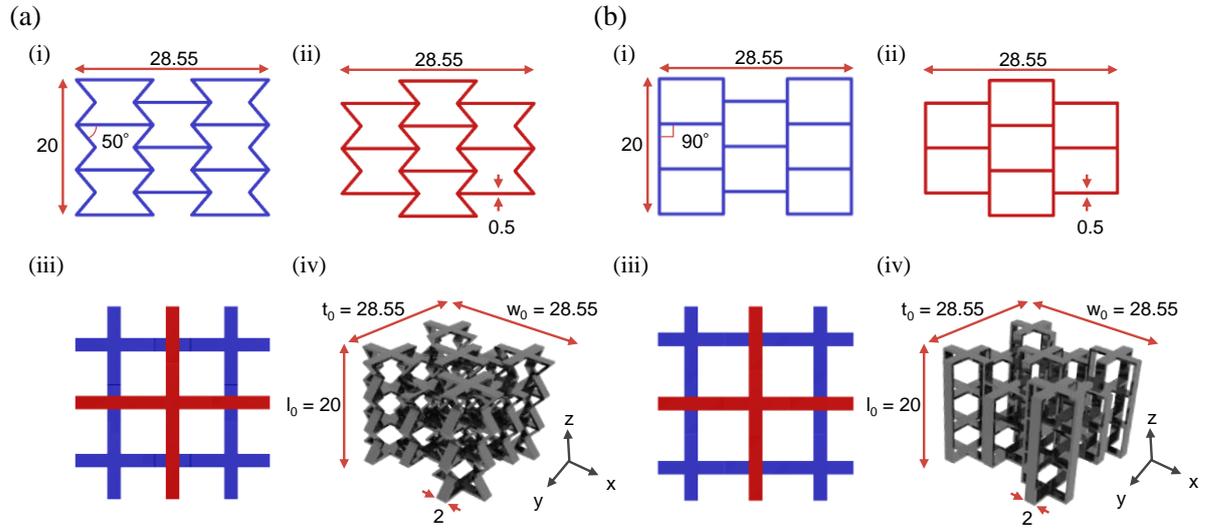
Figure 1. Dimensions of the skeleton structure (a) with auxetic and (b) rectangle. (i) and (ii) 2D skeleton structure of the skeleton. (iii) Top view of 3D skeleton structure. (iv) 3D skeleton structure. All dimensions are listed in mm.

6.2.4 Fabrication of Macro-DN hydrogel composites

3D skeletons were put in the plastic spacer ($l_0 \times w_0 \times t_0 = 20.00 \times 28.55 \times 28.55$ mm^3) and placed on a glass plate. Mold releasing films were attached to the inside of the plastic spacer to prevent chemical bonding between the P-DN hydrogel and the plastic spacer. The spacer and the mold releasing films were removed prior to sample testing. The particle hydrogel solution was poured into the plastic spacer in the reaction cell consisting of a pair of glass plates with a 20 mm silicone spacer. The AAm monomers were photopolymerized with the UV lamp for 8 h under argon atmosphere to obtain the hydrogel composite.

6.2.5 Compression tests

Uniaxial compression tests were performed on the composites, the pristine P-DN hydrogel (matrix), and the neat skeletons (reinforcement) using a tensile-compressive tester (Tensilon RTC-1310A, Orientec Co.). All samples were compressed along the length direction of the samples at a strain rate of 0.2 min^{-1} at room temperature. Strain, ε,

is defined as $\Delta l/l_0$, where l_0 and Δl are the length of the sample before and the length of the sample during compression, respectively. All compression experiments were recorded with a video camera (Panasonic VX985M).

6.2.6 Cycle tests

Cyclic loading/unloading compression tests for evaluating the energy dissipation ability was performed on the composites, the pristine matrix, and the neat skeletons on a tensile-compressive tester (Tensilon RTG-1310, A&D Company, Limited). All samples were compressed to strains of $\varepsilon_x = 0.05 - 0.5$ at a strain rate of 0.2 min^{-1}. Then, samples were returned to the initial strain immediately at the same strain rate. The energy dissipation was calculated from the hysteresis area, U_{hys} by:

$$U_{hys} = \int_{\varepsilon=0}^{\varepsilon=\varepsilon_x} (\sigma_{load} - \sigma_{unload})d\varepsilon$$

Where σ_{load} and σ_{unload} are the stress during loading and unloading, respectively.

6.2.7 90° Peeling tests

The peeling strength between the P-DN hydrogel and the plastic substrate that makes up the skeleton was measured using a standard 90° peeling test (ISO 8510–1) with a tensile-compressive tester (Instron 5965 type universal testing system). As part of the sample preparation process, half of the plastic substrate was masked with adhesive tape to prevent chemical bonding to the substrate, which creates the arm for the peeling test. Then, the P-DN hydrogels were coated onto the substrate, forming chemical bonds with the unmasked region of the substrate. A sample with a hydrogel layer coating thickness of 1.0 mm was cut into strips (with a width of 5 mm and a length of 100 mm) by using a laser cutter (PLS4.75, Universal Laser Systems). Samples were used either in the as-prepared state or after being immersed in deionized water for 14 days. The plastic substrate was fixed to one jig of the tester, and the hydrogel was clamped by the other jig. The samples were

tested according to a standard 90° peeling test with a constant peeling velocity of 100 mm/min. The peeling strength was determined by dividing the peeling force by the width of the sample.

6.3 Results & discussion

6.3.1 The mechanism by which the auxetic skeleton eliminates volume change mismatch in a Macro-DN hydrogel composite

The compressive elastic modulus of the bulk skeleton material is 411.68 ± 4.08 MPa and the modulus of the pristine matrix before and after swelling is 34.53 ± 0.15 kPa and 29.45 ± 0.07 kPa respectively, as determined by uniaxial compression. The mechanical properties of these two materials are significantly contrasting, with the skeleton possessing a modulus more than four orders of magnitude higher than the matrix. The skeletons are designed based on two types of geometries: auxetic and rectangle (as a control). Specific details can be seen in **Figure 1**. Although the rectangle skeleton has a smaller volume, V, than the auxetic skeleton, both the Young's modulus and the yield stress of the rectangle skeleton are higher, because the rectangle skeleton is rigid when compressed. On the other hand, the auxetic skeleton shows a high yield strain because the structure can deform when compressed. The matrix before and after swelling shows almost the same modulus values regardless of the volume being 2.41 ± 0.02 times different. The work of compression of the component materials were also almost the same (**Table 1**).

Table 1. Mechanical properties of the component materials as measured by uniaxial compression. These values were measured using a rectangular prism with $l_0 \times w_0 \times t_0 =$ $20.00 \times 28.55 \times 28.55$ mm^3. The matrix (as-prepared) was allowed to swell in deionized water.

Component	Structure (Angle, θ (°))	Young's modulus, E (kPa)	Yield Stress, σ_y (kPa)	Yield Strain, ε_y	Work of Compression, W (kPa) ($\varepsilon = 0 \sim 0.5$)	Volume, V (cm^3)
Skeleton	Auxetic (50)	172.4 ± 19.5	16.40 ± 1.42	0.192 ± 0.011	6.73 ± 0.80	1.24
Skeleton	Rectangle (90)	3373 ± 214	49.35 ± 0.64	0.025 ± 0.001	4.07 ± 0.06	1.01
Matrix (as-prepared)	-	34.53 ± 0.15	-	-	7.41 ± 0.34	16.30
Matrix (swelled)	-	29.45 ± 0.07	-	-	7.23 ± 0.11	39.35

Next, we immersed the hydrogel composites with auxetic and rectangle skeletons in deionized water and observed the swelling behavior of the hydrogel composites. **Figure 2** shows the sample appearance of the hydrogel composites and the component materials before and after swelling. Here, the samples are shown after 14 days of immersion in deionized water. The pristine matrix swelled greatly, but the two skeletons did not change at all when immersed in deionized water. Based on these results, when these materials are combined, the composites are expected to experience a large volume change mismatch. In this research, we qualitatively defined a material as exhibiting volume change mismatch when the skeleton structure is unexpectedly deformed or when the skeleton is fractured by the hydrogel matrix. In the rectangle hydrogel composite, we can confirm that the skeleton cannot withstand the swelling of the matrix and the skeleton partially fractures. However, the auxetic hydrogel composite could deform along with the swelling of the matrix without inducing volume change mismatch. To investigate the cause in detail, we measured the internal angle of the auxetic skeleton in the hydrogel

composite during the swelling process (**Figure 3b**). The values in **Figure 3b** were calculated from **Figure 3a**. From **Figure 3b**, over time, the internal angle of the auxetic composite increased as the matrix absorbed the water and as the hydrogel composite swelled. After 16,000 mins (about 11 days) of immersion in deionized water, the internal angle reached 90°, and at that point the internal angle hardly changed. Here, the swelling ratio, q, of the auxetic hydrogel composite and the pristine matrix after swelling are 2.25 $\pm\,0.01$ and 2.41 ± 0.02 respectively, with the q of the hydrogel composite being 1.07 times smaller than that of the matrix. Therefore, it is considered that the swelling of the hydrogel composite is only slightly suppressed by the structural elasticity of the skeleton, and at equilibrium the structural elasticity of the skeleton and the swelling pressure of the matrix becomes balanced. From these results, we successfully fabricated a highly deformable hydrogel composite by adopting an auxetic skeleton structure that does not experience volume change mismatch.
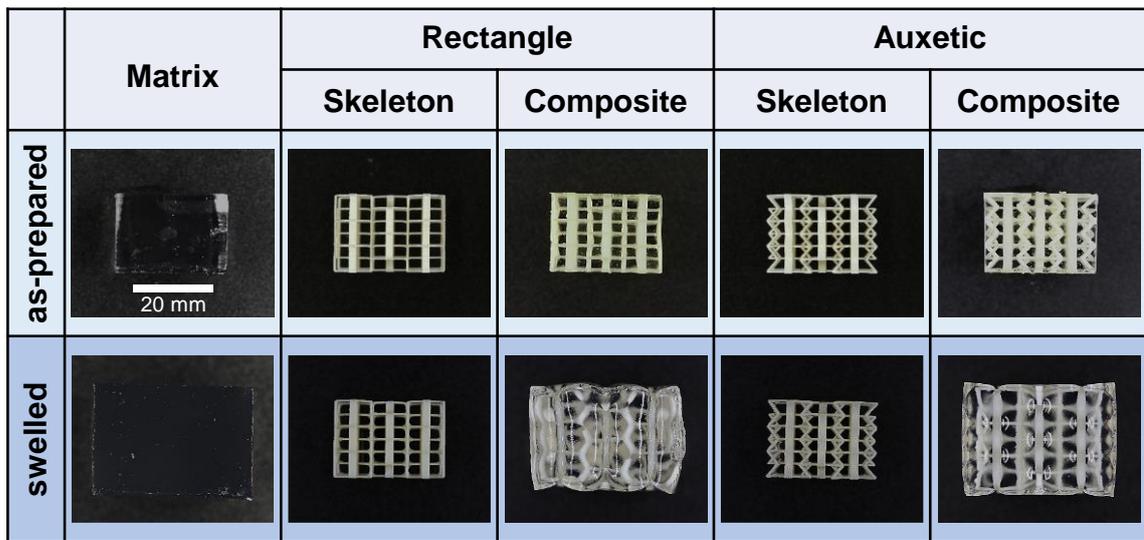
Figure 2. The appearance of the hydrogel composites and the component materials before and after swelling. The swollen samples are after 14 days of immersion in deionized water.

(a)

t = 0   t = 0   t = 500   t = 2000

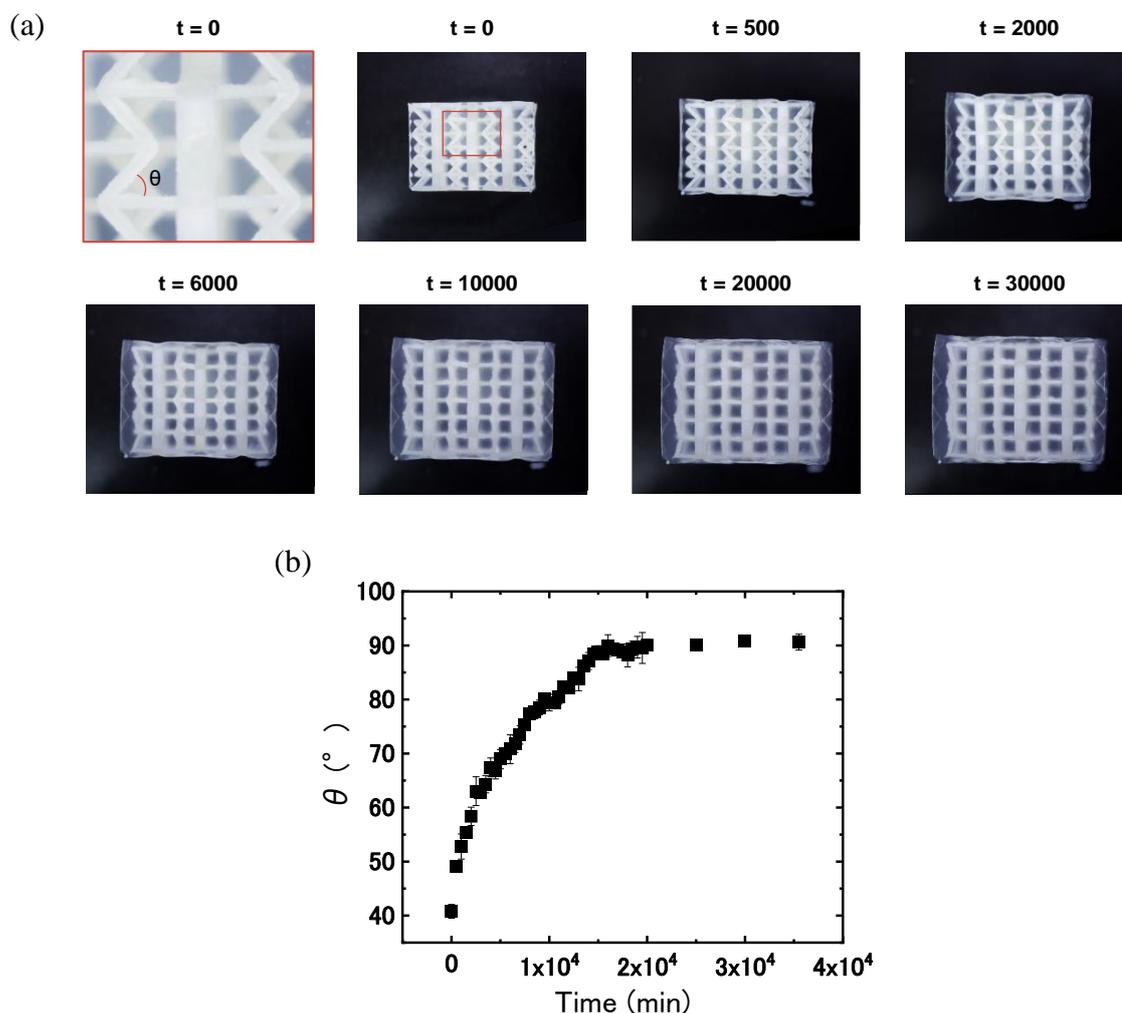t = 6000   t = 10000   t = 20000   t = 30000

(b)

Figure 3. Change in the internal angle of the auxetic hydrogel composite with swelling in deionized water. (a) Images of the auxetic hydrogel composite swelling with time. (b) Internal angle versus time curve for the auxetic hydrogel composite. The internal angle values, θ, were measured from images of the swelling behavior of the auxetic hydrogel composite, shown in (a).

To investigate the characteristics of the hydrogel composites, we measured and compared the mechanical properties of the pristine matrix, the rigid neat skeletons, and the hydrogel composites before and after swelling by uniaxial compression. Stress-strain curves of representative samples with rectangle and auxetic skeletons are shown in **Figure 4a**, and **Figure 4b**, respectively. The hydrogel composites before swelling exhibit excellent mechanical properties compared to the component materials. In detail, since the hydrogel composites before swelling are loaded not only on the skeleton but also on the

137

matrix during compression, it is considered that the yield stress synergistically increased in the low strain region until the skeleton fractures. Especially, the yield stress of the auxetic hydrogel composite is 5.01 times higher than that of the neat skeleton (**Figure 4c**). Here, the Poisson's ratio of the matrix is about 0.5, while the Poisson's ratio of the auxetic skeleton is negative. Therefore, the auxetic skeleton is deformed into a denser structure during compression, resulting in additional force being applied to the matrix. Based on this result, we conclude that the yield stress is improved due to the Poisson's ratio mismatch between the component materials. In the hydrogel composites after yielding, the hard and brittle skeletons began to rupture, but the soft and ductile matrix continued to support load in those regions. Due to this response, the hydrogel composites as a whole did not fracture immediately. When further compressed (after yielding), the skeleton fractured extensively like sacrificial bonds to avoid stress concentrations, and as a result, the stress of the hydrogel composites decreased. However, when further compressed, the stress of the hydrogel composites continued to rise.

The mechanical properties of the hydrogel composites after swelling changed significantly (**Figure 4c-e**). Since the rectangle skeleton in the swollen hydrogel composite fractured during the swelling process, no clear yield point was observed, and the stress-strain curve of the swollen rectangle hydrogel composite was almost the same as that of the matrix. Interestingly, the auxetic hydrogel composite after swelling exhibits a J-shaped curve in the low strain region. The hardening modulus (the rise in modulus seen with increasing strain) (**Figure 4b(ii)**) of the auxetic hydrogel composite after swelling is higher than the Young's modulus before swelling (**Figure 4f**). There are two possible reasons for this result. One is that the internal angle of the auxetic skeleton is larger, so the skeleton can support the force in the compression direction and harden like the rectangle skeleton. The other reason is that the auxetic skeleton contracts more when

138

compressed; that is, it deforms into a denser structure. In this case, the volume of the auxetic hydrogel composite increases due to swelling, which allows more stress to be applied to the matrix by the auxetic skeleton during compression. Except for the modulus, the mechanical properties of the auxetic hydrogel composite after swelling decrease due to the low density of the sample resulting from the swelling of the matrix. These results suggest that the auxetic hydrogel composite not only before swelling but also after swelling exhibits excellent mechanical properties, and the auxetic hydrogel composite after swelling exhibits unique functionalities not seen before swelling.
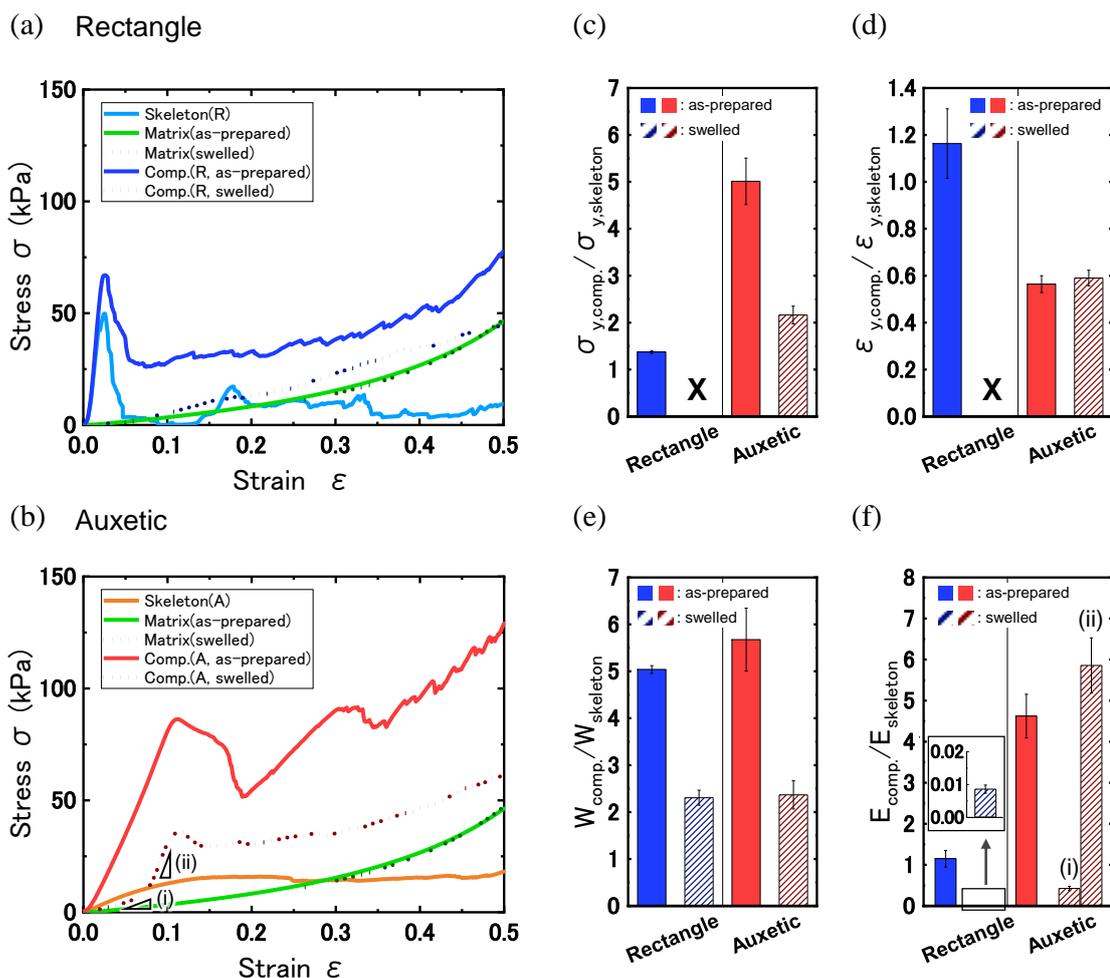
Figure 4. Mechanical response of the hydrogel composites and components by uniaxial compression test. (a) Stress versus strain curves for the rectangle composite, rectangle skeleton, and matrix before and after swelling. (b) Stress versus strain curves for the auxetic composite, auxetic skeleton, and matrix before and after swelling. The enhancement ratio of the composites for (c) yield stress, (d) yield strain, (e) work of compression, and (f) modulus. Light blue and orange show the skeletons with rectangle and auxetic structure, respectively. Dark blue and red represent the rectangle and auxetic composite, respectively. Green represents the matrix. Solid color represents the as-prepared state, and dashed or hashed markers represent the swollen samples. Error bars for all plots represent the standard deviation from n > 3 samples.

To further understand the mechanical properties of the auxetic hydrogel composite, we evaluated the energy dissipation ability by cyclic loading/unloading compression tests (**Figure 5**). For these cyclic tests, the strain was increased by 0.05, and the cycle tests were repeated a total of 10 times until the strain reached 0.5. First, the neat skeleton was tested (**Figure 5a**). Before the yield point (1st-3rd cycles), the neat skeleton did not dissipate much energy, but the amount of the energy dissipated increased with

140

increasing compression strain. Then, after the yield point, the neat skeleton fractured, dissipating some energy. Throughout this experiment, the neat skeleton possesses significant residual strain, demonstrating that the skeleton is somewhat inelastic. Next, the experiment was repeated for the pristine matrix (**Figure 5b**). The pristine matrix dissipated much less energy when compared to the neat skeleton, because the P-DN hydrogel is highly elastic. On the other hand, as seen in **Figure 5c**, the mechanical properties of the auxetic hydrogel composite improved significantly compared to the neat components. Before the yield point (1st and 2nd cycles), the auxetic hydrogel composite did not dissipate energy as well as the neat skeleton, but a significant amount of energy was dissipated after the yield point compared to the neat components (**Figure 5d**). This is because the skeleton inside the auxetic hydrogel composite acted as a sacrificial network. The amount of energy dissipated in the auxetic hydrogel composite is higher than the sum of the components. There are two possible reasons for this. One is due to the Poisson's ratio mismatch between the components mentioned above. This effect increases the strength, but if the skeleton inside the auxetic hydrogel composite does not fracture, energy dissipation will not occur. Then, when the skeleton fractures, stress relaxation occurs and energy is dissipated. The skeleton acts as a sacrificial network when the stress exceeds a certain level, so a certain amount of energy can be dissipated. The other reason is that the fracture of the interface between components causes energy dissipation. To investigate the strength of the interfacial interactions between the components, we evaluated the peeling strength by 90° peeling test (**Figure 6**). Regardless of whether the test was performed before or after swelling, the P-DN hydrogel always fractured first. Therefore, the peeling strength before and after swelling is greater than 66.02 ± 8.63 N/m and 15.17 ± 5.98 N/m, respectively. The matrix of the auxetic hydrogel composite did not fracture with compression of $\varepsilon = 0.5$. Based on these two points, it is

difficult to think that significant energy was dissipated due to the fracture of the interface interaction between the components. These results show that it is possible to create the hydrogel composites that can eliminate volume mismatch even if the components are firmly adhered. This opens the possibility for making a wide range of hydrogel composites, with diverse materials combinations.
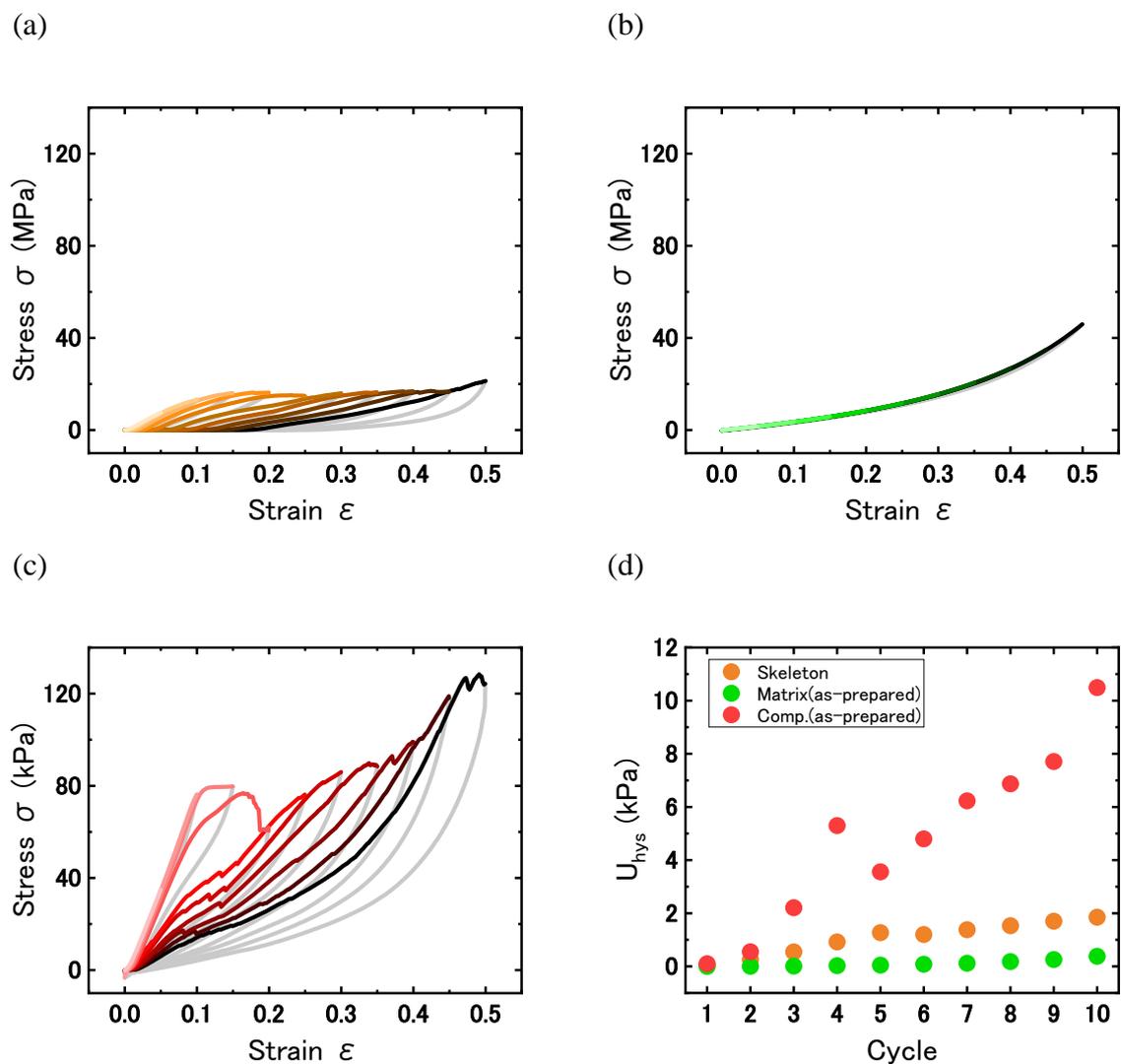
Figure 5. Cycle compression behavior of the auxetic hydrogel composite. Stress-strain curves of (a) a neat auxetic skeleton, (b) a neat matrix (P-DN hydrogel), and (c) the auxetic hydrogel composites. (d) Comparisons of energy dissipation, for the neat skeleton (orange), the neat matrix (green), and the auxetic hydrogel composite (red).

Figure 6. Internal interaction of components materials with Macro-DN hydrogel composite. Normalized force-displacement curves of the peeling test of P-DN hydrogel films with plastic basis for the reinforcement, for the as-prepared sample (bright red) and the swelled sample (dark red).

6.3.2 The influence of the auxetic hydrogel composite swelling ratio on the mechanical properties

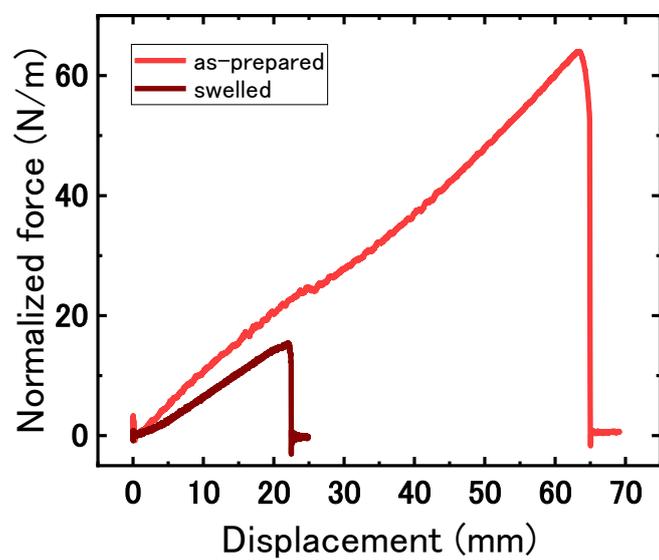In **Section 6.3.1**, we confirmed that the auxetic hydrogel composite after swelling has unique properties not found prior to swelling. Therefore, we investigated the effect of varying the swelling ratio on the mechanical properties of the auxetic hydrogel composite. To change the swelling ratio of the auxetic hydrogel composites, we controlled the osmotic pressure around the samples. The auxetic hydrogel composite was soaked in various polyethylene glycol (PEG) solutions (MW: 20,000) ranging from 2.5 wt% to 17.5 wt%. Then, we measured and compared the mechanical properties of the auxetic hydrogel composites after swelling by uniaxial compression in the same manner as in **Section 6.3.1**. **Figure 7a** shows the sample appearance and swelling ratio, q, of the auxetic hydrogel composites after swelling in the various PEG solutions. From **Figure 7a,b**, the q of the auxetic hydrogel composite and pristine matrix decreases as the concentration of the PEG solution increases. From this result, this auxetic hydrogel composite does not experience volume change mismatch between the components regardless of whether the composite swells to about 2.25 times or shrinks to 1.62 times compared to the original volume.

The q of the hydrogel composite with auxetic skeleton tends to be smaller than that of the pristine matrix immersed in the PEG solution of the same concentration. Therefore, we measured the amount of deformation in the length, l, the width, w, and thickness, t, dimension of each sample compared to the as prepared state (**Figure 7c**). Since the skeleton structure is symmetric in the xz plane and the yz plane, the amount of deformation in the t and w dimension is the same (**Figure 1**). In **Figure 7c,** the solid line represents the case of isotropic change, and the dashed line represents the change in geometry expected from the deformation of the auxetic structure. Since the skeleton is hard, the skeleton itself does not stretch. Therefore, the dashed line indicates the amount

144

that can be deformed by only changing the internal angle of the neat skeleton structure from 20° to 90°. The volume of this auxetic structure increases as the internal angle increases, and the volume can be increased up to a maximum internal angle of 90° (up to the point of x in **Figure 7c**). This estimation was determined by using finite element modeling in Autodesk Inventor. The pristine matrix undergoes an isotropic volume change, whereas the auxetic hydrogel composite undergoes an anisotropic volume change. Moreover, since this anisotropic volume change is close to the expected deformation of the neat auxetic skeleton, it is suggested that the magnitude of the volume change of the hydrogel composite is controlled by the matrix, but the relative swelling in each dimension of the hydrogel composite is controlled by the skeleton.
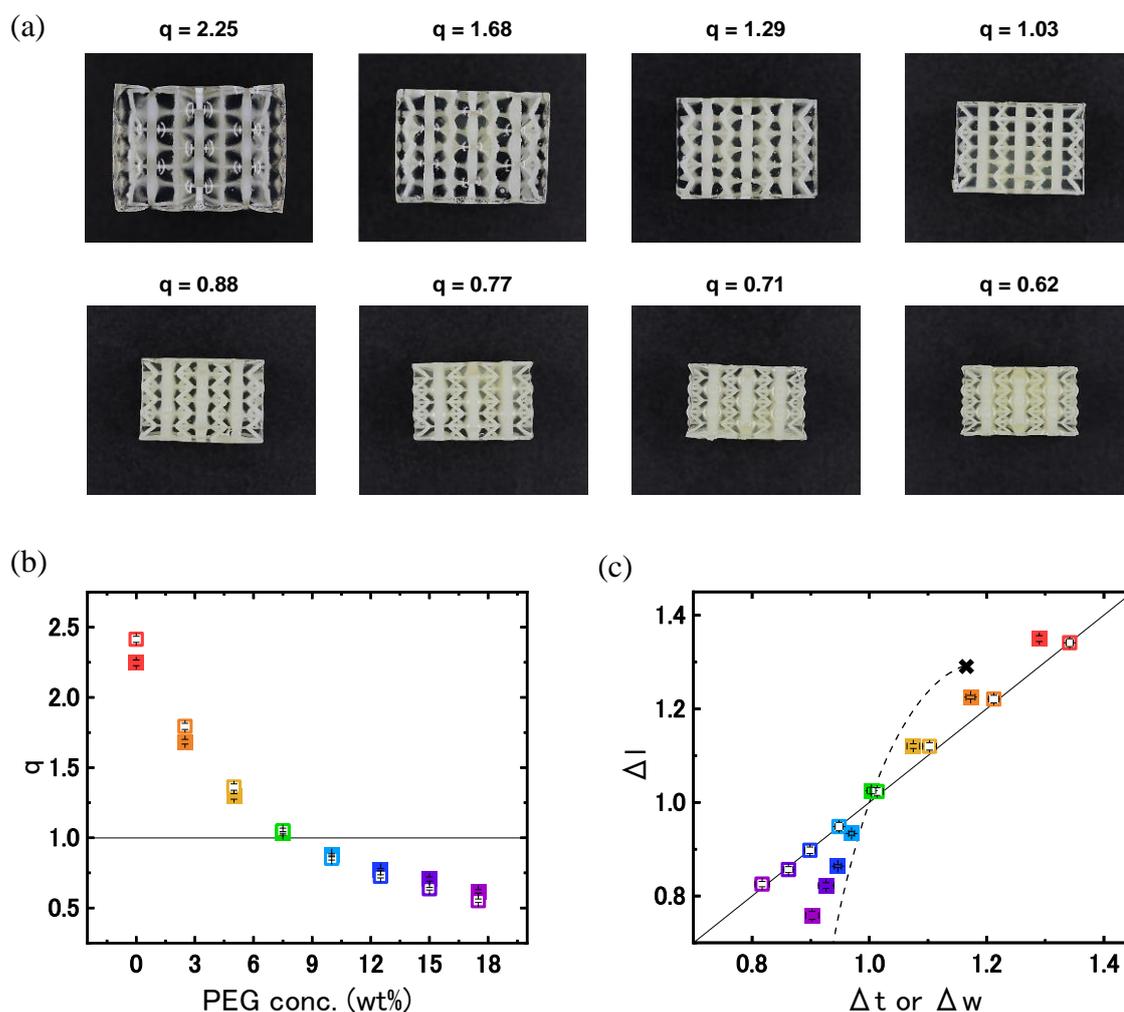
Figure 7. Swelling appearance of the auxetic hydrogel composites and the neat matrix in various PEG solutions. (a) Images of the auxetic hydrogel composites in various PEG solutions. (b) Swelling ratio versus PEG concentration for the auxetic hydrogel composites (filled symbol) and neat matrix (open symbol). (c) Change in length (Δl) versus change in thickness (Δt) or width (Δw) for the auxetic hydrogel composites (filled symbol) and neat matrix (open symbol).

Next, the stress-strain curves of the auxetic hydrogel composite immersed in various PEG solutions that result in swelling (**Figure 8a**) or deswelling (**Figure 8b**) are shown. As the q of the pristine matrix changes, the mechanical properties of the pristine matrix increase due to polymer density (**Table 2**). However, when the q of the auxetic hydrogel composite is changed, the mechanical properties changed significantly. In the swollen samples (**Figure 8a**), as the q of the auxetic hydrogel composite increased, the mechanical properties (hardening modulus, yield stress, and work of compression) decreased. On the

other hand, in the deswelled samples (**Figure 8b**), as the q of the auxetic hydrogel composite decreased, the mechanical properties increased. This trend occurs because the volume fraction of the skeleton in the auxetic hydrogel composite changes as the q of the auxetic hydrogel composite changes. Since the skeleton possesses a significantly higher Young's modulus than the hydrogel, the mechanical properties of the auxetic hydrogel composites with low skeleton volume fraction (high q) are lower than the auxetic hydrogel composites with high skeleton volume fraction (low q). Moreover, interestingly as the q of the auxetic hydrogel composite increased or decreased, J-shaped curves appeared. The mechanical response of these materials was similar, despite possessing vastly different swelling ratios, with the initially response being soft and suddenly hardening with increased strain. Our reasoning for this is as follows. In the high q sample, the matrix wants to swell to a large degree, but there is some resistance due to the relatively higher stiffness of the auxetic skeleton matrix, resulting in a slight decrease in the swelling of the composite compared to the pristine matrix. The skeleton is at rest exhibiting a slight compression force in this case, and therefore initial compression mainly results in deformation of the hydrogel matrix (**Figure 9a**). After the initial deformation of the swollen matrix, the skeleton also begins to deform along with the matrix, causing an increase in modulus, resulting in the J-shaped character. Conversely, in the low q samples, the matrix deswells, but again, the high stiffness of the skeleton prevents complete shrinking. This results in the skeleton being in an initial state of tension, while the matrix is in compression. When compressed, the skeleton resists deformation before the matrix (**Figure 9b**). After some initial deformation both the skeleton and matrix both deform equally, resulting in an increase in modulus, and the noted J-shape character. In the as-prepared sample with a q of 1, the skeleton and matrix are both under

no stress at rest. In this case, a J-shaped stress-strain curve is not observed because the skeleton and the matrix are both deformed equally during compression (**Figure 9c**).

Table 2. Mechanical properties of the neat matrices at various swelling ratios as measured by uniaxial compression tests. These values were measured from samples shaped as rectangular prisms ($l_0 \times w_0 \times t_0 = 20.00 \times 28.55 \times 28.55$ mm^3). All matrices were used after swelling of the matrix in deionized water except as-prepared sample.

| Component	PEG concentration, (wt%)	Swelling ratio, q	Young's modulus, E (kPa)	Work of compression, W (kPa) ($\varepsilon = 0 \sim 0.5$)	Volume, V (cm^3)
Matrix	(as-prepared)	1.00 ± 0.00	34.53 ± 0.15	7.41 ± 0.11	16.30
Matrix	0.0	2.41 ± 0.02	29.45 ± 0.07	7.23 ± 0.11	39.35
Matrix	2.5	1.79 ± 0.02	28.70 ± 1.70	6.73 ± 0.65	29.24
Matrix	5.0	1.36 ± 0.02	30.00 ± 0.42	6.75 ± 0.35	22.19
Matrix	7.5	1.05 ± 0.02	32.23 ± 0.06	7.35 ± 0.08	17.12
Matrix	10.0	0.85 ± 0.01	34.97 ± 0.65	7.60 ± 0.02	13.90
Matrix	12.5	0.72 ± 0.01	37.67 ± 1.98	8.15 ± 0.16	11.82
Matrix	15.0	0.64 ± 0.01	41.50 ± 0.44	8.95 ± 0.19	10.37
Matrix	17.5	0.55 ± 0.01	47.33 ± 2.45	9.19 ± 0.62	8.99
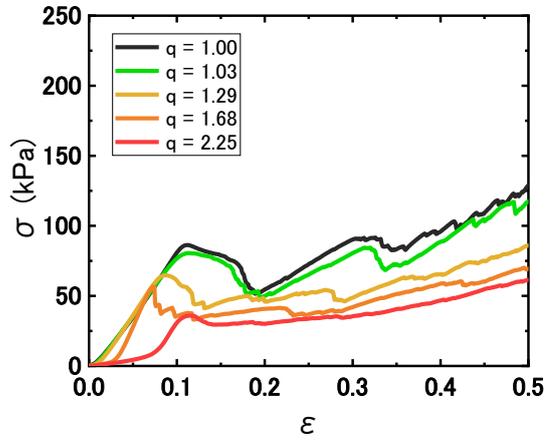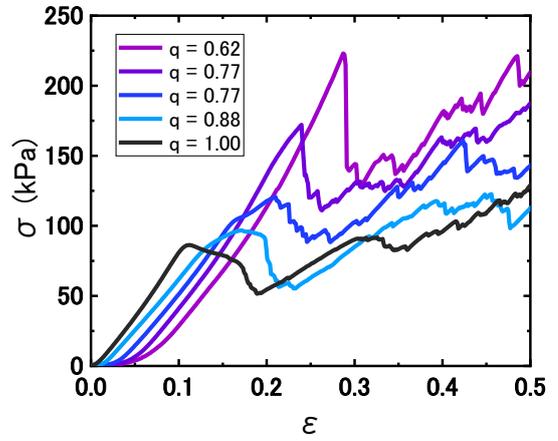
Figure 8. Mechanical response of the auxetic hydrogel composites with various swelling ratio by uniaxial compression. (a) Stress-strain curves for the auxetic hydrogel composites with swelling ratios equal to or greater than 1. (b) Stress-strain curves for the auxetic hydrogel composites with swelling ratios equal to or less than 1.
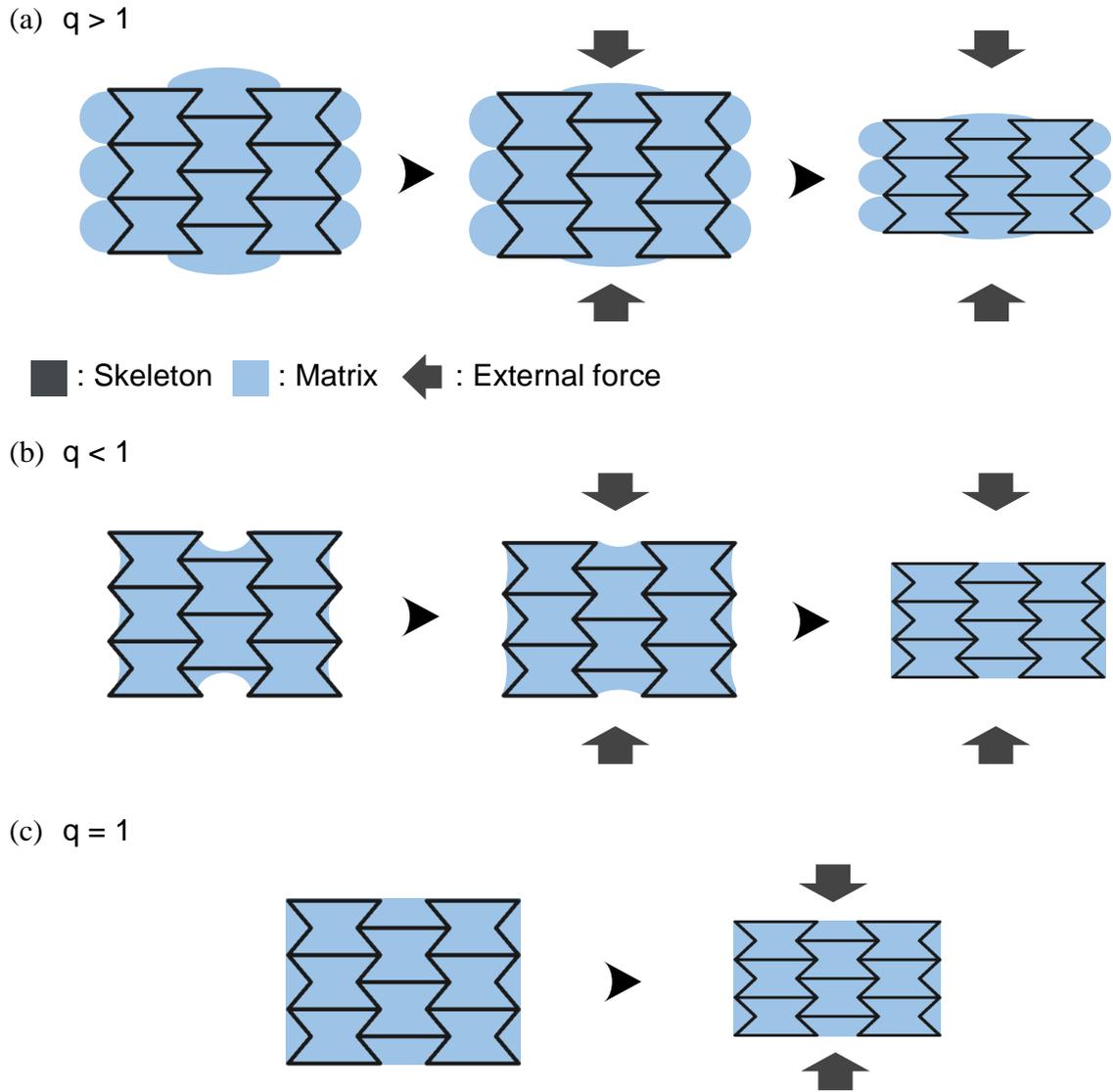
Figure 9. Compression behaviors that create J-shaped curves in various *q*. Compression behaviors (a) in a high *q* sample, (b) in a low *q* sample, (c) in an as-prepared sample.

To more clearly see the effect of q on the mechanical properties of the auxetic hydrogel composites, we calculate the enhancement ratio (**Figure 10a-d**). The enhancement ratio for yield stress ($\sigma_{y,enh}$), yield strain ($\varepsilon_{y,enh}$), work of compression up to a strain of 0.5 (W_{enh}), and hardening modulus (area where the elastic modulus is suddenly high in the J-shaped curve) ($E_{h,enh}$) are calculated as follows:

$$\sigma_{y,enh} = \frac{\sigma_{y,composite}}{\sigma_{y,composite(q=1)}}$$

$$\varepsilon_{y,enh} = \frac{\varepsilon_{y,composite}}{\varepsilon_{y,composite(q=1)}}$$

$$W_{enh} = \frac{W_{composite}}{W_{composite(q=1)}}$$

$$E_{h,enh} = \frac{E_{h,composite}}{E_{h,composite(q=1)}}$$

Where the subscript "composite" refers to the equilibrium composite, and the subscript "composite ($q = 1$)" refers to the as-prepared sample. As we can see in **Figure 10,** the trend changed significantly with $q = 1$ as the boundary. This is because of the anisotropic volume change of the auxetic hydrogel composites. In other words, when $q < 1$, the structure of composites had a larger cross-sectional area and smaller length than that of the isotropic sample, making it easier to compress. On the contrary, when $q > 1$, compared to the isotropic sample, the structure of composites had almost no change in length, but the cross-sectional area was smaller, resulting in a structure that was unbalanced and unfavorable for compression (**Figure 7c**). In **Figure 10a**, the yield stress of the deswelled auxetic hydrogel composites was enhanced by up to 2.70x. For yield strain, the auxetic hydrogel composite showed an enhancement of up to 2.63x (except for $q = 2.25$), however we see the enhancement ratio decreases as the swelling ratio increases (**Figure 10b**). The work of compression shows the same tendency as the yield stress, and the auxetic hydrogel composite work of compression is enhanced by up to 1.56x (**Figure 10c**), when compared to the as-prepared auxetic hydrogel composite. According to **Figure 10d**, the modulus of swollen and deswelled auxetic hydrogel composites was enhanced by up to 1.27x and 1.04x, respectively (except for $q = 2.25$). Furthermore, it was confirmed that as the swelling ratios deviate farther from $q = 1$ are, the better the

modulus of the auxetic hydrogel composite, in either the swelling or deswelling direction. Here, the largest swelling sample ($q = 2.25$) often did not match the other q trends. From **Figure 7c**, it can be seen that the hydrogel swells beyond the maximum volume of the skeleton (the point of x), which may cause the skeleton to exert more pressure inside the composite to suppress the swelling of the hydrogel. This can be seen in the images by the composite possessing a slightly rounded exterior.
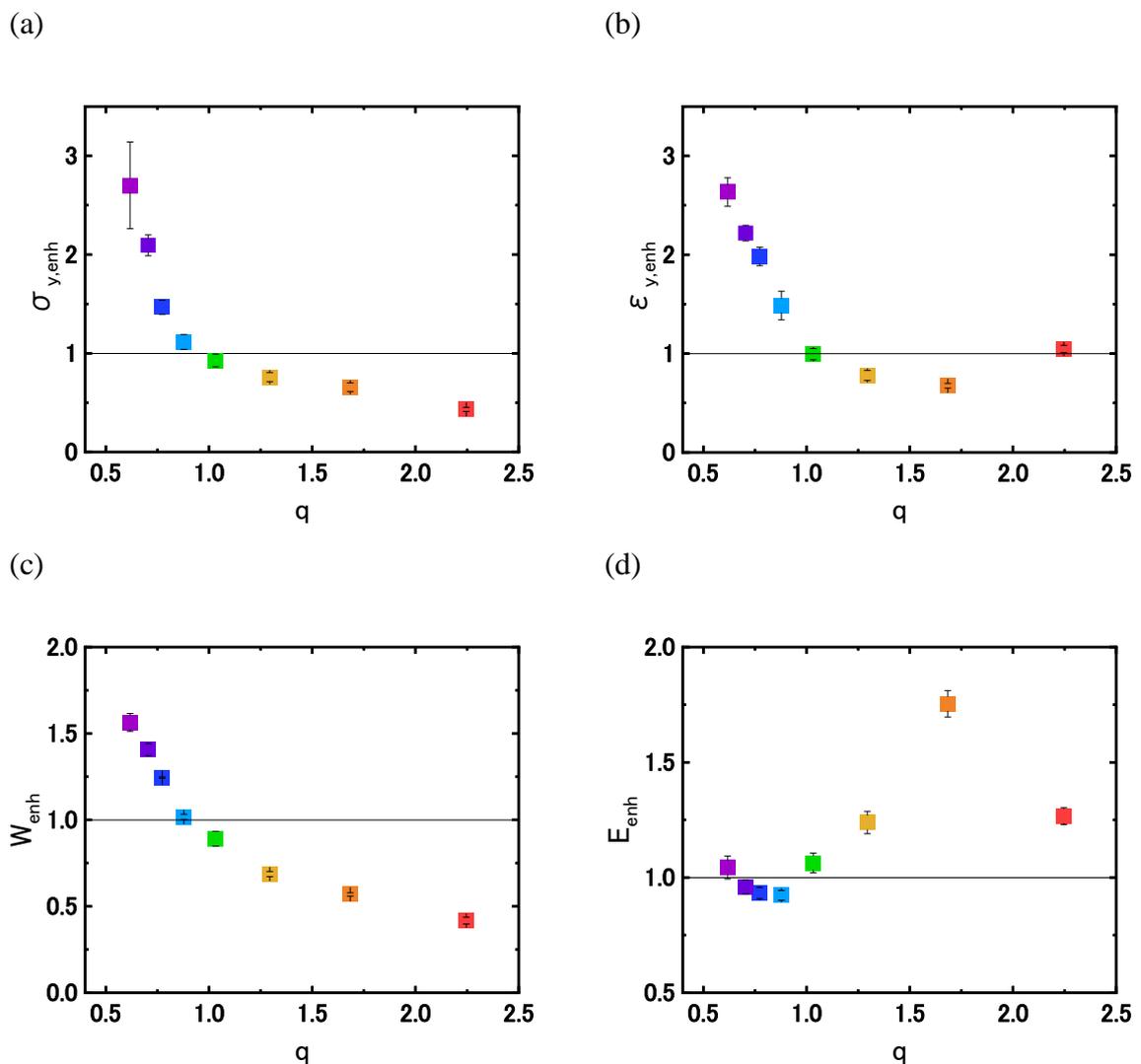
Figure 10. Effect of the swelling ratio of the auxetic hydrogel composite on the enhancement ratio of the mechanical properties. Enhancement ratio versus swelling ratio for (a) yield stress, (b) yield strain, (c) work of compression, and (d) elastic modulus. Yield stress, yield strain, work of compression, and elastic modulus are normalized by the as-prepared auxetic hydrogel component. Error bars for all plots represent the standard deviation from n > 3 samples.

To better understand these enhancement mechanisms, we normalized the auxetic hydrogel composites by their swelling ratio after reaching equilibrium in the PEG solutions. Here, q and $\varphi_{skeleton}$ are inversely proportional ($q \propto^{-1} \varphi_{skeleton}$). Taking the swelling ratio into account, we estimated the efficiency ratio (**Figure 11a-d**) of the auxetic hydrogel composites for the yield stress ($\sigma_{y,eff.}$), yield strain ($\varepsilon_{y,eff}$), work of compression ($W_{eff.}$), and elastic modulus ($E_{h,eff}$). These terms are calculated by:

$$\sigma_{y,eff} = \sigma_{y,enh} \times q_{composite}$$

$$\varepsilon_{y,eff} = \varepsilon_{y,enh} \times q_{composite}$$

$$W_{eff} = W_{enh} \times q_{composite}$$

$$E_{h,eff} = E_{h,enh} \times q_{composite}$$

Where $q_{composite}$ represents the swelling ratio of the auxetic hydrogel composite in various PEG solutions. In **Figure 11a**, except for $q = 2.25$, the efficiency of the yield stress increases by swelling or deswelling as the swelling ratio deviates from $q = 1$. In the auxetic hydrogel composites with $q > 1$, the skeleton structure internal angle approaches 90 degrees and the skeleton becomes harder to deform with compression. However, with the largest amount of swelling (q = 2.25), twisting and fracture is likely to occur before it can be properly compressed. In the region where $q > 1$, the yield strain increases, probably due to the onset of J-shaped character from matrix swelling (**Figure 11b, Figure 8b**). On the other hand, in the auxetic hydrogel composite with $q < 1$, yield stress increases rapidly. This is because when the matrix shrinks, the skeleton internal angle is highly acute and therefore the composite can be highly compressed before the skeleton fractures. Furthermore, when this auxetic hydrogel composite deswells anisotropically, it is more stable and easier to be further compressed because the compression surface is larger than

that of the isotropic sample (**Figure 7c**). In fact, even considering the J-shape curves, in the region where $q < 1$, the yield strain significantly increases (**Figure 11b**).

Next, the work of compression decreased as the q of the auxetic hydrogel composite increased (**Figure 10c**). This is because that the volume fraction of the skeleton, $\varphi_{skeleton}$, decreased as the q increased. To confirm this, we normalized the measured values for each swelling ratio of the auxetic hydrogel composite ($q \propto^{-1} \varphi_{skeleton}$). Then, all auxetic hydrogel composites showed similar values (**Figure 11c**). In addition, from the cycle test results (**Figure 5d**), the skeleton deformed without fracture until before the yield point, so the auxetic hydrogel composite did not dissipate significant energy. On the other hand, when the yield point was exceeded, the skeleton fractured. Then the auxetic hydrogel composite had large hysteresis and dissipated a large amount of energy. From these results, the work of compression of the auxetic hydrogel composite was due to the skeleton fracture as a sacrificial network, so the work of compression increased as the volume fraction of skeleton in the auxetic hydrogel composite increased (**Figure 10c**).

Finally, the elastic modulus improved as the q of the auxetic hydrogel composite decreased or increased, deviating from $q = 1$ (**Figure 10d**). This is because the density of the auxetic hydrogel composite or the volume fraction of the skeleton increased as the q of the auxetic hydrogel composite decreased. In other words, the elastic modulus improved in the deswelling region. To confirm this, we normalized the measured values for each swelling ratio ($q \propto^{-1} \varphi_{skeleton}$) (**Figure 11d**). Then, the values in the deswelling region show a decreasing tendency. However, even after normalization, the elastic modulus improved as the auxetic hydrogel composite swelled. There are two reasons for this phenomenon. One is that the internal angle of the skeleton structure increased (changed from auxetic to rectangle) as the auxetic hydrogel composite swelled. The extended skeleton is able to support additional force in the compression direction. The

second reason is that the volume of the matrix in the skeleton increased, so the matrix could support more load relative to the skeleton during compression. Skeleton structures are able introduce highly anisotropic deformation in hydrogel composites, and in future work it may be possible to impart functional properties due to the anisotropic swelling.
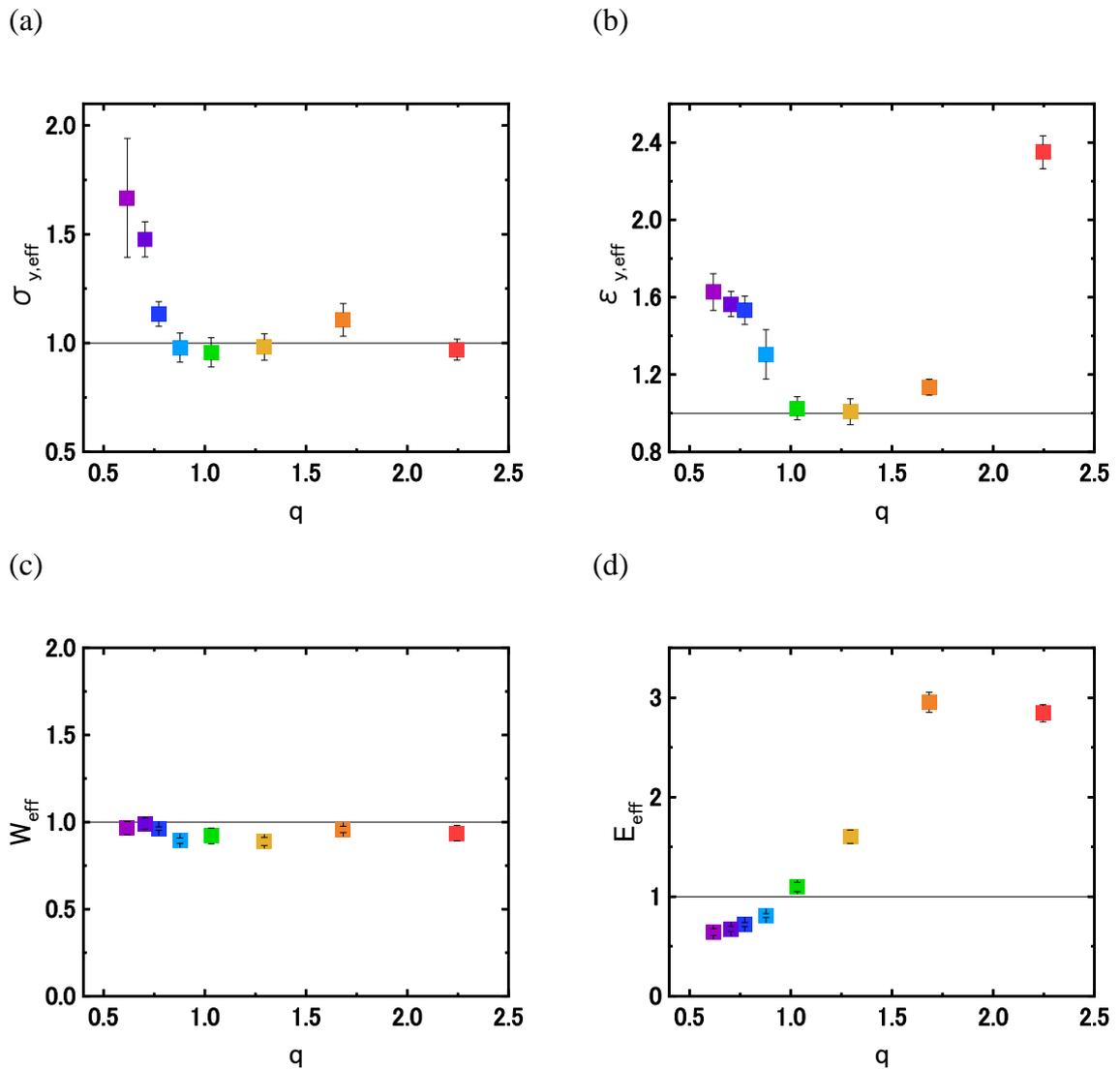
Figure 11. Effect of the swelling ratio of the auxetic hydrogel composite on the efficiency ratio of the auxetic hydrogel composite mechanical properties. Efficiency ratio versus swelling ratio for (a) yield stress, (b) yield strain, (c) work of compression, and (d) hardening modulus. Yield stress, yield strain, work of compression, and hardening modulus are normalized by the swelling ratio of the auxetic hydrogel component. Error bars for all plots represent the standard deviation from n > 3 samples.

6.4 Conclusions

In conclusion, we succeeded in creating novel hydrogel composites based on a 3D auxetic skeleton and a P-DN hydrogel matrix. This auxetic hydrogel composite can eliminate the volume change mismatch between component materials caused by the swelling/deswelling of the hydrogel matrix over a wide swelling ratio range, even though strong interactions exist between the components. The toughness of the auxetic hydrogel composite is significantly increased by 5.7x compared to the neat skeleton as the skeleton acts as a sacrificial network, like the double network effect. Furthermore, utilizing the unique negative Poisson's ratio exhibited by auxetic materials within the macroscopic reinforcement, the Young's modulus and yield stress of the auxetic hydrogel composites are also dramatically increased by 4.6x and 5.0x, respectively compared to the neat skeleton. This is because the mismatch of the Poisson's ratio between reinforcing phase and matrix induces an internal conflict, leading to high deformation of the matrix. Interestingly, this auxetic hydrogel composite shows skeleton-dependent anisotropic swelling characteristics and J-shaped curves by swelling or deswelling. Moreover, the auxetic hydrogel composite exhibited 1.7x higher hardening modulus by swelling and 2.7x higher strength and 1.6x higher toughness by deswelling compared to the as-prepared sample. This novel method of creating soft/hard hydrogel composites by adopting auxetic reinforcement could be useful towards creating hydrogel composites that have high mechanical properties and multiple functionalities, and we believe that this research will find use in the fields of soft robotics, wearable electronics, and biocompatible functional materials.

CHAPTER 7

Summary of the dissertation

In this dissertation, we have focused on macro-scale DN materials, which are derived from molecular-scale DN hydrogels. In this system, a combination of hard phase as reinforcement and soft matrix plays an important role in the emergence of new and useful functions. Through a simple yet versatile design concept of utilizing a macro-scale skeleton as a hard phase by 3D printing, we successfully obtained knowledge on unexplained phenomena in DN materials, established a new toughening mechanism for Macro-DN materials, and developed general method for creating Macro-DN hydrogel composites. The following conclusions are given:

1) Elucidation of unexplained phenomena in DN materials using simple Macro-DN structures

Based on the essence of DN hydrogels, Macro-DN materials that contain a 3D printed hard phase as a sacrificial network embedded within a silicone rubber stretchable matrix have been developed as a simple model for observing the fracture behavior of DN structures. In **Chapter 3,** we clarified the conditions where the toughening of materials based on the DN principle will be expressed at the macro-scale. The mechanical properties of the skeleton were controlled by adjusting the thickness of the columns of the hard skeleton that act as sacrificial bonds. As a result, the expression condition of the DN principle was controlled by the fracture strength ratio of the hard and soft phases. When the fracture strength ratio is less than 1, the Macro-DN material is tough, and when the fracture strength ratio is greater than 1, it becomes brittle. Moreover, it was also shown that increasing the number of sections in the skeleton based on topological interlocking increased the number of fracture events, increasing energy dissipation and improving the toughness of the Macro-DN material.

In **Chapter 4,** we demonstrated the mechanism by which the DN structure is able to ignore defects in their constituent materials and exhibit excellent potential mechanical properties. Defects were introduced into the hard and soft phases of Macro-DN materials to investigate how the heterogeneity of the two phases in the DN structure affects the mechanical properties of the DN materials. The results show that DN structures that inherently contain defects in both phases are capable of exhibiting mechanical properties similar to defect-free materials. These results shed light on why DN hydrogels are so tough: cracks are blunted because defects in the 1st network are supported by locally high concentrations of 2nd network, and 2nd network defects avoid deformation due to high 1st network density. The experimental results agree well with a simple analytical model that was established.

2) Establishment of a new toughening mechanism for Macro-DN materials

In **Chapter 5,** we proposed a novel toughening mechanism for Macro-DN materials utilizing a sacrificial network that possesses a functional structure such as an auxetic or a honeycomb design. These designs cause the hard phase to deform with a Poisson's ratio that deviates from the normal value of 0.5 seen by incompressible materials. When a hard phase with functional structure was combined with a soft phase, the hard phase not only fractured as sacrificial bonds but also synergistically improved the mechanical properties of the Macro-DN material by inducing large deformation of the soft phase. The soft phase attempts to resist the deformation that occurs due to the difference in Poisson's ratio between the hard and soft phases. Furthermore, this effect was found to increase with the difference in Poisson's ratio between the component materials, indicating that both the auxetic (negative Poisson's ratio mismatch) and honeycomb (positive Poisson's ratio mismatch) can contribute to the enhancement of the mechanical properties of Macro-DN materials.

3) Development of Macro-DN hydrogel composites

In **Chapter 6,** we developed a new method for creating highly deformable hydrogel composites with macro-scale hard phase reinforcement. By combining the auxetic structure that shows a negative Poisson's ratio for the hard phase with a particle-based double-network hydrogel matrix, we successfully eliminated the volume change mismatch between components. The Macro-DN hydrogel composite with auxetic skeleton overcomes the volume change mismatch between the constituent materials that is usually exhibited by hydrogel composites by flexibly deforming the hard phase according to the swelling or deswelling of the hydrogel matrix caused changes in environmental conditions. Furthermore, this Macro-DN hydrogel composite showed excellent mechanical properties due to the DN principle and Poisson's ratio mismatch effect described above. In addition to the mechanical properties, the Macro-DN hydrogel composites also exhibited unique functional properties such as J-shaped stress-strain curves and anisotropic swelling and deswelling due to the hard phase. This composite method enables the use of a wide range of hydrogels as the soft phase of Macro-DN materials and provides insight into the expression of new functional properties due to the hard phase.

There are still many unexplored phenomena remaining regarding DN hydrogels. In addition to that, research on Macro-DN materials has just begun. In this dissertation the design guidelines for utilizing a skeleton as the hard phase for Macro-DN materials has been proven. This technique is effective, not only as a method to create new materials that can be used today, but also as a simple model to understand unexplained phenomena in DN materials in general. The Macro-DN concept is not specific but general, and it can be applied to a variety of soft materials for toughening and imparting new functions. We

believe that this research will have a domino effect in the fields of biocompatible functional materials, soft robotics and wearable electronics.

References

1. Connections, M. REVIEW Structural Biological Materials: Critical Mechanics-Materials Connections. 773–780 (2013).

2. Weiner, S. & Wagner, H. D. The material bone: Structure-mechanical function relations. *Annu. Rev. Mater. Sci.* **28**, 271–298 (1998).

3. Ritchie, R. O. Armoured oyster shells. *Nat. Mater.* **13**, 435–437 (2014).

4. Wegst, U. G. K., Bai, H., Saiz, E., Tomsia, A. P. & Ritchie, R. O. Bioinspired structural materials. *Nat. Mater.* **14**, 23–36 (2015).

5. Gong, J. P., Katsuyama, Y., Kurokawa, T. & Osada, Y. Double-network hydrogels with extremely high mechanical strength. *Adv. Mater.* **15**, 1155–1158 (2003).

6. Gong, J. P. Why are double network hydrogels so tough? *Soft Matter* **6**, 2583–2590 (2010).

7. Nakajima, T., Kurokawa, T., Ahmed, S., Wu, W. L. & Gong, J. P. Characterization of internal fracture process of double network hydrogels under uniaxial elongation. *Soft Matter* **9**, 1955–1966 (2013).

8. Ducrot, E., Montes, H. & Creton, C. Structure of Tough Multiple Network Elastomers by Small Angle Neutron Scattering. *Macromolecules* **48**, 7945–7952 (2015).

9. Murai, J. *et al.* Tough double network elastomers reinforced by the amorphous cellulose network. *Polymer (Guildf).* **178**, 121686 (2019).

10.   Matsuda, T., Nakajima, T. & Gong, J. P. Fabrication of Tough and Stretchable Hybrid Double-Network Elastomers Using Ionic Dissociation of Polyelectrolyte in Nonaqueous Media. *Chem. Mater.* **31**, 3766–3776 (2019).

11.   Feng, X. *et al.* A highly stretchable double-network composite. *Soft Matter* **12**, 8999–9006 (2016).

12.   Shabahang, S. *et al.* Controlled fragmentation of multimaterial fibres and films via polymer cold-drawing. *Nature* **534**, 529–533 (2016).

13.   Cooper, C. B. *et al.* Toughening stretchable fibers via serial fracturing of a metallic core. *Sci. Adv.* **5**, 1–9 (2019).

14.   Feng, X., Ma, Z., MacArthur, J. V. & Hong, W. Magnetic double-network composite capable of large recoverable deformation. *Soft Matter* **17**, 554–562 (2021).

15.   Zhu, F. *et al.* 3D-Printed Ultratough Hydrogel Structures with Titin-like Domains. *ACS Appl. Mater. Interfaces* **9**, 11363–11367 (2017).

16.   Takahashi, R. *et al.* Creating Stiff, Tough, and Functional Hydrogel Composites with Low-Melting-Point Alloys. *Adv. Mater.* **30**, 1–7 (2018).

17.   Tominaga, T. *et al.* The molecular origin of enhanced toughness in double-network hydrogels: A neutron scattering study. *Polymer (Guildf).* **48**, 7449–7454 (2007).

18.   Fukao, K. *et al.* Effect of Relative Strength of Two Networks on the Internal Fracture Process of Double Network Hydrogels As Revealed by in Situ Small-Angle X-ray Scattering. *Macromolecules* **53**, 1154–1163 (2020).

19. Higuchi, Y., Saito, K., Sakai, T., Gong, J. P. & Kubo, M. Fracture Process of Double-Network Gels by Coarse-Grained Molecular Dynamics Simulation. *Macromolecules* **51**, 3075–3087 (2018).

20. Jeffery, A. K., Blunn, G. W., Archer, C. W. & Bentley, G. Three-dimensional collagen architecture in bovine articular cartilage. *J. Bone Jt. Surg. - Ser. B* **73**, 795–801 (1991).

21. Sophia Fox, A. J., Bedi, A. & Rodeo, S. A. The basic science of articular cartilage: Structure, composition, and function. *Sports Health* **1**, 461–468 (2009).

22. Amini, A., Khavari, A., Barthelat, F. & Ehrlicher, A. J. E ~1000. **1234**, 1229–1234 (2021).

23. Yamauchi, Y., Tenjimbayashi, M., Samitsu, S. & Naito, M. Durable and Flexible Superhydrophobic Materials: Abrasion/Scratching/Slicing/Droplet Impacting/Bending/Twisting-Tolerant Composite with Porcupinefish-Like Structure. *ACS Appl. Mater. Interfaces* **11**, 32381–32389 (2019).

24. Gong, J. P., Katsuyama, Y., Kurokawa, T. & Osada, Y. Double-Network Hydrogels with Extremely High Mechanical Strength. *Adv. Mater.* **15**, 1155–1158 (2003).

25. Tanaka, Y. *et al.* Determination of fracture energy of high strength double network hydrogels. *J. Phys. Chem. B* **109**, 11559–11562 (2005).

26. Nakajima, T. *et al.* True chemical structure of double network hydrogels. *Macromolecules* **42**, 2184–2189 (2009).

27. Fantner, G. E. *et al.* Sacrificial bonds and hidden length dissipate energy as

mineralized fibrils separate during bone fracture. *Nat. Mater.* **4**, 612–616 (2005).

28. Nakajima, T. *et al.* A universal molecular stent method to toughen any hydrogels based on double network concept. *Adv. Funct. Mater.* **22**, 4426–4432 (2012).

29. Sun, J.-Y. *et al.* Highly stretchable and tough hydrogels. *Nature* **489**, 133–6 (2012).

30. Sun, T. L. *et al.* Physical hydrogels composed of polyampholytes demonstrate high toughness and viscoelasticity. *Nat. Mater.* **12**, 932–937 (2013).

31. Zhang, H. J. *et al.* Tough Physical Double-Network Hydrogels Based on Amphiphilic Triblock Copolymers. *Adv. Mater.* **28**, 4884–4890 (2016).

32. Fukao, K., Nonoyama, T., Gong, J. P., Tanaka, K. & Kiyama, R. Hydrogels toughened by biominerals providing energy-dissipative sacrificial bonds. *J. Mater. Chem. B* **8**, 5184–5188 (2020).

33. Kamio, E., Yasui, T., Iida, Y., Gong, J. P. & Matsuyama, H. Inorganic/Organic Double-Network Gels Containing Ionic Liquids. *Adv. Mater.* **29**, 1–8 (2017).

34. Arafune, H. *et al.* Highly Robust and Low Frictional Double-Network Ion Gel. *Adv. Mater. Interfaces* **4**, (2017).

35. Ducrot, E., Chen, Y., Bulters, M., Sijbesma, R. P. & Creton, C. Toughening elastomers with sacrificial bonds and watching them break. *Science (80-.).* **344**, 186–9 (2014).

36. Ahmed, S., Nakajima, T., Kurokawa, T., Anamul Haque, M. & Gong, J. P. Brittle-ductile transition of double network hydrogels: Mechanical balance of two networks as the key factor. *Polymer (Guildf).* **55**, 914–923 (2014).

37. Matsuda, T. *et al.* Yielding Criteria of Double Network Hydrogels. *Macromolecules* **49**, 1865–1872 (2016).

38. King, D. R. *et al.* Extremely tough composites from fabric reinforced polyampholyte hydrogels. *Mater. Horizons* **2**, 584–591 (2015).

39. Huang, Y. *et al.* Energy-Dissipative Matrices Enable Synergistic Toughening in Fiber Reinforced Soft Composites. *Adv. Funct. Mater.* **27**, 1–10 (2017).

40. Cui, W. *et al.* Fiber-Reinforced Viscoelastomers Show Extraordinary Crack Resistance That Exceeds Metals. *Adv. Mater.* **32**, 1–9 (2020).

41. Cui, W. *et al.* Tiny yet tough: Maximizing the toughness of fiber-reinforced soft composites in the absence of a fiber-fracture mechanism. *Matter* **4**, 3646–3661 (2021).

42. Takahashi, R. *et al.* Creating Stiff, Tough, and Functional Hydrogel Composites with Low-Melting-Point Alloys. *Adv. Mater.* **30**, 1706885 (2018).

43. Tauber, J., Dussi, S. & van der Gucht, J. Microscopic insights into the failure of elastic double networks. *Phys. Rev. Mater.* **4**, 063603 (2020).

44. Du, X., Zhou, J., Shi, J. & Xu, B. Supramolecular Hydrogelators and Hydrogels: From Soft Matter to Molecular Biomaterials. *Chem. Rev.* **115**, 13165–13307 (2015).

45. Ramakrishna, S. & Mayer, J. Biomedical applications of polymer-composite materials: a review. *Compos. Sci. Technol.* **61**, 1189–1224 (2001).

46. Maeda, S., Hara, Y., Sakai, T., Yoshida, R. & Hashimoto, S. Self-walking gel. *Adv. Mater.* **19**, 3480–3484 (2007).

47.   Wehner, M. *et al.* An integrated design and fabrication strategy for entirely soft, autonomous robots. *Nature* **536**, 451–455 (2016).

48.   Markvicka, E. J., Bartlett, M. D., Huang, X. & Majidi, C. An autonomously electrically self-healing liquid metal-elastomer composite for robust soft-matter robotics and electronics. *Nat. Mater.* **17**, 618–624 (2018).

49.   Dickey, M. D. Stretchable and Soft Electronics using Liquid Metals. *Adv. Mater.* **1606425**, 1–19 (2017).

50.   Creton, C. 50th Anniversary Perspective: Networks and Gels: Soft but Dynamic and Tough. *Macromolecules* **50**, 8297–8316 (2017).

51.   Okumura, Y. & Ito, K. The polyrotaxane gel: A topological gel by figure-of-eight cross-links. *Adv. Mater.* **13**, 485–487 (2001).

52.   Noda, Y., Hayashi, Y. & Ito, K. From topological gels to slide-ring materials. *J. Appl. Polym. Sci.* **131**, 1–9 (2014).

53.   Cordier, P., Tournilhac, F., Soulié-Ziakovic, C. & Leibler, L. Self-healing and thermoreversible rubber from supramolecular assembly. *Nature* **451**, 977–80 (2008).

54.   Brown, H. R. A Model of the Fracture of Double Network Gels. *Macromolecules* **40**, 3815–3818 (2007).

55.   Ragelle, H. *et al.* Surface tension-assisted additive manufacturing. *Nat. Commun.* **9**, 1–10 (2018).

56.   Li, T., Chen, Y., Hu, X., Li, Y. & Wang, L. Exploiting negative Poisson's ratio to design 3D-printed composites with enhanced mechanical properties. *Mater. Des.*

142, 247–258 (2018).

57. Zhu, F. *et al.* 3D-Printed Ultratough Hydrogel Structures with Titin-like Domains. *ACS Appl. Mater. Interfaces* **9**, 11363–11367 (2017).

58. Feng, X. *et al.* A highly stretchable double-network composite. *Soft Matter* **12**, 8999–9006 (2016).

59. Webber, R. E., Creton, C., Brown, H. R. & Gong, J. P. Large Strain Hysteresis and Mullins Effect of Tough Double-Network Hydrogels. *Macromolecules* **40**, 2919–2927 (2007).

60. Yang, W. *et al.* On the tear resistance of skin. *Nat. Commun.* **6**, 6649 (2015).

61. Yang, J., Bai, R. & Suo, Z. Topological Adhesion of Wet Materials. *Adv. Mater.* **30**, 1–7 (2018).

62. Steck, J., Yang, J. & Suo, Z. Covalent Topological Adhesion. *ACS Macro Lett.* **8**, 754–758 (2019).

63. Yang, J. *et al.* Design Molecular Topology for Wet–Dry Adhesion. *ACS Appl. Mater. Interfaces* **11**, 24802–24811 (2019).

64. Hubbard, A. M. *et al.* Hydrogel/Elastomer Laminates Bonded via Fabric Interphases for Stimuli-Responsive Actuators. *Matter* 1–16 (2019). doi:10.1016/j.matt.2019.04.008

65. Shabahang, S. *et al.* Controlled fragmentation of multimaterial fibres and films via polymer cold-drawing. *Nature* **534**, 529–533 (2016).

66. Yang, C., Yin, T. & Suo, Z. Polyacrylamide hydrogels. I. Network imperfection.

J. Mech. Phys. Solids **131**, 43–55 (2019).

67.   Creton, C. & Ciccotti, M. Fracture and adhesion of soft materials: a review.

        Reports Prog. Phys. **79**, 046601 (2016).

68.   Long, R. & Hui, C.-Y. Fracture toughness of hydrogels: measurement and

        interpretation. *Soft Matter* **12**, 8069–8086 (2016).

69.   King, D. R., Okumura, T., Takahashi, R., Kurokawa, T. & Gong, J. P.

        Macroscale Double Networks: Design Criteria for Optimizing Strength and

        Toughness. *ACS Appl. Mater. Interfaces* **11**, 35343–35353 (2019).

70.   Cohen, Y., Ramon, O., Kopelman, I. J. & Mizrahi, S. Characterization of

        inhomogeneous polyacrylamide hydrogels. *J. Polym. Sci. Part B Polym. Phys.*

        30, 1055–1067 (1992).

71.   Yazici, I. & Okay, O. Spatial inhomogeneity in poly(acrylic acid) hydrogels.

        Polymer (Guildf). **46**, 2595–2602 (2005).

72.   Sakai, T. *et al.* Design and fabrication of a high-strength hydrogel with ideally

        homogeneous network structure from tetrahedron-like macromonomers.

        Macromolecules **41**, 5379–5384 (2008).

73.   Liu, C. *et al.* Unusual Fracture Behavior of Slide-Ring Gels with Movable Cross-

        Links. *ACS Macro Lett.* **6**, 1409–1413 (2017).

74.   Kim, J., Zhang, G., Shi, M. & Suo, Z. Fracture, fatigue, and friction of polymers

        in which entanglements greatly outnumber cross-links. *Science (80-.).* **216**, 212–

        216 (2021).

75.   Hou, S., Li, T., Jia, Z. & Wang, L. Mechanical properties of sandwich

composites with 3d-printed auxetic and non-auxetic lattice cores under low velocity impact. *Mater. Des.* **160**, 1305–1321 (2018).

76. Li, T., Liu, F. & Wang, L. Enhancing indentation and impact resistance in auxetic composite materials. *Compos. Part B Eng.* **198**, 108229 (2020).

77. Lei, M. *et al.* 3D Printing of Auxetic Metamaterials with Digitally Reprogrammable Shape. *ACS Appl. Mater. Interfaces* **11**, 22768–22776 (2019).

78. Munch, E. *et al.* Tough, bio-inspired hybrid materials. *Science (80-.).* **322**, 1516–1520 (2008).

79. Wang, L., Lau, J., Thomas, E. L. & Boyce, M. C. Co-continuous composite materials for stiffness, strength, and energy dissipation. *Adv. Mater.* **23**, 1524–1529 (2011).

80. Han, L., Wang, L., Song, J., Boyce, M. C. & Ortiz, C. Direct quantification of the mechanical anisotropy and fracture of an individual exoskeleton layer via uniaxial compression of micropillars. *Nano Lett.* **11**, 3868–3874 (2011).

81. Lee, J., Wang, L., Boyce, M. C. & Thomas, E. L. Periodic Bicontinuous Composites for High Specific Energy Absorption. *Nano Lett.* **12**, 4392–4396 (2012).

82. Hanifpour, M., Petersen, C. F., Alava, M. J. & Zapperi, S. Mechanics of disordered auxetic metamaterials. *Eur. Phys. J. B* **91**, 1–8 (2018).

83. Peng, X. L., Soyarslan, C. & Bargmann, S. Phase contrast mediated switch of auxetic mechanism in composites of infilled re-entrant honeycomb microstructures. *Extrem. Mech. Lett.* **35**, 100641 (2020).

84. Ting, T. C. T. & Chen, T. Poisson's ratio for anisotropic elastic materials can have no bounds. *Q. J. Mech. Appl. Math.* **58**, 73–82 (2005).

85. Norris, A. Extreme values of Poisson's ratio and other engineering moduli in anisotropic materials. *J. Mech. Mater. Struct.* **1**, 793–812 (2006).

86. Mousanezhad, D. *et al.* Hierarchical honeycomb auxetic metamaterials. *Sci. Rep.* **5**, 18306 (2016).

87. Tee, B. C. K., Wang, C., Allen, R. & Bao, Z. An electrically and mechanically self-healing composite with pressure- and flexion-sensitive properties for electronic skin applications. *Nat. Nanotechnol.* **7**, 825–832 (2012).

88. Hong, S. *et al.* 3D Printing of Highly Stretchable and Tough Hydrogels into Complex, Cellularized Structures. *Adv. Mater.* **27**, 4035–4040 (2015).

89. Zohuriaan-mehr, M. J. & Kabiri, K. Superabsorbent polymer materials: a review. *Iran. Polyemr J.* **17**, 451–477 (2008).

90. Li, P. *et al.* A polycationic antimicrobial and biocompatible hydrogel with microbe membrane suctioning ability. *Nat. Mater.* **10**, 149–156 (2011).

91. Hirota, N., Kakugo, A., Narita, T., Gong, J. P. & Osada, Y. Effect of aspect ratio on protein diffusion in hydrogels. *J. Phys. Chem. B* **104**, 9904–9908 (2000).

92. Jian Ping Gong *et al.* Synthesis of hydrogels with extremely low surface friction [4]. *J. Am. Chem. Soc.* **123**, 5582–5583 (2001).

93. Haraguchi, K. & Takeshisa, T. Nanocomposite Hydrogels : A Unique Organic-Inorganic Network Structure. *Adv. Mater.* 1120–1124 (2002).

94. Illeperuma, W. R. K., Sun, J. Y., Suo, Z. & Vlassak, J. J. Fiber-reinforced tough hydrogels. *Extrem. Mech. Lett.* **1**, 90–96 (2014).

95. Bin Imran, A. *et al.* Extremely stretchable thermosensitive hydrogels by introducing slide-ring polyrotaxane cross-linkers and ionic groups into the polymer network. *Nat. Commun.* **5**, 1–8 (2014).

96. Beebe, D. J. *et al.* Functional hydrogel structures for autonomous flow control inside microfluidic channels. *Nature* **404**, 588–590 (2000).

97. Tanaka, T. *et al.* 24. Easterling, K. E. & Tholen, A. R. Acta met. *Bruce, R. H. Sd Ceram* **8**, 203–205 (1975).

98. Zhang, X. *et al.* Optically- and thermally-responsive programmable materials based on carbon nanotube-hydrogel polymer composites. *Nano Lett.* **11**, 3239–3244 (2011).

99. Kim, M. Y., Jung, B. & Park, J. H. Hydrogel swelling as a trigger to release biodegradable polymer microneedles in skin. *Biomaterials* **33**, 668–678 (2012).

100. Hu, J. *et al.* Microgel-reinforced hydrogel films with high mechanical strength and their visible mesoscale fracture structure. *Macromolecules* **44**, 7775–7781 (2011).

101. Saito, J. *et al.* Robust bonding and one-step facile synthesis of tough hydrogels with desirable shape by virtue of the double network structure. *Polym. Chem.* **2**, 575–580 (2011).

102. Takahashi, R. *et al.* Tough Particle-Based Double Network Hydrogels for Functional Solid Surface Coatings. *Adv. Mater. Interfaces* **5**, 1–10 (2018).

List of Publications

7.1 Original papers related to doctoral dissertation

1. D. R. King, **T. Okumura**, R. Takahashi, T. Kurokawa & J. P. Gong: "Macroscale Double Networks: Design Criteria for Optimizing Strength and Toughness" *ACS Appl. Mater. Interfaces,* **11**(38), 35343-35353 (2019).

2. **T. Okumura**, R. Takahashi, K. Hagita, D. R. King & J. P. Gong: "Improving the Strength and Toughness of Macroscale Double Networks by Exploiting Poisson's Ratio Mismatch" *Scientific Reports,* **11**, 13280 (2021).

3. **T. Okumura**, T. Indei, D. R. King & J. P. Gong: "A Simple Macroscopic Model to Clarify the Defect-Insensitive Nature of Double-Networks" **in Preparation.**

4. **T. Okumura**, R. Takahashi, D. R. King & J. P. Gong: "Overcoming Volume Change Mismatch in Macroscale Reinforced Hydrogel Composites" **in Preparation.**

7.2 Presentation in conferences related to doctoral dissertation

1. **T. Okumura**, R. Takahashi, D. R. King & J. P. Gong: "Macroscale Toughening Mechanism Applying Double Network Effect", 10th CSE-ALP International Summer School, Hokkaido (Japan), July 2019.

2. **T. Okumura**, R. Takahashi, D. R. King & J. P. Gong: "ポアソン比ミスマッチによる高靭性ソフト・ハード複合材料の創製", 68th Symposium on Macromolecules, Fukui (Japan), September 2019.

3. **T. Okumura**, R. Takahashi, D. R. King & J. P. Gong: "Creation of Tough Soft/Hard Composites due to Poisson's ratio Mismatch Effect", International Hydrogel Workshop in Fukui 2019, Fukui (Japan), September 2019.

4. **T. Okumura**, R. Takahashi, D. R. King & J. P. Gong: "Design Parameters of Soft Composite Materials Containing Macroscale Double Networks", Strasbourg-Hokkaido Symposium, Strasbourg (France), November 2019.

5. **T. Okumura**, R. Takahashi, D. R. King & J. P. Gong: "機能性構造に誘起されたソフト材料の大変形による強靭化", 29th Annual Meeting of MRS-J, Kanagawa (Japan), November 2019.

6. **T. Okumura**, R. Takahashi, D. R. King & J. P. Gong: "Soft Composites Toughened by Applying the Effect of Poisson's Ratio Mismatch", 16th Pacific Polymer Conference, Singapore (Singapore), December 2019.

7. **T. Okumura**, R. Takahashi, D. R. King & J. P. Gong: "大変形可能な巨視的骨格構造を有するハイドロゲル複合材料の創製", 70th Symposium on Macromolecules, Online Virtual Meeting, December 2021.

8. **T. Okumura**, D. R. King & J. P. Gong: "大変形可能なハイドロゲル複合材料におけるオーセチック構造の効果", 56th SPSJ Hokkaido Branch Winter Meeting, Online Virtual Meeting, January 2022.

Acknowledgments

The research of this dissertation has been carried out in the Laboratory of Soft and Wet Matter (LSW), Graduate School of Life Science, Hokkaido University, Japan, which is supervised by Professor Jian Ping Gong. The associate examiners are Professor Takayuki Kurokawa, associate Professor Katsuhiko Sato, and assistant Professor Daniel R. King.

Firstly, I would like to show sincere appreciation and respect to my supervisor, Professor Jian Ping Gong, for all the support and encouragement during my bachelor's, master's and doctoral study in LSW. She gave me not only her tremendous academic support to become an outstanding researcher but also so countless wonderful opportunities. I really appreciate her for evaluating my interdisciplinary research. Moreover, I was taught that one of the most important things to become a leader is "tolerance" from her admirable life-style. I deeply respect her amicable personality, positive attitude, and understanding of research, hoping that I would be able to achieve some accomplishments as what she had done and live out a live like hers in the future.

Also, appreciation to follow researchers mentioned below can never be ignored: Professor Takayuki Kurokawa, associate Professor Tasuku Nakajima, associate Professor Takayuki Nonoyama, assistant Professor Daniel R. King and associate Professor Tsutomu Indei, for their helpfulness, scientific insight, fruitful discussions, and useful suggestions regarding to my research.

I am also very grateful to my post-doctoral fellows, guest researcher and research assistants in LSW and the Laboratory of Transformational Soft Matter (TSM). Especially, Dr. Yoshinori Katsuyama, and Ms. Yukiko Hane, who taught me not only about a lot of

scientific insight but also the responsibility and awareness as a member of the society. Then, I would like to thank the staffs in LSW and TSM, Ms. Eiko Hasegawa, Ms. Yuki Okubo, Ms. Saeko Iseya, and Yuri Kamada for helping and teaching me in financial work of Hokkaido University. I greatly appreciate all the past and present students of LSW and TSM, regardless of their nationality, for their kindness and friendly attitude.

Finally, grateful thanks to my family for almost unbelievable support during the life in Hokkaido University. They are the most important people in my world, and I dedicate this dissertation to them.

Tsuyoshi Okumura

Laboratory of Soft & Wet Matter

Division of Soft Matter

Graduate School of Life Science

Hokkaido University

Sapporo Japan

March 2022